

PHASE DIAGRAMS AND QUANTUM PHASE TRANSITIONS IN
LATTICE-CONFINED ANTIFERROMAGNETIC SPINOR BOSE-EINSTEIN
CONDENSATES

By

TAO TANG

Bachelor of Science in Physics
HeFei University of Technology
Hefei, China
2009

Master of Science in Physics
University of Science and Technology of China
Hefei, China
2012

Submitted to the Faculty of the
Graduate College of the
Oklahoma State University
in partial fulfillment of
the requirements for
the Degree of
DOCTOR OF PHILOSOPHY
December, 2018

PHASE DIAGRAMS AND QUANTUM PHASE TRANSITIONS IN
LATTICE-CONFINED ANTIFERROMAGNETIC SPINOR BOSE-EINSTEIN
CONDENSATES

Dissertation Committees:

Dr. Yingmei Liu
Dissertation Adviser

Dr. John Mintmire

Dr. Albert T. Rosenberger

Dr. Guoliang Fan

ACKNOWLEDGEMENTS

First, I would like to express my sincere gratitude to my thesis advisor Dr. Yingmei Liu, who took me into ultracold atoms field and gave me much guidance throughout my PhD study. Her widespread knowledge, insightful comments and persistent enthusiasm in physical research touched me deeply. As her graduate student, it has been a valuable experience to perform my PhD study under her advising. I also would like to thank my committee members, Dr. Albert Rosenberger, Dr. John Mintmire, and Dr. Guoliang Fan for their advice and support during my PhD study. I thank Dr. Rosenberger for the knowledge in optics, including physical optics, lasers, laser spectroscopy and non-linear optics I learnt from him. I thank Dr. Mintmire for his support in the department. I appreciate Dr. Fan often offered me some suggestions on research. During my more than five years study at OSU, I was lucky to work with many talented people, e.g. Lichao Zhao, Zihe Chen, Jared Austin and Zachary Shaw in our lab. They, as my current team members, have been providing me much help throughout all the aspects, especially in the last year. I also extend my thanks to our former labmates Jie Jiang and Micah Webb. Moreover, I would like to thank our staffs in the department of physics. Susan is a very nice woman and always helps us to deal with different problems when we need help. Alisha, Beth, Melissa and Charles, as well as Temra, Sandra and Warren, helped us a lot on ordering all kinds of lab equipments. Last but not least, I am greatly indebted to my father Erwen Tang, my mother Huamin Shen and my sister Qiong Shen for their endless love and spiritual support. Finally I especially thank my beloved girl-friend, who had accompanied with me all the time and brought me a lot of happiness. I dedicate this dissertation to them.

Name: TAO TANG

Date of Degree: DECEMBER, 2018

Title of Study: PHASE DIAGRAMS AND QUANTUM PHASE TRANSITIONS
IN LATTICE-CONFINED ANTIFERROMAGNETIC SPINOR BOSE-EINSTEIN
CONDENSATES

Major Field: PHOTONICS

Abstract: A spinor Bose-Einstein condensate (BEC) confined in optical lattices has attracted much attention for its abilities to systematically study, verify, and optimize condensed matter models. In this dissertation, I present results from three of our recent experimental studies on lattice-confined antiferromagnetic spinor BECs.

First, I explain how we have achieved the first experimental realization of the first-order superfluid (SF) to Mott-Insulator (MI) quantum phase transition in lattice-confined antiferromagnetic spinor BECs. Marking an important milestone, a second-order SF-MI transition was realized in scalar BECs about a decade ago. Spinor BECs, on the other hand, possess an additional spin degree of freedom, leading to a range of phenomena absent in scalar BECs. One important prediction is the existence of first-order SF-MI transitions in antiferromagnetic spinor BECs. By adiabatically loading sodium spinor BECs into sufficiently deep cubic lattices, we have observed trustworthy signatures of the first-order SF-MI transitions. These observed signatures include hysteresis effect, significant heatings across the phase transitions, and changes in spin populations due to the formation of spin singlets in the MI phase. We have found the nature of the phase transitions strongly depends on the ratio of the quadratic Zeeman energy q to the spin-dependent interaction. Our observations are qualitatively understood by the mean field theory (MFT), and also suggest tuning q is a new approach to realize SF-MI transitions.

Second, we have experimentally mapped the phase diagram of lattice-confined antiferromagnetic spinor BECs at various q and various magnetization. We have also studied the first-order SF-MI transition in different lattice geometries including monoclinic lattices. Good agreements between our experimental results and MFT are observed.

Third, we have theoretically proved and experimentally confirmed that combining cubic lattices with spinor BECs substantially relaxes three strict constraints and brings spin singlets of ultracold spin-1 atoms into experimentally accessible regions. A spin singlet of spin-1 atoms has been widely suggested as an ideal candidate in studying quantum information science, because of its long lifetimes and enhanced tolerance to environmental noises. Via two independent detection methods, we have demonstrated that around 80% of atoms in lattice-confined spin-1 spinor BECs can form spin singlets.

TABLE OF CONTENTS

Chapter	Page
I. INTRODUCTION	1
1.1 Theoretical predictions and experimental realizations of Bose-Einstein Condensates	1
1.2 Spinor BECs.....	2
1.3 Optical lattices	5
1.4 Bloch band structure	7
1.5 Bose-Hubbard model	11
1.6 Outline.....	16
II. EXPERIMENTAL SETUP	18
2.1 Experimental setup for generating sodium BECs	18
2.2 Setup for creating microwave dressing fields	21
2.3 Experimental setup of three-dimensional optical lattices	22
III. FIRST-ORDER SUPERFLUID TO MOTT-INSULATOR PHASE TRANSITIONS IN CUBIC OPTICAL LATTICES	28
3.1 Superfluid to Mott-insulator phase transition	28
3.2 Signatures of the first-order Superfluid to Mott-insulator phase transitions	33
3.3 Phase diagrams of spinor Mott-Insulators	45
IV. FIRST-ORDER SUPERFLUID TO MOTT-INSULATOR PHASE TRANSITIONS IN THREE-DIMENSIONAL MONOCLINIC LATTICES	52
4.1 Theoretical model	53
4.2 Superfluid to Mott-insulator phase transition in monoclinic lattices	55
4.3 Differences induced by the purification of initial states	58
V. LATTICE-INDUCED RAPID FORMATION OF SPIN SINGLET IN SPIN-1 SPINOR CONDENSATES	63

Chapter	Page
5.1 Create spin singlet states in free space or with optical lattices	63
5.2 Experimental signatures of spin-singlet states	69
5.3 Light-scattering measurements	73
VI. FUTURE DIRECTIONS	81
6.1 First-order superfluid to Mott-Insulator phase transition in a homogeneous system	81
6.2 Non-equilibrium dynamics of spinor BECs in optical lattices	82
6.3 Applications in quantum information science	84
REFERENCES	85
APPENDICES	95
APPENDIX A: DYNAMICS IN SPINOR CONDENSATES TUNED BY A MICROWAVE DRESSING FIELD.....	95
APPENDIX B: FIRST-ORDER SUPERFLUID-TO-MOTT-INSULATOR PHASE TRANSITIONS IN SPINOR CONDENSATES	101
APPENDIX C: LATTICE-INDUCED RAPID FORMATION OF SPIN SINGLETS IN SPIN-1 SPINOR CONDENSATES	107

LIST OF TABLES

Table	Page
1.1 A short list of the reported scattering lengths a_0 and a_2 in the unit of the Bohr radius a_B , and the ratio U_2/U_0 in the ^{23}Na system	13
2.1 Useful parameters of our three-dimensional optical lattices.....	23

LIST OF FIGURES

Figure		Page
1.1	Bosonic atoms undergo a BEC phase transition when their temperature is lowered down.	2
1.2	Band structures of ultracold atoms in a 1D optical lattice at (a) $u_L = 0E_R$, (b) $u_L = 6E_R$, (c) $u_L = 12E_R$, and (d) $u_L = 18E_R$ (30, 31).	9
1.3	The plane-wave decompositions $ c_{j,nq} ^2$ of the Bloch eigenstates for the three lowest bands (a) Band 0 (b) Band 1 (c) Band 2 at $u_L = 18E_R$	9
1.4	The plane-wave decompositions $ c_{j,nq} ^2$ of the Bloch eigenstates for the three lowest bands (a) Band 0 (b) Band 1 (c) Band 2 at $u_L = 6E_R$	10
1.5	The tunneling energy J (left) and the on-site interaction U (right) in an optical lattice.	12
2.1	Optical setup for generating multiple laser beams used in cooling and trapping sodium atoms.	19
2.2	The atomic structure (the D_2 line) of a ^{23}Na atom and frequencies of various laser beams used in laser cooling and trapping sodium atoms (46).	20
2.3	The sketch of our dipole trap and an illustration of the evaporative cooling process. The white and black atoms represent atoms with high and low energy, respectively. The energy of the shaded atoms fall in between those of the white and black atoms.	25
2.4	(a) The $F = 1$ and $F = 2$ hyperfine structures of the $3^2S_{1/2}$ level in ^{23}Na atoms when an external magnetic field is applied. The three chosen transitions are marked by straight lines with arrows. (b) The number of atoms in the $F = 2$ state excited by a resonant microwave pulse as a function of the pulse duration. The solid lines are sinusoidal fits to extract the on-resonance Rabi frequency Ω of the pulse. Blue and Red colors represent Rabi frequencies measured by using the old antenna and new antenna, respectively.	26
2.5	Optical setup for three-dimensional lattices.	27
2.6	The periodic lattice potential in the dipole trap.	27

Figure	Page
3.1 (a) MF phase diagrams derived from the BH model for scalar BECs in cubic lattices (33). Inset: two typical TOF pictures shows the SF and MI states. (b) The superfluid order parameter ϕ_{SF} versus u_L at $\mu/U_0 = 1.4$ in scalar BECs.	30
3.2 (a) MF phase diagrams derived from the BH model for the LP and TP sodium spinor BECs in cubic lattices. (b) The superfluid order parameter ϕ_{SF} versus u_L at $\mu/U_0 = 1.4$ in LP spinor BECs at $q_B/h = 20$ Hz. Here $ \phi_{\text{SF}} ^2 = N_{\text{SF}}$ and h is the Planck constant.	31
3.3 Predicted SF-MI transition point u_c versus q_B at $\mu/U_0 = 1.4$ for scalar BECs and LP spinor BECs after lattices are ramped up and down.	32
3.4 (a) Schematic of the reciprocal lattice and a TOF image taken after lattices are abruptly released. The area in red represents the imaging beam. (b) Two lattice ramp sequences used in this chapter. (c) A TOF image showing the first Brillouin zone.	34
3.5 Interference patterns observed after we abruptly release scalar (top), LP spinor (middle), and TP spinor BECs (bottom) at various u_L and a 5.5-ms TOF at $q_B/h = 360$ Hz. Panels (a)-(c) are taken after ramp-up sequences to a final $u_L = 2, 10, \text{ and } 26E_R$, respectively. Panels (d)-(e) are taken after ramp-down sequences to a final u_L of $12E_R$ and $4E_R$. The field of view is $400 \mu\text{m} \times 400 \mu\text{m}$	35
3.6 Peak OD of interference peaks versus u_L after lattice ramp-up sequences. Markers are experimental data and lines are linear fits. We estimate u_c from the intersection of two linear fits to the data. The inset shows how we extract the peak OD from a TOF image (left). The dotted line in the right inset is a density profile of this TOF image through the central and one pair of interference peaks along the vertical direction, while the solid line is a bimodal fit to one side peak.	36
3.7 Peak OD of interference peaks versus u_L after lattice ramp-down sequences. Markers are experimental data and lines are linear fits. We estimate u_c from the intersection of two linear fits to the data.	37

Figure	Page
3.8 (a) Theoretical calculation of the energy gaps across the SF-MI phase transitions. Significant heating, resulted from these energy gaps when atoms cross the phase transitions, is regarded as a signature of the first-order SF-MI phase transitions. (b) The value of the energy gap between MSF and MI state (ramp up sequence) versus q_B .	39
3.9 Peak OD of interference peaks versus q_B observed after lattice ramp down sequences to $10E_R$. Markers are experimental data. Red and blue lines are exponential fits. The black line is a linear fit.	40
3.10 (a) Measured ρ_0 versus u_L after an initial LP spinor BEC undergoes ramp-up sequences to various final u_L at $q_B/h = 20$ Hz. The solid line is a sigmoidal fit. (b) Similar to (a) except that we set q_B at various values, and the final u_L at $26E_R$ to ensure atoms enter into the MI phase. The dashed (solid) line represents the MF result for $n = 2$ ($n_{\text{peak}} = 5$).	41
3.11 (a) N_{SF} and (b) the fractional population ρ_0 of the ground state at various chemical potential μ and lattice depth u_L with $q_B/h = 20$ Hz. Metastable states are not shown in these figures.	43
3.12 (a) N_{SF} and (b) the fractional population ρ_0 of the ground state at various quadratic Zeeman energy q_B and lattice depth u_L with $\mu/U_0 = 1.4$. Metastable states are not shown in these figures.	44
3.13 ρ_0 of the ground state as a function of q_B/U_2 for five different n (occupation number per site) in the MI phase.	45
3.14 (a) Experimental ρ_0 in the ground state at various q_B/U_2 and magnetizations m in cubic lattices. (b) The predicted ρ_0 for $n = 2$ in the ground state at various q_B/U_2 and m . (c) The predicted ρ_0 for $n_{\text{peak}} = 5$ in the ground state at various q_B/U_2 and m .	51
4.1 (a) Schematic of reciprocal lattice and TOF images from top and side views taken after lattices are abruptly released. The imaging beams are shown by the red area. (b) Schematic of our monoclinic lattices setup. We set $\theta = \pi/4$.	55

4.2	Peak optical density of interference peaks versus u_L after our cubic and monoclinic lattices ramp-up sequences. Experimental data are shown by different markers, and lines are two linear fits to the data. Here cubic lattices data are copied from our paper (44). Inset: It shows how we extract the peak optical density from a TOF image. The blue solid line is a gaussian fit to the side peak. Here the magnetic field is set at $q_B/h = 360$ Hz.	56
4.3	Peak optical density of interference peaks taken in our monoclinic and cubic lattice experiments versus J_5/U_0 . Solid lines are exponential fits to the experimental data. Here the magnetic field is set at $q_B/h = 360$ Hz.	57
4.4	(a) We measured ρ_0 at various q_B in monoclinic lattices. In order to ensure all atoms enter into the MI phase, we set the final u_L at $26E_R$. (b) Similar to Panel (a) but we set $q_B/h = 20$ Hz. Solid lines in Panels (a) and (b) are exponential and sigmoidal fits, respectively.	57
4.5	(a) Measured ρ_0 versus q_B/h (b) Measured ρ_0 versus q_B/U_2 and the final u_L at $26E_R$ and $45E_R$ in monoclinic lattices, and at $26E_R$ in cubic lattices. Solid lines are the MF results at various occupation number n . Here the maximum of n is five.	59
4.6	Interference patterns observed after we abruptly release TP and LP spinor BECs at $q_B/h = 360$ Hz (a high magnetic field) and $q_B/h = 20$ Hz (a low magnetic field) at various u_L and a 4.5-ms Stern-Gerlach separation during a 5.5-ms TOF. Panels (a)-(b) are taken after ramp-up sequences to a final $u_L = 2E_R$ and $12E_R$. Panels (c)-(d) are taken after first ramping up the lattice to $26E_R$ and then ramping the lattice down to a final u_L of $12E_R$ and $2E_R$. The lattice ramp speed is $2E_R$ per one millisecond.	60
4.7	Absorption images taken after linearly ramping up the lattice to a final u_L ($2E_R$ or $8E_R$), holding TP states at the final u_L for various time, abruptly releasing atoms from the lattices, and a 5.5-ms TOF (including a 4.5-ms Stern-Gerlach separation) at $q_B/h = 360$ Hz and 20 Hz.	61

5.1 (a) and (b): vertical black (red) dotted lines mark q_{\max} , the maximum allowed q for spin singlets, in $F=1$ sodium spinor BECs of $n = 10^5$ atoms in free space (in the $n=2$ Mott lobe at $u_L = 26E_R$). All panels are derived from MFT at zero m with solid (dashed) lines representing the $q < 0$ ($q > 0$) region, and black (red) lines representing spinor gases in free space (spinor Mott insulators). (a) Predicted ρ_0 versus $ q $ at $n = 2$ (red) and 10^5 (black). The top horizontal axis lists the corresponding B when $q > 0$. (b) Predicted $\Delta\rho_0$ versus $ q $ at $n = 2$ (red) and 10^5 (black).....	64
5.2 (a) Predicted q_{\max} versus n . (b) The minimum time t_{\min} versus n for generating singlets of sodium atoms via an adiabatic sweep at its corresponding $\pm q_{\max}$	65
5.3 The maximum allowed m for spin singlets at $q = 0$, derived from the mean-field theory for $F=1$ sodium spinor BECs.	67
5.4 Measured ρ_0 versus t_{ramp} after an initial LP spinor BEC enters the MI phase in a high field. Black lines are two linear fits. We estimate t_0 , the ideal t_{ramp} , from the intersection point of these two lines (see text).....	68
5.5 (a) Measured ρ_0 (red circles) and (b) $\Delta\rho_0$ (blue triangles) versus u_L after an initial TP spinor BEC undergoes the ideal lattice sequence to various final u_L in a weak field near zero q . The solid line is a sigmoidal fit, and the dashed line is to guide the eye.	70
5.6 (a) Red circles (blue triangles) are the measured ρ_0 in spinor Mott insulators without (with) atoms being rotated by resonant $\pi/2$ pulses at various q . The red dashed line is the prediction of Eq. (5.4). The insulators are created after an initial TP spinor BEC undergoes the ideal lattice ramp sequence.	73
5.7 The optical setup of light-scattering measurements. Here PDs are photodetectors and PBS is a polarized beam-splitter.....	75
5.8 The relation between the off-diagonal element N_{yz} of the nematicity matrix and the angle θ (see text).	76
5.9 Predicted spatial distributions of I_{yz} when the light-scattering beam is linearly polarized. Here I_{yz} is proportional to $ \int \psi(y, z) * N_{yz} \psi(y, z) dx ^2$, and can be experimentally recorded by replacing one photodetector (i.e., PD2) in Fig. 5.7 with an ultra-sensitive CCD camera.	77

Figure	Page
5.10 The value of $ E/E^{(0)} ^2$ versus the frequency detuning. The red and blue lines correspond to the LP state and scalar state, respectively. The simulation is derived at $\theta = 45^\circ$	78
5.11 The value of $ E/E^{(0)} ^2$ versus the frequency detuning at $\theta = 45^\circ$. The lines are the theoretical predictions and the markers are our experimental data. The red (blue) color corresponds to the LP (scalar) state.	79
5.12 The Fourier transformation results for the vacuum state and a spinor BEC ($\rho_0 = 0.5$, $m = 0$).....	80
6.1 Simulation results for an initial LP state crossing the superfluid to the Mott-Insulator phase transitions at $u_L = 32E_R$ in $q/h = 75\text{Hz}$	82
6.2 The dip time as a function of the quadratic Zeeman energy q	83
6.3 Amplitude of spin oscillations as a function of the quadratic Zeeman energy q	83

CHAPTER I

INTRODUCTION

1.1 Theoretical predictions and experimental realizations of Bose-Einstein condensates

A Bose-Einstein condensation is a phase transition that happens at a very low temperature. This kind of phase transition was proposed by Satyendra Nath Bose and Albert Einstein in 1925 (1). An illustration of a typical BEC transition is shown in Fig. 1.1. First, when the temperature T of an atomic system is high, the inter-particle distance d is large and the system can be characterized by d . The value of d decreases with the temperature. When the atomic gases are cooled down to a very low temperature (close to a critical temperature T_c), d becomes comparable to the deBroglie wavelength λ_{db} . At $T \leq T_c$, the system undergoes a phase transition from a thermal cloud to a BEC with a large number of atoms occupying the lowest energy state (2). At zero temperature, atoms can form a pure BEC with all particles being in the ground states. One of important advantages of a BEC system is that it provides an opportunity to observe quantum effects on a macroscopic scale.

Due to numerous technical difficulties associated with cooling down atoms to an ultracold temperature, it took the physics community 70 years to experimentally realize it (3). In 1995, Eric Cornell and Carl Wieman at the University of Colorado and Wolfgang Ketterle at MIT successfully produced BECs with neutral alkali metal atoms (2, 4, 5). Marking a significant milestone in providing a revolutionary method to observe microscopic quantum

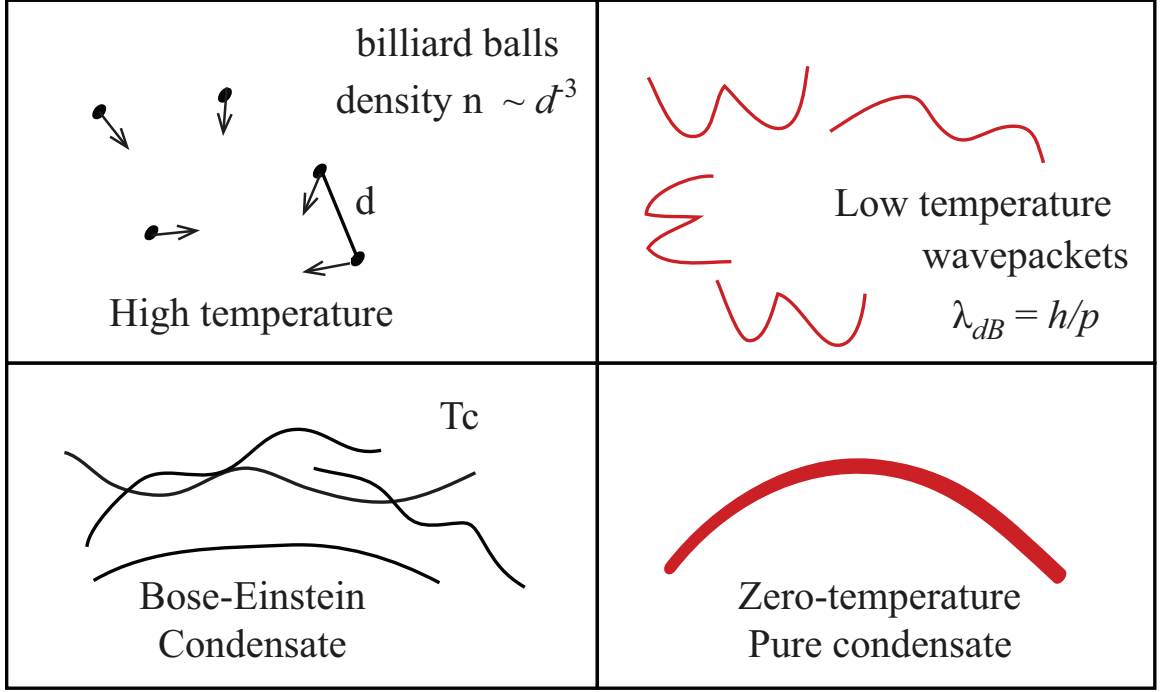


Figure 1.1: Bosonic atoms undergo a BEC phase transition when their temperature is lowered down.

phenomena in a macroscopic scale, this achievement was awarded a Nobel prize in physics in 2001.

In the following two decades, various kinds of BECs are realized experimentally with different types of atomic species, e.g. ^{87}Rb at the University of Colorado (2), ^{23}Na at MIT (4), ^7Li at Rice University (5), ^1H (6), ^{85}Rb (7), ^{39}K (8), ^{133}Cs (9), ^{174}Yb (10), and ^{52}Cr (11). Nowadays, BECs have been applied to many other fields, such as condensed matter physics, astrophysics, quantum communication and precision measurements.

1.2 Spinor BECs

There are two popular methods to generate BECs. The first method is to create BECs through an evaporative cooling inside a magnetic trap (2, 4, 5), in which the spin degree of freedom is frozen and only one spin component can be trapped. This type of BEC is named as scalar BECs. The other method is to create BECs through an evaporative cooling inside

an optical trap (12). Because all spin components can be confined in an optical trap, atoms in this type of BECs gain an additional spin degree of freedom. This type of BECs is thus named as spinor BECs. My Ph.D. research focuses on a $F = 1$ spinor BEC system that contains three different spin components (i.e., atoms in the $|1, -1\rangle$, $|1, 0\rangle$ and $|1, +1\rangle$ atomic states).

In $F = 1$ spinor condensates, the only interesting coherent collision is the spin-changing collision between two spin-zero atoms and a pair of a spin-up atom and a spin-down atom, i.e., $|1, 0\rangle + |1, 0\rangle \rightleftharpoons |1, +1\rangle + |1, -1\rangle$. In the spin-changing collision, the total atom number N and the total magnetization m are found to be conserved. When an external magnetic field is applied, the effective Hamiltonian of a spinor BEC system can be written as (13)

$$H = T + V_{\text{ext}}(r) + H_z + H_s , \quad (1.1)$$

where T is the kinetic energy and $V_{\text{ext}}(r)$ is an external potential (e.g., the potential induced by an optical trap). The last term, H_s , represents spin-dependent and spin-independent interactions. The Zeeman effect term, H_z , represents the interaction between the effective magnetic moment of an atom and an external magnetic field B . For alkali atoms with $I = 3/2$ at weak magnetic fields, H_z can be approximated as (13)

$$H_z(F = 1) = \int (pF_z + qF_z^2) dr , \quad (1.2)$$

where $p = (E_{+1} - E_{-1})/2$ stands for the linear Zeeman effect and $q = (E_{+1} + E_{-1} - 2E_0)/2$ characterizes the quadratic Zeeman effect. For $F = 1$ bosons, the total spin f can only be the even values: $f = 0$ and $f = 2$. The total spin $f = 1$ is forbidden due to the bosonic parity (14). Therefore we can write H_s as (13)

$$H_s(F = 1) = \int (c_0 : n^2 : + c_2 : F^2 :) dr / 2 , \quad (1.3)$$

where $::$ denotes normal ordering that requires creation operators are placed to the left of annihilation operators. The coupling coefficients c_0 and c_2 are linear combinations of the

s-wave scattering lengths a_f . For $F = 1$, a_f is a_0 or a_2 . If c_2 is positive (negative), F^2 should be minimized (maximized) to derive the ground state. Based on the sign of c_2 , spinor BECs are divided into two categories: anti-ferromagnetic spinor BECs with $c_2 > 0$ (e.g., the ^{23}Na BEC system) and ferromagnetic spinor BECs with $c_2 < 0$ (e.g., the ^{87}Rb BEC system) (15).

For a small BEC whose size is smaller than the spin healing length, the single spatial mode approximation (SMA) can be applied (16). In SMA, the spatial and spin wavefunctions are separated, and the wavefunction of spinor condensates can be written as (13, 17)

$$\psi(r, t) = \sqrt{N} \phi(r) \phi_{m_F} \exp(-iE_{m_F}t/\hbar) , \quad (1.4)$$

where \hbar is the reduced Planck constant, $\phi(r)$ is the spatial wave function, $\int |\phi(r)|^2 dr = 1$, and N is the total number of atoms. In addition, ϕ_{m_F} represents the spin wave function, where $m_F = +1, 0, -1$, and $\sum_{m_F=-1}^{+1} |\phi_{m_F}|^2 = 1$. We define the fractional population of each m_F state as $\rho_{m_F} = |\phi_{m_F}|^2$, where $\phi_{m_F} = \sqrt{\rho_{m_F}} \exp(-i\theta_{m_F})$ with θ_{m_F} being the phase of each m_F state. So $\rho_{-1} + \rho_0 + \rho_{+1} = 1$.

After taking into account the total atom number N and total magnetization m (m is defined as $m = \rho_{+1} - \rho_{-1}$.) are independent of time t , we can express the BEC energy E , and the time evolution of ρ_0 and θ ($\theta = \theta_{+1} + \theta_{-1} - 2\theta_0$) as follows, (15, 17)

$$E(t) = c\rho_0(t)\{[1 - \rho_0(t)] + \sqrt{[1 - \rho_0(t)]^2 - m^2} \cos[\theta(t)]\} + q(t)[1 - \rho_0(t)] , \quad (1.5)$$

$$\dot{\rho}_0 = \frac{-4\pi}{h} \frac{\partial E(t)}{\partial \theta(t)} = \frac{2c}{h} \sqrt{(1 - \rho_0^2) - m^2} \sin \theta , \quad (1.6)$$

$$\dot{\theta}_0 = \frac{4\pi}{h} \frac{\partial E(t)}{\partial \rho_0(t)} = -\frac{2q}{h} + \frac{2c}{h} (1 - 2\rho_0) + \frac{2c(1 - \rho_0)(1 - 2\rho_0) - m^2}{h \sqrt{(1 - \rho_0^2) - m^2}} \cos \theta . \quad (1.7)$$

Here h is the Planck constant. We can derive the ground states by minimizing Eq. (1.5). When $m = 0$ and $q > 0$, the ground state is found to be the longitudinal polar (LP) state with $\rho_0 = 1$.

Here the quadratic Zeeman energy q is generated by a magnetic field and is always a positive

value. To obtain an negative quadratic Zeeman energy q , we can apply a microwave dressing field (15, 18, 19, 20, 21) or a linearly polarized off-resonant laser beam (22). They can both shift the quadratic Zeeman energy to the negative region. Here I will only discuss microwave dressing fields.

According to the second order perturbation theory and summing over the contribution from all possible transitions, the energy shift of $|F = 1, m_F\rangle$ can be derived as (16),

$$\begin{aligned}\delta E|_{m_F} &= \frac{h}{4} \sum_{k=0,\pm 1} \frac{\Omega_{m_F, m_F+k}^2}{\Delta_{m_F, m_F+k}} \\ &= \frac{h}{4} \sum_{k=0,\pm 1} \frac{\Omega_{m_F, m_F+k}^2}{\Delta - [(m_F + k)/2 - (-m_F/2)]\mu_B B} .\end{aligned}\quad (1.8)$$

Here Ω_{m_F, m_F+k} is the on-resonance Rabi frequency that is proportional to the Clebsch-Gordan coefficient C_{m_F, m_F+k} , Δ is the detuning from the $|F = 1, m_F = 0\rangle \leftrightarrow |F = 2, m_F = 0\rangle$ transition and μ_B is the Bohr magneton.

Thus the net quadratic Zeeman energy q is the sum of q_B generated from the magnetic fields and q_M induced by a microwave dressing field, and can be expressed as (16)

$$\begin{aligned}q &= q_B + q_M \\ &= aB^2h + \frac{\delta E|_{m_F=+1} + \delta E|_{m_F=-1} - 2\delta E|_{m_F=0}}{2} ,\end{aligned}\quad (1.9)$$

where $a \approx 277 \text{ Hz/G}^2$ for $F=1$ ^{23}Na atoms and $a \approx 71.9 \text{ Hz/G}^2$ for $F=1$ ^{87}Rb atoms.

1.3 Optical lattices

An optical lattice is formed when a pair of laser beams interfere, which creates a periodic potential. Optical lattices are versatile tools that can conveniently control interatomic interactions and the mobility of atoms by varying such parameters as the power and polarization of optical lattice beams. Cold atoms trapped in optical lattices resemble a lattice structure in a solid state material, thus have been applied to various research areas, such

as simulating condensed matter systems and studying quantum information science. The lattice depth and the lattice spacing are two important parameters of optical lattices. The lattice depth can be tuned by changing the intensity of the laser beams, while the lattice spacing can be modified by changing the wavelength of the laser beams or by changing the relative angle of optical lattice beams.

Neutral atoms can be trapped by this periodic potential due to the AC Stark effect. The potential created by a single optical beam of the optical intensity $I(\mathbf{r})$ can be written as (23),

$$V(\mathbf{r}) = \frac{3\pi\hbar\Gamma c^3}{2\Delta\omega_R^2} I(\mathbf{r}) , \quad (1.10)$$

where Γ is the nature linewidth, c is the speed of light, ω_R is the resonance frequency of the transition, and Δ is the frequency detuned from the resonance frequency. An optical lattice can be formed by retro-reflecting the lattice beam. This is the easiest way and is adopted in our experiments. We can describe lattice beams as Gaussian beams with the wavelength λ_L as follows,

$$V_{lat}(r, z) = 4V_s \left[1 - 2 \left(\frac{r}{\omega_0} \right)^2 - \left(\frac{z}{z_R} \right)^2 \right] \cos^2 \left(\frac{2\pi z}{\lambda_L} \right) , \quad (1.11)$$

Here V_s is the peak potential of a single beam,

$$V_s = \frac{3\pi\hbar\Gamma c^3}{2\Delta\omega_R^2} \frac{2P}{\pi\omega_0^2} , \quad (1.12)$$

and the optical intensity $I(r, z)$ is described as,

$$I(r, z) = \frac{2P}{\pi\omega_0^2} \left[1 - 2 \left(\frac{r}{\omega_0} \right)^2 - \left(\frac{z}{z_R} \right)^2 \right] . \quad (1.13)$$

Here, P is the power of the laser, ω_0 is the Gaussian beam waist at its focus point, and $z_R = \pi\omega_0^2/\lambda_L$ is the Rayleigh length. Equation 1.11 stands for a periodic potential with a period (lattice spacing) of $\lambda_L/2$.

We can treat the lattice potential as the fast oscillating potential in the unit of E_R , and

express the three-dimensional lattice potential as,

$$V_{lat}(\mathbf{x}) = E_R \widetilde{u_L} (\sin^2(k_L x) + \sin^2(k_L y) + \sin^2(k_L z)) , \quad (1.14)$$

where $E_R = \hbar^2 k_L^2 / (2M)$ is the recoil energy, $\widetilde{u_L} = 4V_s / E_R$ is the dimensionless lattice depth, and $k_L = 2\pi / \lambda_L$. Note that the above derivations of Eqs. (1.10–1.14) are based on Ref. (23).

When the interaction energy ϵ_{int} is much smaller than the kinetic energy ϵ_{kin} . The ratio of these two energy terms is (24)

$$\frac{\epsilon_{int}}{\epsilon_{kin}} \approx 4\pi n_0^{1/3} a_s , \quad (1.15)$$

where n_0 is the particle density and a_s is the scattering length. In BECs, in general, the interparticle distance $d \sim n^{-1/3}$ is larger than the scattering length a_s . Therefore, the ratio $\frac{\epsilon_{int}}{\epsilon_{kin}}$ in Eq. (1.15) is very small (i.e., $\frac{\epsilon_{int}}{\epsilon_{kin}} \sim 0.02$). To enter into the strong coupling regime, we can increase the scattering length and/or the particle density. The scattering length can be altered by Feshbach resonances (25, 26), although its experimental realization is difficult. In contrast, optical lattices offer a convenient method: raising the power of optical lattice beams can prevent atoms from hopping among lattice sites and significantly increase the interatomic interactions (26, 27, 28).

1.4 Bloch band structure

To simplify our discussions, we first ignore the interactions between atoms and focus on the situation with only one single atom in the periodic lattice potentials. I start with discussing the wave-function calculations in a one-dimensional lattice potential, which is constructed by one pair of counter-propagating laser beams along the x -direction.

Since the potential V_{lat} in optical lattices is periodical, according to the Bloch theorem, the

solution of the wave function can be written as (29),

$$\Psi_{n\mathbf{q}}(\mathbf{x}) = e^{i\mathbf{q}\cdot\mathbf{x}} u_{n\mathbf{q}}(\mathbf{x}) . \quad (1.16)$$

Here \mathbf{q} is the quasimomentum, n is the band index, and $u_{n\mathbf{q}}(\mathbf{x})$ has the same periodicity as the optical lattices. Then Schrödinger equation can be written as

$$H\Psi_{n\mathbf{q}}(\mathbf{x}) = E_{n\mathbf{q}}\Psi_{n\mathbf{q}}(\mathbf{x}), \quad H = \frac{1}{2m}\hat{p}^2 + V_{\text{lat}}. \quad (1.17)$$

After substituting Eq. 1.16 into Eq. 1.17, we expand u and V with their Fourier series as

$$\begin{cases} u_{nq}(x) = \frac{1}{\sqrt{2\pi}} \sum_{j=-\infty}^{\infty} c_{j,nq} e^{-ijk_L x} , \\ V(x) = \sum_r V_r e^{-ijk_L r} . \end{cases}$$

As $V_{\text{lat}} = \frac{1}{4}\widetilde{u}_L E_R (e^{-2ik_L x} + e^{-2ik_L x} + 2)$, Eq. 1.17 can be expressed in the matrix form as follows,

$$H_{j,j'} = \begin{cases} [(2j + q/k_L)^2 + \widetilde{u}_L/2]E_R , & \text{if } j = j' ; \\ -\widetilde{u}_L E_R / 4 , & \text{if } |j - j'| = 1 ; \\ 0 , & \text{if } |j - j'| > 1 . \end{cases} \quad (1.18)$$

Note that the derivations of Eqs. (1.16–1.18) are based on Ref. (29). For a given quasimomentum q , the energy bands are characterized by the eigenvalues E . These eigenvalues and corresponding eigenstates can be calculated numerically. Generally the Hamiltonian is truncated at a given value. In our calculations, this value is set at 20, which means Bloch states are expanded into 20 discrete plane-wave basis. Figure 1.2 shows the band structure calculated at different lattice depths, i.e., eigenenergies versus quasimomentum for the first three or four bands ($n = 0$ to $n = 3(4)$) from $q = -\hbar k$ to $q = +\hbar k$ within the first Brillouin zone. The observed first Brillouin zone will be shown in Chapter III. When the lattice depth is 0, it means there is no lattice effect and the energy-momentum relationship of atoms is

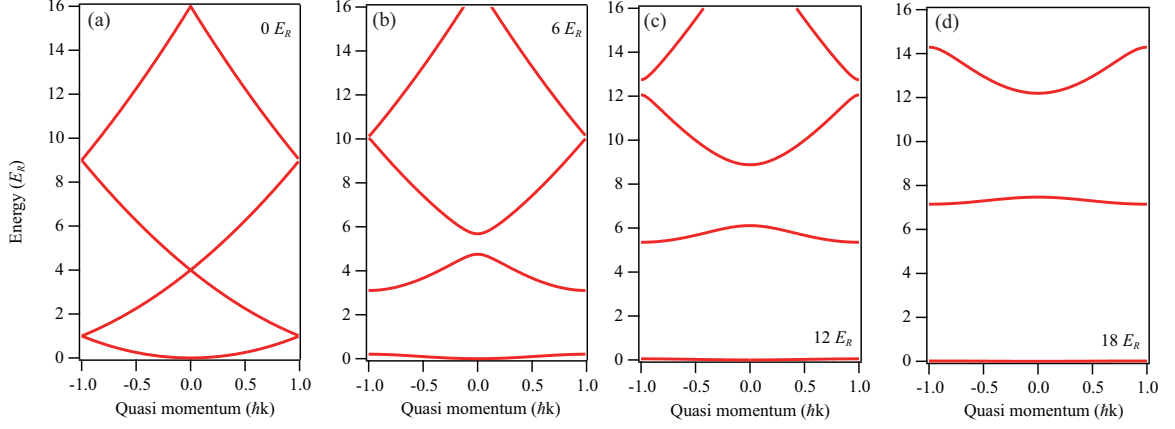


Figure 1.2: Band structures of ultracold atoms in a 1D optical lattice at (a) $u_L = 0E_R$, (b) $u_L = 6E_R$, (c) $u_L = 12E_R$, and (d) $u_L = 18E_R$ (30, 31).

identical to that in free space. We find the bands are continuous and there are no band gaps. As the lattice depth increases, the bands become flatter and the band gaps enlarge. We can also see even in relatively shallow lattices, e.g. $u_L = 12E_R$, the $n = 0$ band is very flat. This implies that the tunnelling rate is low (31).

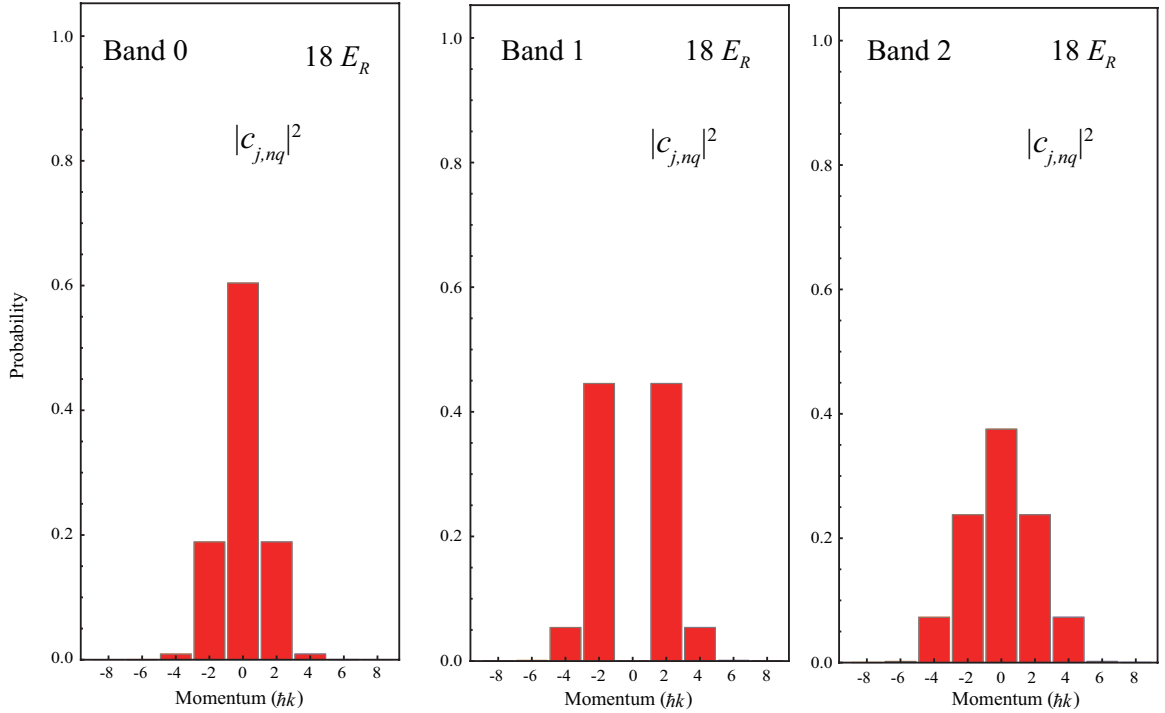


Figure 1.3: The plane-wave decompositions $|c_{j,nq}|^2$ of the Bloch eigenstates for the three lowest bands (a) Band 0 (b) Band 1 (c) Band 2 at $u_L = 18E_R$.

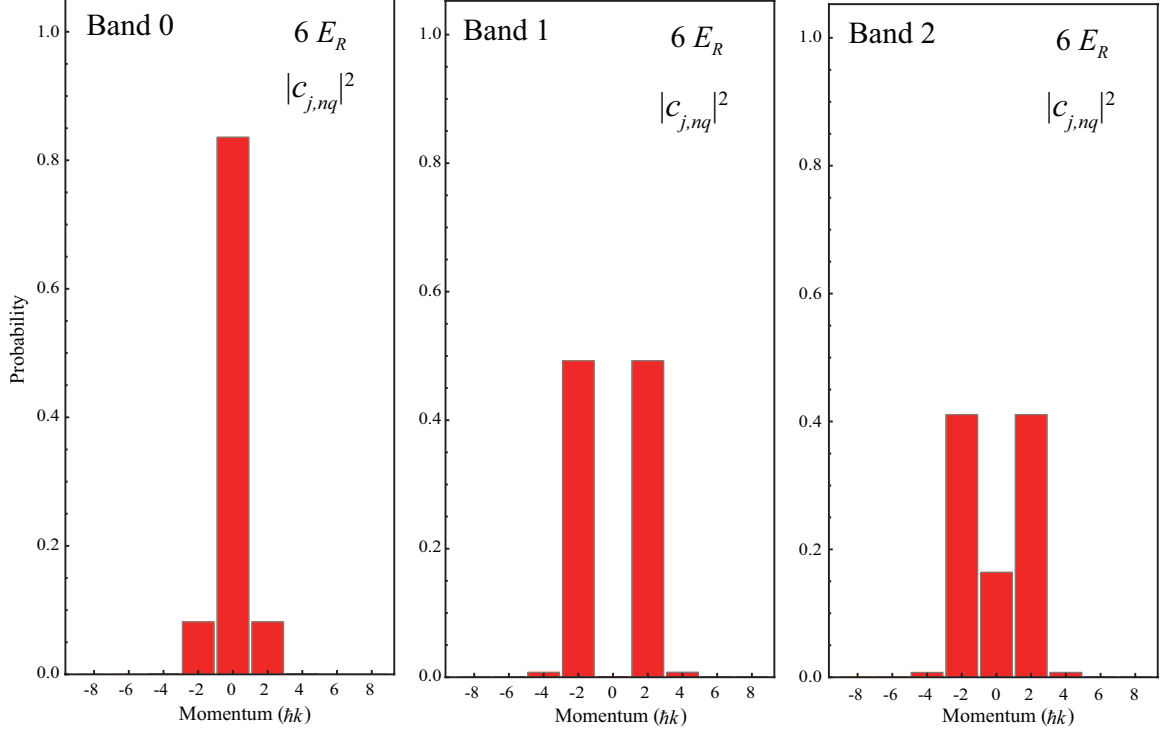


Figure 1.4: The plane-wave decompositions $|c_{j,nq}|^2$ of the Bloch eigenstates for the three lowest bands (a) Band 0 (b) Band 1 (c) Band 2 at $u_L = 6E_R$.

Figure 1.3 and Figure 1.4 show the plane-wave decompositions $|c_{j,nq}|^2$. These plane-wave decompositions are the Bloch eigenstates for the bands $n = 0, 1, 2$ in $q = 0$ and at two different lattice depths $u_L = 18E_R$ and $u_L = 6E_R$, respectively. We can see that the lattice ground state for $n = 0$ and $q = 0$ mainly consists of around 60% zero momentum components, some $-2\hbar k$ momentum components and some $+2\hbar k$ momentum components. For the positive and negative momentum components, they are symmetric and each of them is around 19% at $u_L = 18E_R$. However, for $u_L = 6E_R$, the ground state for $n = 0$ and $q = 0$ consists of around 84% zero momentum components. For the $-2\hbar k$ momentum component and the $+2\hbar k$ momentum component, each of them is only around 8%. Moreover, for different bands, the momentum distributions have large differences. For example, as shown in Fig. 1.3 (a) and (b), the zero momentum component is around 60% for the first band (Band 0 ($n = 0$)), while it is almost 0% for the second band (band 1 ($n = 1$)) at $u_L = 18E_R$ (31).

Since the equation is separable along three orthogonal directions, the wave function can be calculated separately and the energy is simply the sum of the eigenenergies along each direction for three-dimensional cubic lattices.

1.5 Bose-Hubbard model

In 1998, Jaksch *et al.* developed a successful model based on Bose-Hubbard model, which has proved to well explain scalar BECs in optical lattices (32). In their model, the Hamiltonian of lattice-confined scalar BECs can be written as (32)

$$H = \int d^3x \psi^\dagger(x) \left(\frac{-\hbar^2}{2m} \nabla^2 + V(x) \right) \psi(x) + \frac{1}{2} \frac{4\pi a_s \hbar^2}{m} \int d^3x \psi^\dagger(x) \psi^\dagger(x) \psi(x) \psi(x) . \quad (1.19)$$

Here the total potential $V(x)$ includes the periodic lattice potential $V_{\text{lat}}(x)$ and the potential induced by external confinements $V_{\text{ext}}(x)$. Similar to Ref. (32), in relatively deep lattices, we solve this Hamiltonian with wave functions in the Wannier basis. If the energy of the system is less than the energy of the first excited state, we only need to consider Wannier functions $\omega(x - x_i)$ of the lowest energy band. Therefore, the field operator $\psi(x)$ can be expanded as (32)

$$\psi(x) = \sum_i \hat{a}_i \omega(x - x_i) . \quad (1.20)$$

By substituting Eq. (1.20) into Eq. (1.19) and only considering tunnelling among neighboring sites, we can get (32, 33)

$$H = -J \sum_{\langle i,j \rangle} a_i^\dagger a_j + \sum_i (\epsilon_i - \mu) a_i^\dagger a_i + \sum_i \frac{1}{2} U (a_i^\dagger a_i - 1) (a_i^\dagger a_i) . \quad (1.21)$$

The first term describes the tunnelling energy J of atoms among neighboring lattice sites, i.e., $J = \int d\vec{r} \omega_i(\vec{r}) \left(\frac{-\hbar^2}{2m} \nabla^2 + V_{\text{lat}}(r) \right) \omega_j(\vec{r})$ (32), as shown in Fig. 1.5. The second term, $\epsilon_i = \int d\vec{r} |\omega_i(\vec{r})|^2 V_{\text{ext}}(r) \approx V_{\text{ext}}(\vec{r}_i)$ (32), is the energy due to the external confinement. And μ is the chemical potential that acts as a Lagrangian multiplier to fix the average number of particles when the system is considered as a grand canonical ensemble. The last term,



Figure 1.5: The tunnelling energy J (left) and the on-site interaction U (right) in an optical lattice.

$U = \frac{4\pi a_s \hbar^2}{2m} \int d\vec{r} |\omega_i(\vec{r})|^4$ (32), corresponds to the repulsive interaction between two atoms on a single site. For a given optical lattice potential, U and J can be calculated numerically. For instance, for deep lattices, the Wannier function $\omega(x - x_i)$ can be treated as the ground state of a harmonic oscillator, so U and J can be easily calculated. The two parameters, U and J , can be controlled by varying the intensity, direction, and polarization of optical lattice beams. In one regime (i.e., in the shallow lattices where the tunnelling energy is dominating and $J \gg U$), atoms are in the superfluid (SF) phase. In the opposite regime (i.e., in deep lattices where $U \gg J$), atoms are in the Mott-insulator (MI) phase. We can adiabatically change U/J , the ratio of U and J , to realize quantum phase transitions between the superfluid phase and Mott-insulator phases. As atoms are delocalized in the superfluid phase, they can tunnel through different lattice sites and the number of atoms per site fluctuates.

In $F = 1$ spinor BECs, the interaction terms can be written as (34) (The derivations of

Table 1.1: A short list of the reported scattering lengths a_0 and a_2 in the unit of the Bohr radius a_B , and the ratio U_2/U_0 in the ^{23}Na system.

a_0/a_B	a_2/a_B	$U_2/U_0 = (a_2 - a_0)/(a_0 + 2a_2)$	reference
48.91 ± 0.40	54.54 ± 0.20	0.036	(35)
50.00 ± 2.70	55.10 ± 2.70	0.032	(36)
47.36 ± 0.80	52.98 ± 0.40	0.037	(37)
49.90 ± 1.20	55.40 ± 1.20	0.034	(38)
46.00 ± 5.00	52.00 ± 5.00	0.04	(39)

Eqs. (1.22–1.27) are based on Ref. (34).),

$$V_{\text{int}}(r, r') = \delta(r - r')(g_0 P_0 + g_2 P_2) \quad (1.22)$$

Here $g_f = \frac{4\pi\hbar^2 a_f}{m}$. a_f denotes the s-wave scattering length for two atoms with total spin f . f can only be even values, i.e., 0 and 2 for spin-1 atoms. The corresponding projection operator P_f is defined as,

$$P_f = \sum_{m_F=-1}^1 |F, m_F\rangle \langle F, m_F| \quad (1.23)$$

The projection operator P_f satisfies the following two equations:

$$P_0 + P_2 = 1, \quad (1.24)$$

$$F_1 \cdot F_2 = P_2 - 2P_0. \quad (1.25)$$

From Eq. (1.22), Eq. (1.24) and Eq. (1.25), we can get

$$V_{\text{int}}(r, r') = \delta(r - r')(c_0 + c_2 F_1 \cdot F_2) \quad (1.26)$$

with $c_0 = \frac{g_0 + 2g_2}{3}$ and $c_2 = \frac{g_2 - g_0}{3}$ representing the spin-independent and spin-dependent interaction coefficients, respectively. Therefore, we can express c_0 and c_2 as follows,

$$c_0 = \frac{4\pi\hbar^2}{m} \frac{a_0 + 2a_2}{3}, \quad c_2 = \frac{4\pi\hbar^2}{m} \frac{a_2 - a_0}{3}. \quad (1.27)$$

In the Bose-Hubbard model for spinor BECs, the second quantized form of the Hamiltonian

can be given by (34),

$$\begin{aligned}
H = & -J \sum_{\langle i,j \rangle, m_F} a_{i,m_F}^\dagger a_{j,m_F} + \frac{U_0}{2} \sum_i n_i(n_i - 1) - \mu \sum_i n_i \\
& + \frac{U_2}{2} \sum_i (\vec{F}_i \cdot \vec{F}_i - 2n_i) + q_B \sum_{i,m_F} m_F^2 a_{i,m_F}^\dagger a_{i,m_F} .
\end{aligned} \tag{1.28}$$

Here a_{i,m_F}^\dagger and a_{i,m_F} are the creation and annihilation operators of a boson in the m_F hyperfine state at the site i , $m_F = 1, 0$ or -1 , $n_i = \sum_{m_F} a_{i,m_F}^\dagger a_{i,m_F}$ is the total atom number of all the m_F hyperfine states at the site i , and μ is the chemical potential. \vec{F}_i is the spin operator at the site i , which has three components \vec{F}_{ix} , \vec{F}_{iy} , \vec{F}_{iz} satisfying angular momentum commutation rules. In other words, $\vec{F}_{i\alpha} = \sum_{m_F, m'_F} a_{i,m_F}^\dagger (F_\alpha)_{m_F m'_F} a_{i,m'_F}$, $\alpha = x, y$, or z and F_α is the matrix element of the spin-1 angular momentum \vec{F} . U_2 is positive (negative) in antiferromagnetic (ferromagnetic) spinor BECs. Table 1.1 lists various reported experimental and theoretical values of the ratio U_2/U_0 for the ^{23}Na system. In my disseration, most of the discussions are based on $U_2 = 0.04U_0$ (30).

By neglecting the second order term $(a_{i,m_F}^\dagger - \langle a_{i,m_F}^\dagger \rangle)(a_{j,m_F} - \langle a_{j,m_F} \rangle)$ in the hopping energy and applying the decoupling MF theory, Eq. (1.28) can be reduced to a site-independent form (27, 40, 41),

$$\begin{aligned}
H_{\text{MF}} = & \frac{U_0}{2} n(n-1) + \frac{U_2}{2} (\vec{F}^2 - 2n) + q_B \sum_{m_F} m_F^2 n_{m_F} \\
& - zJ \sum_{m_F} (\phi_{m_F}^* a_{m_F} + \phi_{m_F} a_{m_F}^\dagger) + zJ |\vec{\phi}|^2 - \mu n
\end{aligned} \tag{1.29}$$

with the vector order parameter being $\phi_{m_F} \equiv \langle a_{m_F} \rangle$ and z being the number of nearest neighbors. With spatially uniform superfluids in equilibrium, one can assume ϕ_{m_F} to be real, and $\phi_{m_F} = 0$ ($\neq 0$) in the MI (SF) phase.

Comparing with the Hamiltonian of spinor BECs in optical lattices, we can describe a free-space $F=1$ spinor BEC in the Fock space and express the spin-dependent part of its

Hamiltonian as (15, 42, 43)

$$H_{\text{fs}} = \sum_{i,j,k,l=-1}^1 \left[q_B k^2 a_k^\dagger a_k + \frac{c_2}{2} \sum_{\gamma} a_k^\dagger a_i^\dagger (F_{\gamma})_{ij} (F_{\gamma})_{kl} a_j a_l \right]. \quad (1.30)$$

Here a_k (a_k^\dagger) is the annihilation (creation) operator of the $|F = 1, m_F = k\rangle$ state, c_2 is the spin-dependent interaction energy, $F_{\gamma=x,y,z}$ are the spin-1 matrices. The ground state of the free-space spinor BEC is obtained by diagonalizing this Hamiltonian numerically, while the ground state of our sodium spinor BECs in three-dimensional optical lattices can be obtained from the Eq. (1.28). A spin singlet state is a ground state when the quadratic Zeeman energy $q_B = 0$ in free space and in optical lattices. In general, a ground state is an equilibrium state, in which atoms are most stable with the lowest energy. According to the lowest energy principle, the ground state is a preferable state, and the atoms will damp to the ground state after an enough long time duration even if the initial state is not the ground state. If the initial state is the ground state, the atoms will stay at the ground state in an adiabatic experimental process. In thermodynamics, an adiabatic process is defined as a process in which there is no transfer of heat between a system and its surrounding environment. Here the adiabatic concept belongs to the quantum mechanics domain. In quantum mechanics, the adiabatic theorem tells us that if an extra perturbation acts on a system slowly enough and at the same time if there is a gap between the two states, this kind of system will remain in its instantaneous eigenstates. In other words, if the Hamiltonian of a system is changed slowly enough, this physical system will remain in its instantaneous eigenstates. For our experiment, when we ramp up our lattices slowly enough, our system has always stayed in its ground state since we keep the initial state as the ground state before we load the atoms into optical lattices. I will discuss it further in the following chapters.

1.6 Outline

In this dissertation, I mainly focus on results from three of our recent experimental studies on lattice-trapped antiferromagnetic spinor BECs, i.e., the first experimental realization of the first-order SF-MI phase transition, phase diagrams of antiferromagnetic spinor BECs in cubic optical lattices and monoclinic optical lattices, and our efficient experimental scheme to rapidly create spin singlet states.

In Chapter II of this dissertation, I give a short introduction of our experimental setups for creating antiferromagnetic spinor BECs, generating microwave dressing fields and three-dimensional optical lattices.

In Chapter III, I explain how we achieve the first experimental realization of the first-order SF to MI phase transition. I also present our experimental studies on the phase diagrams of antiferromagnetic spinor BECs in three-dimensional cubic optical lattices within a wide range of the quadratic Zeeman energy and the magnetization. The differences between the first-order and second-order SF-MI quantum phase transitions are elaborated in Section 2.1, experimental results are listed in Sections 2.2 and Section 2.3.

Chapter IV discusses the SF-MI phase transition in different lattice geometries, especially in a monoclinic optical lattice. Section 4.1 introduces the theoretical model for monoclinic lattices based on their geometrical relations. Section 4.2 explains how the SF-MI transition point shifts with changes in optical lattice geometries, while Section 4.3 discusses interesting differences induced by the purification of the initial states, especially when the initial states are two polar states, i.e., the longitudinal polar (LP) and transverse polar (TP) states.

In Chapter V, I experimentally demonstrate that combining a cubic optical lattice with a spinor BEC substantially relaxes three strict constraints and brings spin singlets of ultracold spin-1 atoms into experimentally accessible regions. A spin singlet of spin-1 atoms has been widely suggested as an ideal candidate in studying quantum information science, because of its long lifetimes and enhanced tolerance to environmental noises. Via two independent de-

tection methods, we have demonstrated that most of the atoms in the lattice-confined spin-1 spinor BEC form spin singlets, after the atoms cross first-order SF-MI phase transitions near zero field. The last section of this chapter explains how we identify another signature of spin singlets, i.e., confirm their zero spin nematicity in light-scattering measurements. Our simulation results and preliminary experimental idea are also discussed.

In the last chapter, Chapter VI, I will give a brief outlook on our on-going projects and a couple of future directions.

Some parts of this dissertation have been published. Chapter II is based on Refs. (16), Chapter III is based on Refs. (44), and Chapter V is based on Refs. (45). Reprints of these published papers are included in Appendix.

CHAPTER II

EXPERIMENTAL SETUP

This chapter discusses our experimental setups. One paper related to these topics was published:

- L. Zhao, J. Jiang, T. Tang, M. Webb, and Y. Liu, *Dynamics in spinor condensates tuned by a microwave dressing field*, Phys. Rev. A **89**, 023608 (2014).

2.1 Experimental setup for generating sodium BECs

Our BEC apparatus can be divided into five parts: an ultra-high vacuum (UHV) system, a Zeeman slower, a magneto-optical trap (MOT), an optical dipole trap (ODT), and three-dimensional optical lattices. The UHV system is to minimize the collisions between the sodium atoms and other impurity atoms in the vacuum chamber. In our apparatus, we maintain the vacuum pressure at 1×10^{-12} Torr in the main chamber where the MOT and the ODT locate. For obtaining the ultra-high vacuum, we use a turbo pump, three ion pumps, two differential pumping tubes, and a Ti-sublimation pump. The turbo pump directly connected with the sodium oven can only decrease the pressure of the oven chamber to 1×10^{-8} Torr. Multiple laser beams of different frequencies are used for cooling and trapping alkali atoms. Figure 2.1 is a photo showing our optical setup for generating cooling, repumping, slowing, and imaging laser beams. The frequencies of these beams are determined by the hyperfine structure of alkali atoms.



Figure 2.1: Optical setup for generating multiple laser beams used in cooling and trapping sodium atoms.

For alkali atoms, the $3^2S_{1/2} \rightarrow 3^2P_{3/2}$ and $3^2S_{1/2} \rightarrow 3^2P_{1/2}$ transitions belong to fine-structure domain. The fine-structure is the result of the coupling between the spin angular momentum \hat{S} of the electron in the outermost layer and its orbital angular momentum \hat{L} . For alkali atoms, there is only one electron in the outermost layer. Then the total angular momentum \hat{J} of the electron is given by $\hat{J} = \hat{L} + \hat{S}$ and the corresponding quantum number J is in the range of $|L - S| \leq J \leq L + S$. For the ground state of alkali atoms (e.g. ^{23}Na or ^{87}Rb atoms), $L = 0$ and $S = 1/2$. And $J = 1/2$ according to the sum rule of two angular momenta. For the first excited state, $L = 1$, so $J = 1/2$ or $J = 3/2$. The energy level is shifted according to the value of J , so the $L = 0 \rightarrow L = 1$ (D line) transition is split into two components, the D_1 line ($3^2S_{1/2} \rightarrow 3^2P_{1/2}$) and the D_2 line ($3^2S_{1/2} \rightarrow 3^2P_{3/2}$).

The hyperfine structure is a result of the coupling of \hat{J} with the total nuclear angular

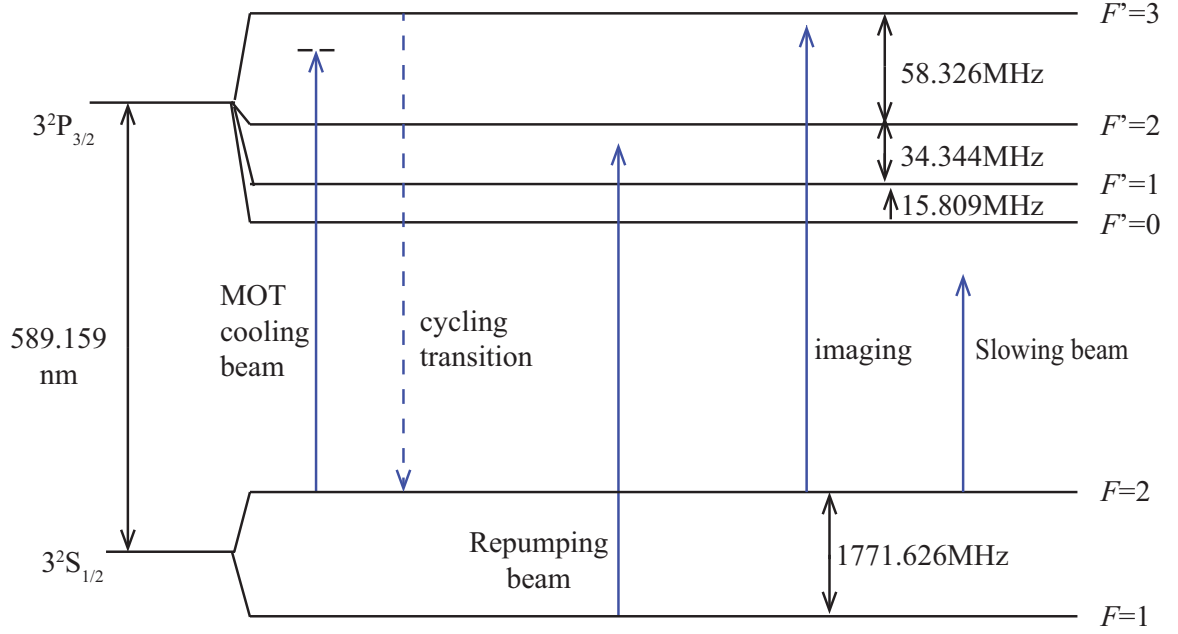


Figure 2.2: The atomic structure (the D_2 line) of a ^{23}Na atom and frequencies of various laser beams used in laser cooling and trapping sodium atoms (46).

momentum \hat{I} . The total atomic angular momentum \hat{F} is then given by $\hat{F} = \hat{J} + \hat{I}$ and the magnitude of \hat{F} is within the range of $|J - I| \leq F \leq J + I$. For the ground state of alkali atoms (e.g. ^{23}Na and ^{87}Rb atoms), $J = 1/2$ and $I = 3/2$, so $F = 1$ or $F = 2$. For the excited state of the D_2 line ($3^2P_{3/2}$), F can take any of the following values: 0, 1, 2, or 3. For the D_1 excited state ($3^2P_{1/2}$), $F = 1$ or 2. Here the energy level is shifted according to the value of F . Figure 2.2 shows the predicted atomic D_2 level of sodium atoms (46).

Figure 2.2 also illustrates the frequencies of various laser beams used for laser cooling and trapping sodium atoms in our system (46). First, the cooling beam is -20 MHz red detuned from the transition $3^2S_{1/2} (|F = 2\rangle) \rightarrow 3^2P_{3/2} (|F' = 3\rangle)$. This transition is a cycling transition, as showed in Fig. 2.2. In this process, atoms are first excited to the $3^2P_{3/2} (|F' = 3\rangle)$ state and then return to the $3^2S_{1/2} (|F = 2\rangle)$ state due to spontaneous emissions. These atoms can be recycled by the cooling laser beam. However, the atoms may decay to the $3^2S_{1/2} (|F = 1\rangle)$ state from the $3^2S_{1/2} (|F = 2\rangle)$ state, therefore we need a repumping beam to pump these atoms back to the $3^2S_{1/2} (|F = 2\rangle)$ state. The repumping beam first excites atoms to the $3^2P_{3/2} (|F' = 2\rangle)$ state and then these atoms will go back

to $3^2S_{1/2}$ ($|F = 2\rangle$) state. Therefore, the repumping beam should be 1713.3 MHz blue-detuned: 1771.626 MHz ($|F = 1\rangle \rightarrow |F = 2\rangle$) -58.326 MHz ($|F' = 2\rangle \rightarrow |F' = 3\rangle$) = 1713.3 MHz. The imaging beam we used is the $F = 2$ imaging, which corresponds to the transition $|F = 2\rangle \rightarrow |F' = 3\rangle$. The slowing beam is -544 MHz red-detuned from the transition $3^2S_{1/2}$ ($|F = 2\rangle$) \rightarrow $3^2P_{3/2}$ ($|F' = 3\rangle$). The cooling beam and the repumping beam are coupled into a 2-in-6-out fiber array. The six output laser beams are arranged as follows, two beams counter propagate in each of the three orthogonal directions. Each pair of counter-propagating beams acts on the atom and creates a force that is proportional to the velocity of atoms. And a pair of anti-Helmholtz coils are placed in the top and bottom recess windows of our main chamber. These two coils are another important part of our MOT. A position dependent force generated by the six cooling beams and the pair of magnetic coils can force the atoms being trapped at the center of our MOT. Only those atoms with appropriate velocities can be captured by the MOT. For increasing the capture efficiency of our MOT, we insert a spin-flip Zeeman slower in front of the main chamber (47).

The crossed optical dipole trap (ODT) consists of two far-detuned 1064 nm laser beams, which can independently confine all three spin components of $F = 1$ atoms. We create spinor BECs through an evaporative cooling in the ODT, i.e., by exponentially lowering the ODT laser beam power. The sketch of our optical dipole trap and an illustration of the evaporative cooling process are shown in Fig. 2.3. In the beginning of an evaporative cooling process, the power of the laser beams is very high. Therefore, a large number of atoms can be confined in the trap. When we decrease the laser power, hot atoms with high energies escape from the trap and eventually the coldest atoms are left in the trap.

2.2 Setup for creating microwave dressing fields

To create sufficiently large negative q , a microwave antenna is placed a few inches above the center of vacuum main chamber. It is designed for a frequency near the $|F = 1\rangle \leftrightarrow |F = 2\rangle$ transition and connected to a microwave amplifier that works between 0.8 GHz to 2 GHz. The output maximum power of this amplifier is 10 W. The microwave function generator

is 8664A made by Agilent, Inc. The frequency range of this generator is very wide, i.e., from 100 kHz to 3 GHz. To amplify the signal, a microwave amplifier ZHL-10W-2G+ from Mini-circuits, Inc. is used. This amplifier works between 0.8 GHz to 2 GHz. In addition, a high isolation switch is used to shut down or turn on the microwave pulse. This switch is controlled by our Labview programs.

According to Eq. 1.8 and Eq. 1.9, the exact value of q is carefully calibrated based on the polarization and frequency of a microwave pulse. Since the resonant Rabi frequency is proportional to the Clebsch-Gordan coefficient of the transition, so we don't need to measure all the 9 Rabi frequencies (16). Generally, we only need to calibrate 3 Rabi frequencies and use the relationships among Rabi frequencies and the known Clebsch-Gordan coefficients to get other 6 Rabi frequencies. In our experiments, we choose the three Rabi frequencies, as shown in Fig. 2.4(a). The resonant Rabi frequencies Ω can be measured by the number of atoms in the $F=2$ state, which is excited by a resonant microwave pulse from the $F=1$ state. The number of atoms oscillates with the microwave pulse duration. A typical example of the Rabi oscillation from $|F=1, m_F=-1\rangle \leftrightarrow |F=2, m_F=-2\rangle$ is shown in Fig. 2.4(b). Here I show two Rabi frequencies measured by using old and new antennas. Since the heating induced by microwave pulses is inversely proportional to the frequency detuning, we replace the old antenna with the new antenna in order to avoid a large amount of microwave-induced heatings. From Fig. 2.4(b), we can see the Rabi frequencies change a lot by using the new antenna. After the replacement, the detuning is shifted by around 20 kHz.

2.3 Experimental setup of three-dimensional optical lattices

After a spinor BEC is created in the ODT, we adiabatically load the BEC into a three-dimensional optical lattice. The setups of our three-dimensional cubic lattices are shown in Fig. 2.5.

Our lattice beams are derived from YLR-30-1064-LP-SF made by IPG Photonics. This is a CW single-mode laser. The maximum output power is 30W. The central wavelength

Table 2.1: Useful parameters of our three-dimensional optical lattices.

lattices	input f (mm)	return f (mm)	fiber	collimator	waist (μm)
Horizontal 1	300	500	Thorlabs	F810APC-1064	60
Horizontal 2	250	500	Toptica	F810APC-1310	
Vertical	300	500	Toptica	F810FC-1064	100

is from 1063.5nm to 1064.5nm. The output linewidth FWHM is around 70kHz and the output beam is linearly polarized. In our experiment, the total power we need is around 2.5W. Before we take data, we need to ensure the three-dimensional lattice beams pass the center of BECs so that the three-dimensional lattices can be balanced well. First, we have to check the position of BECs in the dipole trap and then tune the fine adjustment knobs of the mirror before the vacuum chamber for the input beams and optimize the mirror for the return beams. Finally we need to align the three lattices to the center of BECs, so the differences between the center of BECs and the foci of the lattices are less than one and a half pixels. The periodic potential of lattices in the dipole trap is shown in Fig. 2.6. This 3D lattice is constructed by three optical standing waves at 1064nm, which results in a cubic periodic potential with a lattice spacing of 532 nm. All lattice beams are frequency-shifted by at least 20 MHz with respect to each other for eliminating cross interference among them. The calibration of optical lattice depth u_L is conducted via Kapitza-Dirac (K-D) diffraction patterns and has an uncertainty of $\sim 15\%$. K-D calibration results tell us the power per lattice trap depth in the unit of mW/ E_R . In order to obtain uniform images in the Mott-Insulator phase, the polarization of light need to be stabilized. We set one polarization beamsplitter (PBS) cube to purify the output polarization after the fiber in each lattice beam path. Moreover, in each lattice beam path, we set one liquid crystal half-wave plate. The angle of this kind of waveplates can be controlled by the crystal's driving voltage. Then we connect them to the computer and control them with a proportional–integrate–derivative (PID) feedback control loop with a Labview program. By doing this, the powers of three lattices are stabilized well. Table 2.1 lists some useful parameters of our three-dimensional optical lattices, including the focal lengths f of lens in the input and return beam paths, fibers, collimators, and beam waists. Here the beam

waists are measured by a commercial beam profiler. We can also calculate the beam waists based on the K-D calibrations according to Eq. 1.12, e.g. for the horizontal-1 lattice beam, its waist should be $45.8\mu\text{m}$ (the K-D result is $5.5988\text{ mW}/E_R$); for the horizontal-2 lattice beam, its waist is $68.9\mu\text{m}$ (the K-D result is $12.664\text{ mW}/E_R$); and for the vertical lattice beam, its waist is $67\mu\text{m}$ (the K-D result is $11.959\text{ mW}/E_R$).

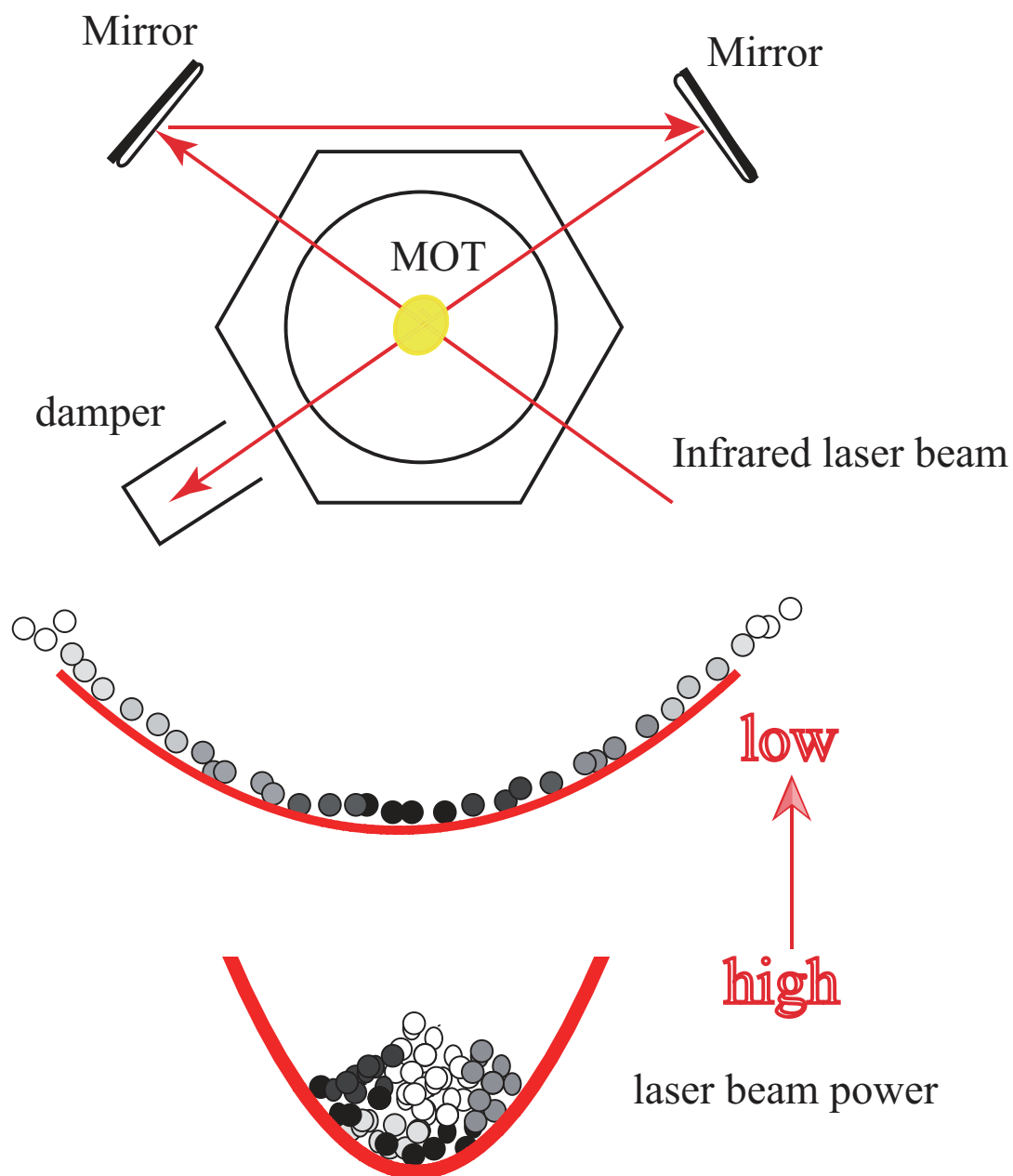


Figure 2.3: The sketch of our dipole trap and an illustration of the evaporative cooling process. The white and black atoms represent atoms with high and low energy, respectively. The energy of the shaded atoms falls in between those of the white and black atoms.

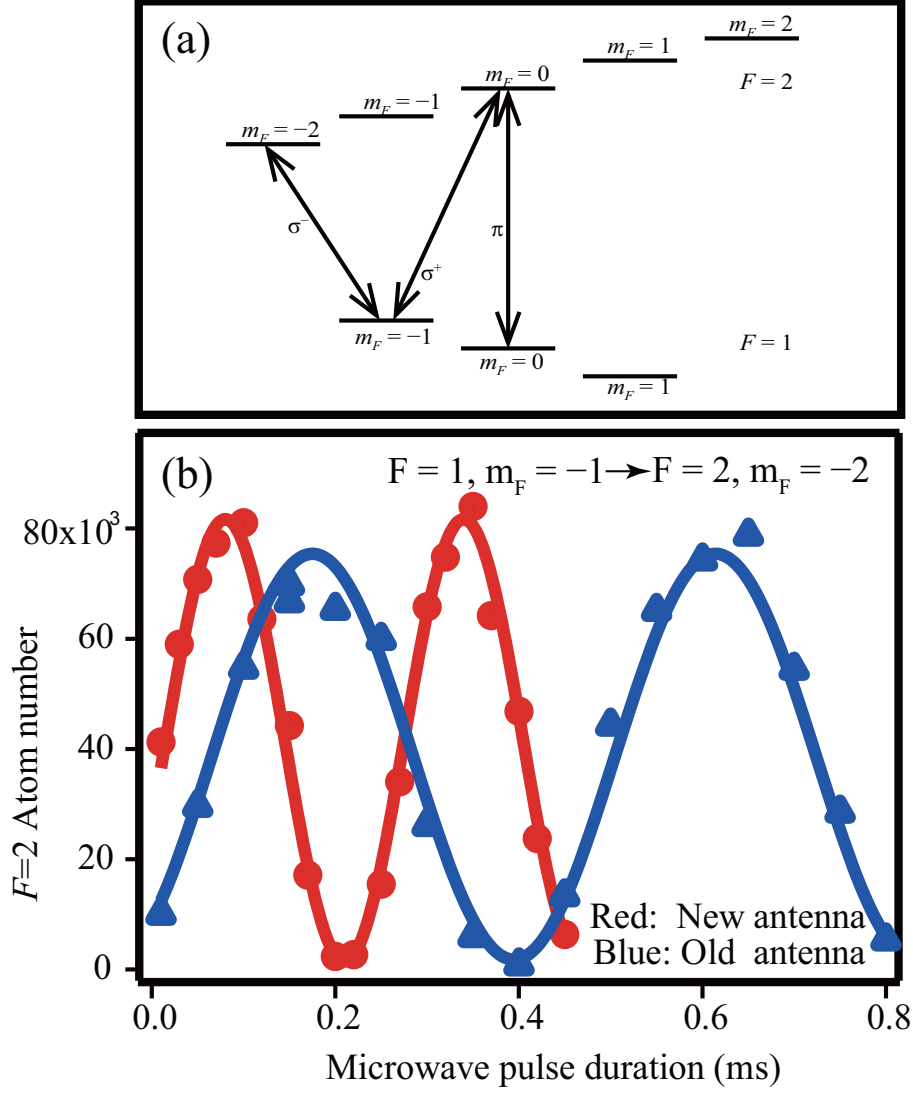


Figure 2.4: (a) The $F = 1$ and $F = 2$ hyperfine structures of the $3^2S_{1/2}$ level in ^{23}Na atoms when an external magnetic field is applied. The three chosen transitions are marked by straight lines with arrows. (b) The number of atoms in the $F = 2$ state excited by a resonant microwave pulse as a function of the pulse duration. The solid lines are sinusoidal fits to extract the on-resonance Rabi frequency Ω of the pulse. Blue and Red colors represent Rabi frequencies measured by using the old antenna and new antenna, respectively.

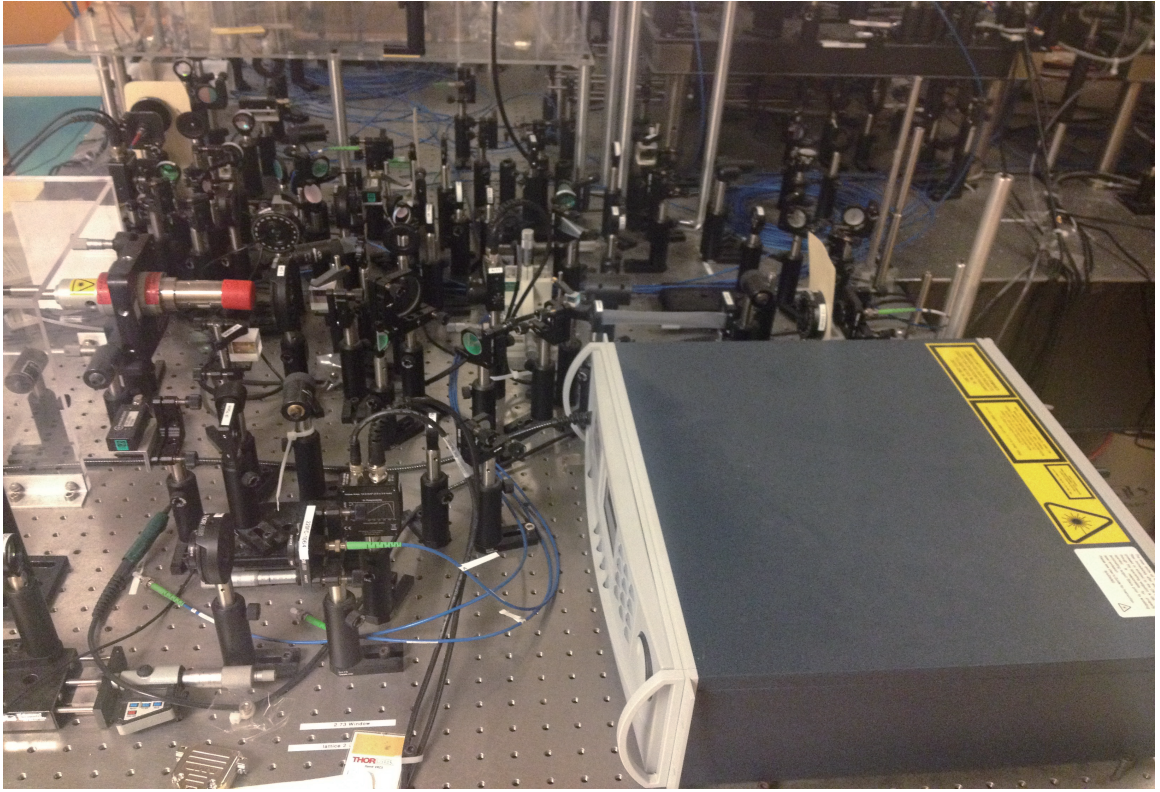


Figure 2.5: Optical setup for three-dimensional lattices.

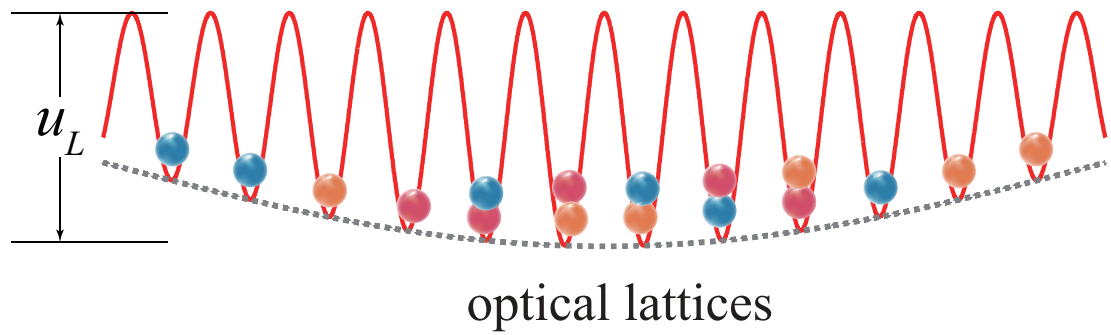


Figure 2.6: The periodic lattice potential in the dipole trap.

CHAPTER III

FIRST-ORDER SUPERFLUID TO MOTT-INSULATOR PHASE TRANSITIONS IN CUBIC OPTICAL LATTICES

This chapter discusses the first-order superfluid to Mott-Insulator phase transition and phase diagrams of antiferromagnetic spinor condensates in three-dimensional cubic lattices. One paper related to these topics was published:

- J. Jiang, L. Zhao, S.-T. Wang, Z. Chen, T. Tang, L.-M. Duan, and Y. Liu, *First-order superfluid-to-Mott-insulator phase transitions in spinor condensates*, Phys. Rev. A **93**, 063607 (2016).

3.1 Superfluid to Mott-insulator phase transition

A phase transition describes a transition among any two of the common phases of matter, e.g., solid, liquid, and gas. Different phases of matter have different physical properties and for one certain phase, the physical property is uniform. In general, phase transitions are divided into two broad categories: first-order phase transitions and second-order phase transitions.

First-order phase transitions are those that associate with extra heatings and the hysteresis effect. A system will either absorb or release a fixed amount of heating across such a transition. During this process, some physical quantities are discontinuous, such as volume, temperature, and pressure. For instance, when a piece of ice melts into the water, its volume

should be changed greatly. A second-order phase transition is also called a continuous phase transition. In other words, physical quantities are continuous before and after the phase transition.

A quantum phase transition from a superfluid (SF) to a Mott-insulator (MI) was realized in a scalar Bose-Einstein condensate (BEC) trapped by three-dimensional (3D) optical lattices around a decade ago (48). This achievement marks an important milestone and has stimulated tremendous efforts to apply highly controllable ultracold bosonic and fermionic systems in studying condensed matter models (15, 26, 28, 49, 50). This kind of phase transitions in scalar BECs is a second-order phase transition. Moreover, the SF-MI transitions have been confirmed in various scalar BEC systems via different techniques that can efficiently control the ratio of interatomic interactions to the mobility of atoms (25, 26, 48, 50). The first method is to use a magnetically tuned Feshbach resonance to manipulate interactions (25). Another more convenient way is to enhance interatomic interactions and suppress atomic motion by raising the depth of an optical lattice (48). A third technique is to control the hopping energy of bosonic atoms by periodically shaking the lattice (50). Spinor BECs, on the other hand, possess an additional spin degree of freedom, leading to a range of phenomena absent in scalar BECs (27, 51, 52, 53, 54, 55, 56). Interestingly, One important prediction is the existence of first-order SF-MI phase transitions in lattice-trapped antiferromagnetic spinor BECs (15, 54, 55, 57, 58, 59, 60, 61), while the SF to MI phase transition in ferromagnetic spinor BECs is second-order (15, 26, 60).

The SF to MI phase transition is controlled by the ratio of the on-site interaction U_0 and the tunnelling J , i.e., when U_0/J reaches a critical value, a transition between SF and MI phases is expected to happen. It can be manipulated by varying the lattice potential u_L . Based on the Hamiltonian shown in Eq. (1.21), the ground state at different μ/U_0 and u_L can be calculated by the mean field (MF) theory. A predicted phase diagram for scalar BECs in simple cubic optical lattices is shown in Fig. 3.1 (a). The Mott lobes decrease with the increase of μ/U_0 . Fig. 3.1 (b) shows the superfluid order parameter ϕ_{SF} versus u_L at $\mu/U_0 = 1.4$ in scalar BECs. We can clearly conclude the change of the order parameter is continuous. This is the feature of second-order transitions.

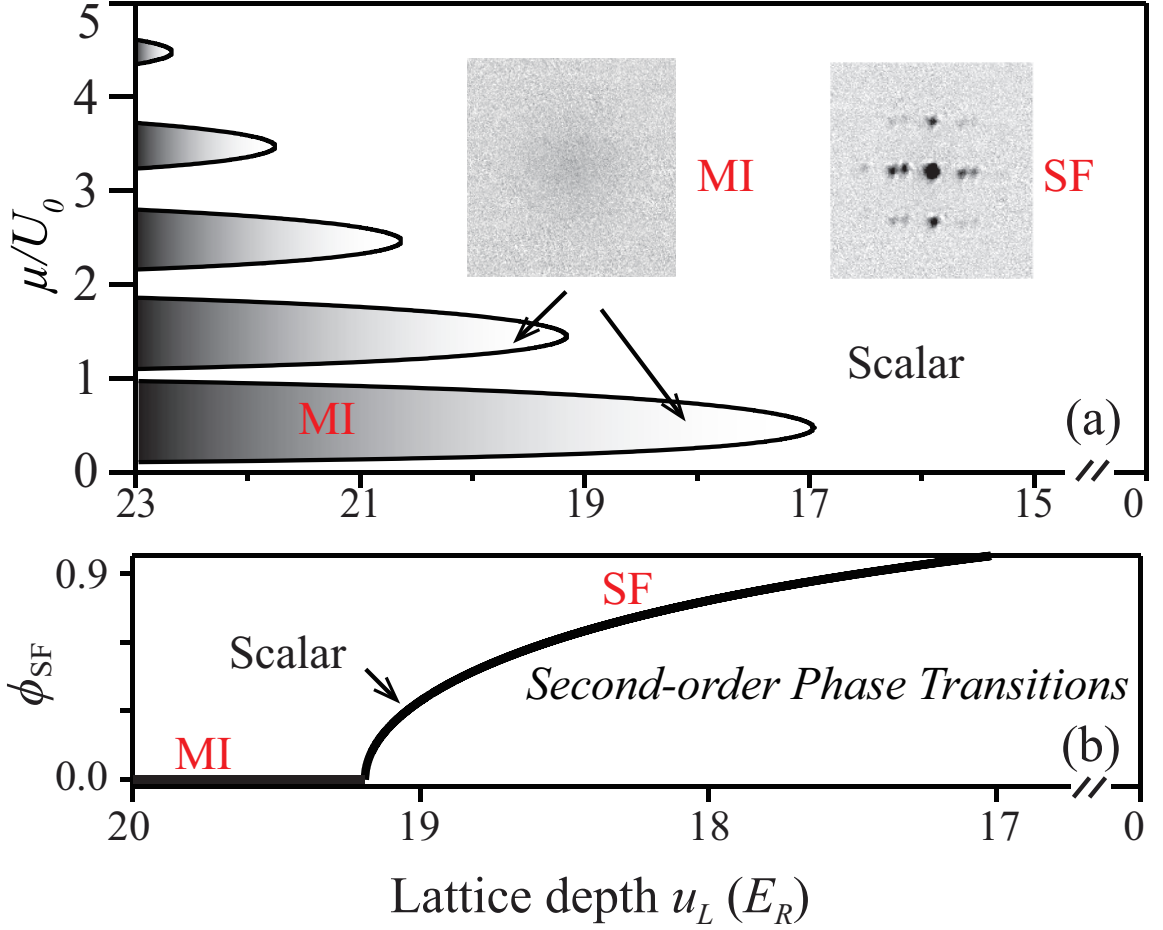


Figure 3.1: (a) MF phase diagrams derived from the BH model for scalar BECs in cubic lattices (33). Inset: two typical TOF pictures shows the SF and MI states. (b) The superfluid order parameter ϕ_{SF} versus u_L at $\mu/U_0 = 1.4$ in scalar BECs.

An antiferromagnetic $F = 1$ spinor BEC of zero magnetization forms a polar superfluid in equilibrium with $\langle \vec{S} \rangle = 0$ (15, 30, 39, 42, 62). There are two types of polar superfluids: the longitudinal polar (LP) state with $(\phi_1, \phi_0, \phi_{-1}) = \sqrt{N_{\text{SF}}}(0, 1, 0)$, and the transverse polar (TP) state with $(\phi_1, \phi_0, \phi_{-1}) = \sqrt{N_{\text{SF}}/2}(1, 0, 1)$. Here N_{SF} is the number of condensed atoms per site. At zero q_B and the same N_{SF} , TP and LP states are degenerate in energy. At $q_B > 0$, the MF ground state is always the LP state, but a meta-stable TP phase may exist (15, 42).

Our MF calculations show that q_B/U_2 is a key factor to understand the nature of SF-MI transitions in antiferromagnetic spinor BECs. At low magnetic fields (where $0 \leq q_B \lesssim U_2$), U_2 penalizes high-spin configurations and enlarges the Mott lobes for even number fillings

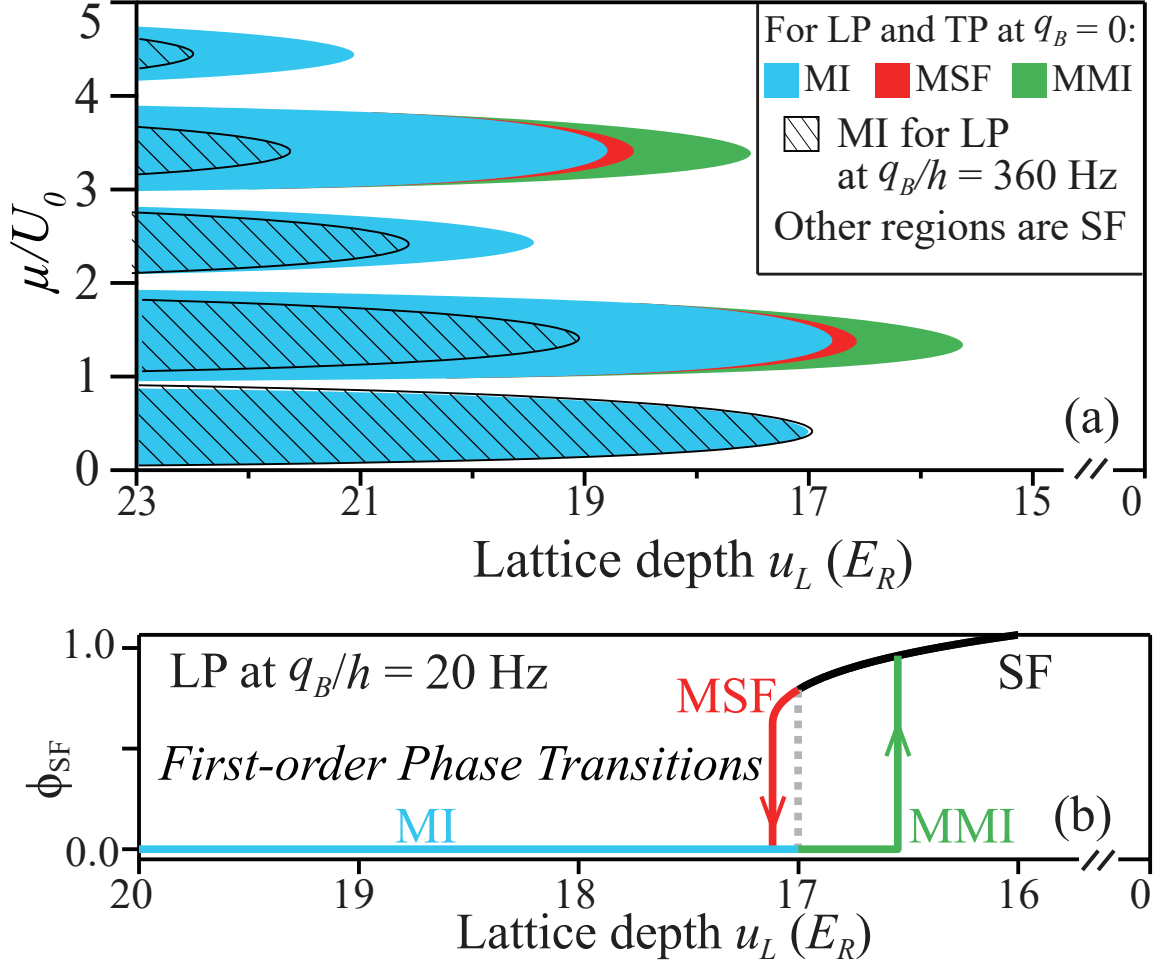


Figure 3.2: (a) MF phase diagrams derived from the BH model for the LP and TP sodium spinor BECs in cubic lattices. (b) The superfluid order parameter ϕ_{SF} versus u_L at $\mu/U_0 = 1.4$ in LP spinor BECs at $q_B/h = 20$ Hz. Here $|\phi_{SF}|^2 = N_{SF}$ and h is the Planck constant.

as atoms can form spin singlets to minimize the energy. The phase diagram for LP and TP states at quadratic Zeeman energy $q_B/h = 0$ Hz which is shown in Fig. 3.2(a). We can obviously see the enlarged Mott lobes except for the filling number $n = 1$.

Moreover, the Meta-stable Mott-insulator (MMI) and meta-stable superfluid (MSF) phases emerge due to the spin barrier, and lead to first-order SF-MI transitions, which is also shown in Fig. 3.2(a) (57, 59, 60, 61). In addition, when the system changes from a meta-stable phase to a stable phase (e.g., from MSF to MI), there will be a jump in the order parameter and the system energy, leading to unavoidable heating to the atoms. When 3D lattices are ramped up and down, hysteresis is expected across the phase transitions.

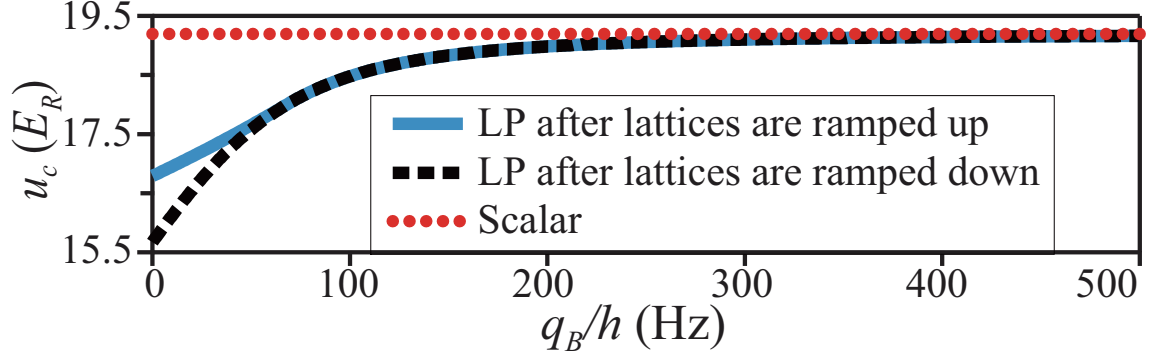


Figure 3.3: Predicted SF-MI transition point u_c versus q_B at $\mu/U_0 = 1.4$ for scalar BECs and LP spinor BECs after lattices are ramped up and down.

Fig. 3.2(b) show the jump in the order parameter and the hysteresis effect for LP spinor BECs at $q_B/h = 20$ Hz. Figs. 3.3 shows the transition lattice depth u_c for ramp up and down sequences in LP and scalar states under different magnetic fields. At high magnetic field for LP state and all the magnetic fields in scalar BECs, the transition point for ramp up and down sequences is the same. It indicates the phase transition is second-order. At low magnetic field, the transition points for ramp up and down sequences are different, which shows the first-order phase transition. Hence, we can see hysteresis, substantial heating, and the formation of spin singlets may be interpreted as signatures of first-order transitions. I will show these experimental signatures in the next section. In Fig. 3.2(a), we can also find the Mott lobes for LP at $q_B/h = 360$ Hz is similar to that in scalar BECs. This is because when q_B increases, the $m_F = 0$ state has lower energy than other m_F levels and U_2 becomes less relevant. When q_B becomes sufficiently larger than U_2 ($U_2/h \lesssim 80$ Hz in this work), the ground state phase diagram of antiferromagnetic spinor BECs reverts back to one that is similar to the scalar BH model with only second-order SF-MI transitions (see Fig. 3.2).

3.2 Signatures of the first-order Superfluid to Mott-insulator phase transitions

In this dissertation, SF-MI transitions are studied in sodium antiferromagnetic spinor BECs confined by cubic optical lattices. We observe hysteresis effect, changes in spin components, and substantial heating across the phase transitions. These indicate the existence of meta-stable states, the formation of spin singlets, and associated first-order transitions. Here, the ratio q_B/U_2 is a key factor I mentioned before, e.g. in the ground state of the spinor BECs, the nature of SF-MI transitions is found to be determined by the competition between the quadratic Zeeman energy q_B and the spin-dependent interaction U_2 . When q_B dominates at high magnetic fields, the transitions appear to be second order and resemble those occurring in scalar BECs (see Fig. 3.1 and Fig. 3.2(a)). In the opposite limit, signatures of first-order transitions are observed. These qualitative features are explained by our mean-field (MF) calculations. We also study the phase transitions with an initial meta-stable state (TP state) and observe stronger heatings across all magnetic fields. Furthermore, our data indicate a new technique to realize SF-MI transitions is by varying q_B . With spatially uniform superfluids in equilibrium, one can assume ϕ_{m_F} to be real. $\phi_{m_F} = 0$ ($\neq 0$) in the MI (SF) phase. Three different types of BECs (i.e., scalar BECs, LP and TP spinor BECs) are studied in this thesis. A scalar BEC containing up to 1.2×10^5 sodium atoms in the $|F = 1, m_F = -1\rangle$ state is created with an all-optical approach similar to Ref. (16). The scalar BEC can be created by imposing a gradient magnetic field. A $F = 1$ spinor BEC of zero magnetization is then produced by imposing a resonant rf-pulse to the scalar BEC at a fixed q_B . Since the LP state (where $\rho_0 = 1$) is the mean-field ground state, it can be prepared by simply holding the spinor BEC for a sufficiently long time at high magnetic fields (42). However, this method is not efficient enough to obtain a very good initial LP state. Another method to generate LP state is by using two resonant microwave pulse to transfer all $m_F = -1$ and $m_F = +1$ atoms to the $F = 2$ state and then blast away these $F = 2$ atoms with a resonant laser pulse. Here ρ_{m_F} is the fractional population of each m_F state. In this and next chapter, we use the first method to generate LP state. The TP

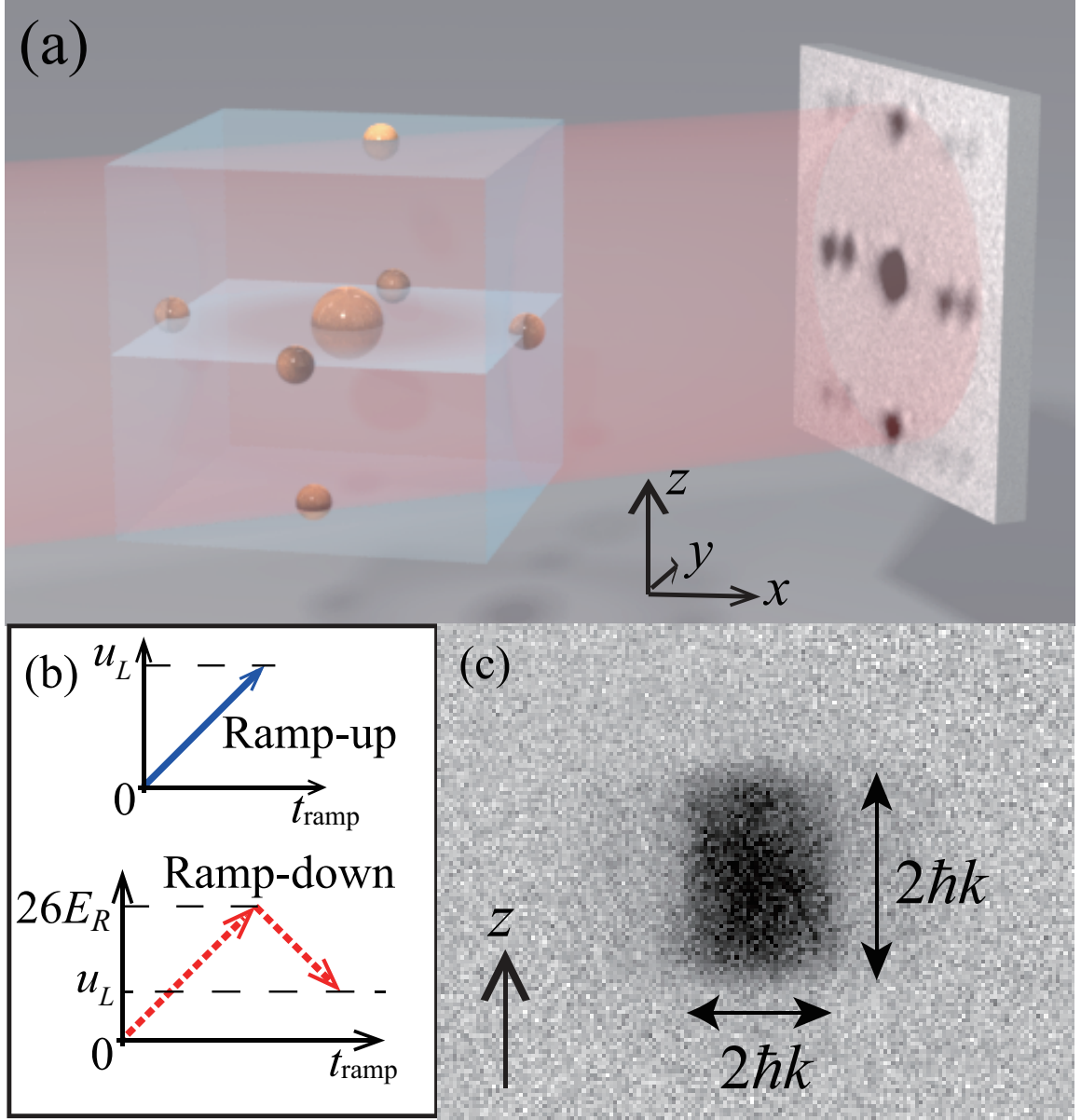


Figure 3.4: (a) Schematic of the reciprocal lattice and a TOF image taken after lattices are abruptly released. The area in red represents the imaging beam. (b) Two lattice ramp sequences used in this chapter. (c) A TOF image showing the first Brillouin zone.

state (where $\rho_{\pm 1} = 0.5$) is generated via a similar approach. The only difference is that here we apply a resonant microwave pulse to transfer all $m_F = 0$ atoms in the $F = 1$ spinor BEC to the $F = 2$ state, and then blast away these atoms. After quenching q_B to a desired value, we adiabatically load the BEC into a cubic optical lattice within time t_{ramp} . As shown in Fig. 3.4(b), lattices are linearly ramped up to a given u_L in a ramp-up sequence, while lattices are first adiabatically ramped up to $26E_R$ and then back down to a variable

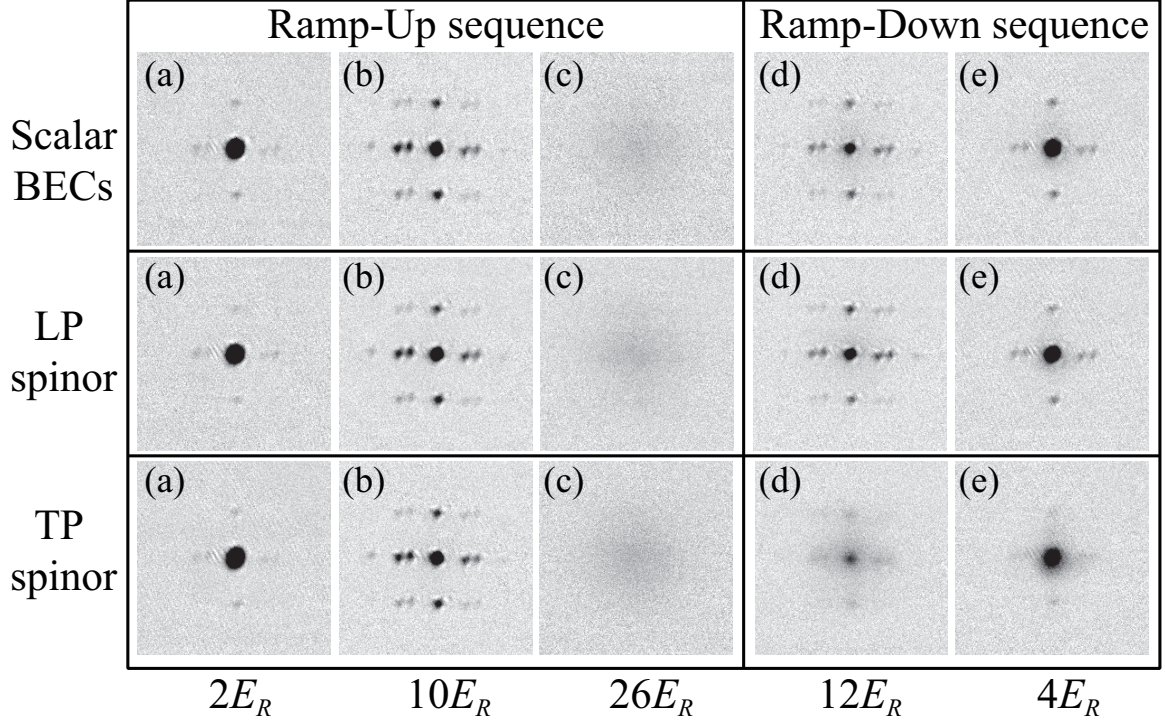


Figure 3.5: Interference patterns observed after we abruptly release scalar (top), LP spinor (middle), and TP spinor BECs (bottom) at various u_L and a 5.5-ms TOF at $q_B/\hbar = 360$ Hz. Panels (a)-(c) are taken after ramp-up sequences to a final $u_L = 2, 10$, and $26E_R$, respectively. Panels (d)-(e) are taken after ramp-down sequences to a final u_L of $12E_R$ and $4E_R$. The field of view is $400\text{ }\mu\text{m} \times 400\text{ }\mu\text{m}$.

final u_L in a ramp-down sequence. Here $E_R = \hbar^2 k_L^2 / (2M)$ is the recoil energy, M and \hbar are respectively the atomic mass and the reduced Planck constant, and k_L is the lattice wave-vector. We find that a ramp speed of $2E_R/\text{ms}$ is sufficient to satisfy the intraband adiabaticity condition and ensure $\geq 80\%$ of atoms remain in a scalar or a high-field LP spinor BEC after a ramp-down sequence to $2E_R$. We measure ρ_{mF} with Stern-Gerlach imaging and microwave imaging after a certain time of flight (TOF).

Distinct interference peaks can always be observed during ballistic expansion, after each BEC is abruptly released from a shallow lattice of $u_L \leq 10E_R$. As shown in the TOF images in Fig. 3.5, the six first-order diffracted peaks are symmetrically set apart from the central peak by a distance corresponding to a momentum of $2\hbar k_L$ along three orthogonal axes. These interference peaks may be considered as evidence for coherence associated with the SF phase. In fact, a larger visibility of interference patterns, a narrower width of the central peak, and a higher optical density (OD) of interference peaks have all been used as

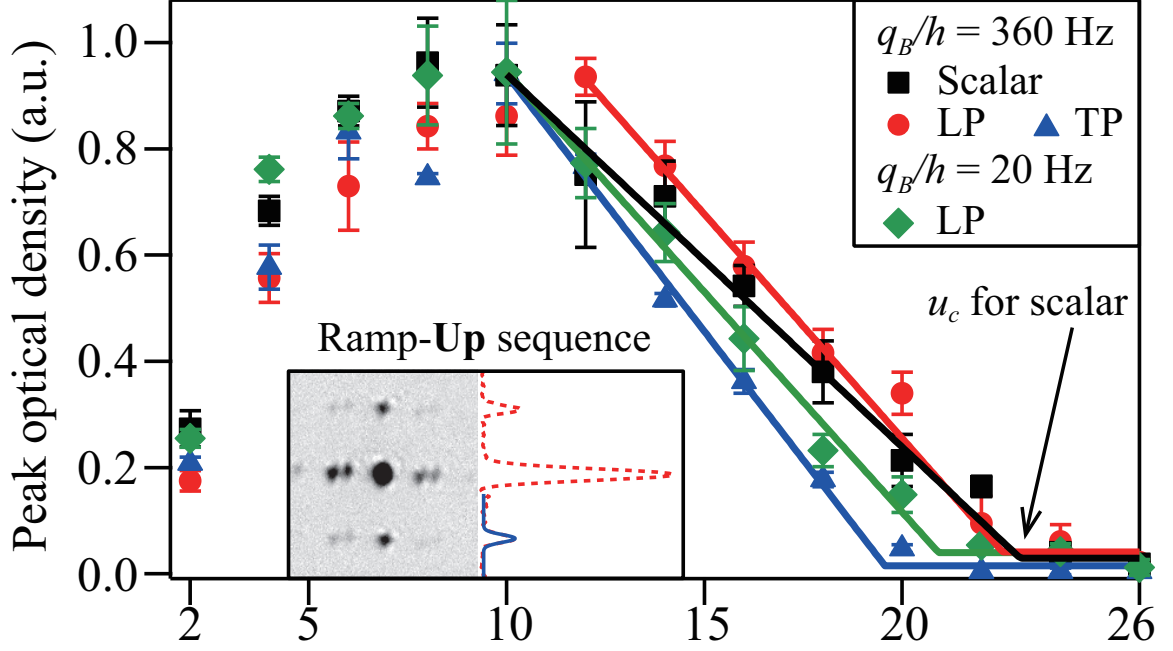


Figure 3.6: Peak OD of interference peaks versus u_L after lattice ramp-up sequences. Markers are experimental data and lines are linear fits. We estimate u_c from the intersection of two linear fits to the data. The inset shows how we extract the peak OD from a TOF image (left). The dotted line in the right inset is a density profile of this TOF image through the central and one pair of interference peaks along the vertical direction, while the solid line is a bimodal fit to one side peak.

trustworthy evidence for improved phase coherence in atomic systems (26, 48, 49, 63).

TOF images in Fig. 3.5 show the loss and revival of the interference contrast in both scalar and spinor BECs as cubic lattices are ramped up and down. A quantitative analysis of these TOF images demonstrates the interference peaks (i.e., coherence associated with the SF phase) change in a reversible manner with u_L (see Fig. 3.6). First, the interference patterns become more visible as lattices are made deeper, and reach their maximum OD around $10E_R$. This may be due to lattice-enhanced density modulation (26, 49, 63). Second, when u_L is further increased and exceeds u_c , the interference peaks steadily smear out to a single broad peak indicating atoms completely lose phase coherence. We extract u_c in Fig. 3.6 and Fig. 3.7 from the intersection of two linear fits to the data of a given BEC. The loss of coherence can be accounted for by many mechanisms, such as heating, inelastic collisions, or entering into a MI state. To confirm the system has undergone a SF-MI transition, we monitor lattice ramp-down sequences, because one characteristic of a MI state has proven

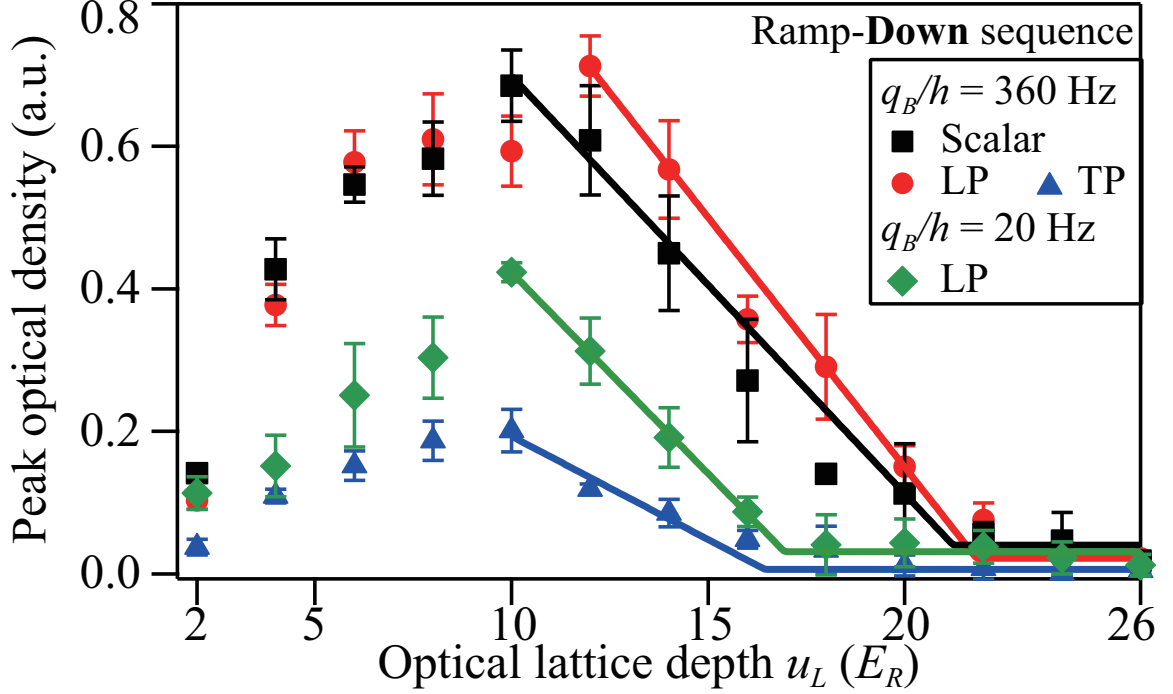


Figure 3.7: Peak OD of interference peaks versus u_L after lattice ramp-down sequences. Markers are experimental data and lines are linear fits. We estimate u_c from the intersection of two linear fits to the data.

to be a loss of phase coherence in deep lattices and a subsequent rapid revival of coherence as u_L is reduced (26, 48, 49). The interference peaks of scalar and spinor BECs reversibly revive after ramp-down sequences, indicating atoms quickly recohere and return to SF states (see Fig. 3.7).

Observations in Fig. 3.6 and Fig. 3.7 are qualitatively consistent with our MF calculations and suggest the existence of first-order SF-MI transitions under some circumstances. First, LP spinor BECs at high magnetic fields possess many properties (e.g., the peak OD) that are similar to those of scalar BECs. Their ramp-up and ramp-down curves are close to each other, while both have roughly symmetric transition points u_c . Similar phenomena were observed in ^{87}Rb and ^6Li systems, and have been considered as signatures of second-order SF-MI transitions (26, 48, 49). Second, LP states at low magnetic fields and TP states at high fields apparently have smaller u_c for both ramp-up and ramp-down processes compared to scalar BECs, suggesting enlarged Mott lobes. Particularly, the ramp-down u_c for LP states at low fields is noticeably smaller than their ramp-up u_c , corroborating with the

MF picture that hysteresis occurs across first-order phase transitions. Third, the recovered interference contrast is visibly different for various BECs after the ramp-down process (after SF-MI transitions). For scalar and high-field LP spinor BECs, nearly 75% of peak OD can be recovered in the interference peaks after ramp-down sequences. The slightly reduced interference contrast may be due to unaccounted heatings, which leads a small portion of atoms ($< 20\%$) to populate the Brillouin zone. Fig. 3.5(c) shows the population within the first Brillouin zones is recorded after the optical lattice depth is adiabatically ramped down and some time of flight. In contrast, after we utilized quite a few techniques and optimized many parameters, the maximal recovered interference contrast of low-field LP states is only $\sim 40\%$ ($\sim 20\%$ for high-field TP states). We attribute this to unavoidable heatings across the first-order transitions as there is a jump in system energy between meta-stable states and stable states. Both hysteresis effect and significant heatings strongly suggest that first-order SF-MI transitions are realized in our experiment. Note, however, we do not see noticeable jumps in the observables as is typically associated with first-order transitions. This is likely due to the presence of even and odd atom fillings in inhomogeneous systems such as trapped BECs, although predicted first-order SF-MI transitions only exist for even occupancy number. Limited experimental resolutions may be another reason.

In addition, our data of the LP state in Fig. 3.7 demonstrate the feasibility of realizing SF-MI transitions via a new approach, i.e., by ramping q_B at a fixed lattice depth. For example, when the final u_L in the ramp-down sequence is set at a value between $17E_R$ and $21E_R$, atoms in the LP spinor BECs can cross the SF-MI transitions if q_B is sufficiently reduced (e.g., from $h \times 360$ Hz to $h \times 20$ Hz). This agrees with the MF prediction in Fig. 3.3: u_c depends on q_B .

Figure 3.8(a) shows the theoretical calculation of the energy gap across the phase transition. These energy gaps lead to significant heatings when atoms cross the SF-MI phase transitions. Figure 3.8(a) indicates that the induced heating in the lattice ramp-down sequence is more than that in the lattice ramp-up sequence. The induced heating in the lattice ramp-up sequence is strongly dependent of q_B , as shown in Fig. 3.8(b). The induced heating should reduce to zero when q_B is large enough, which corresponds to the second-order SF-MI phase

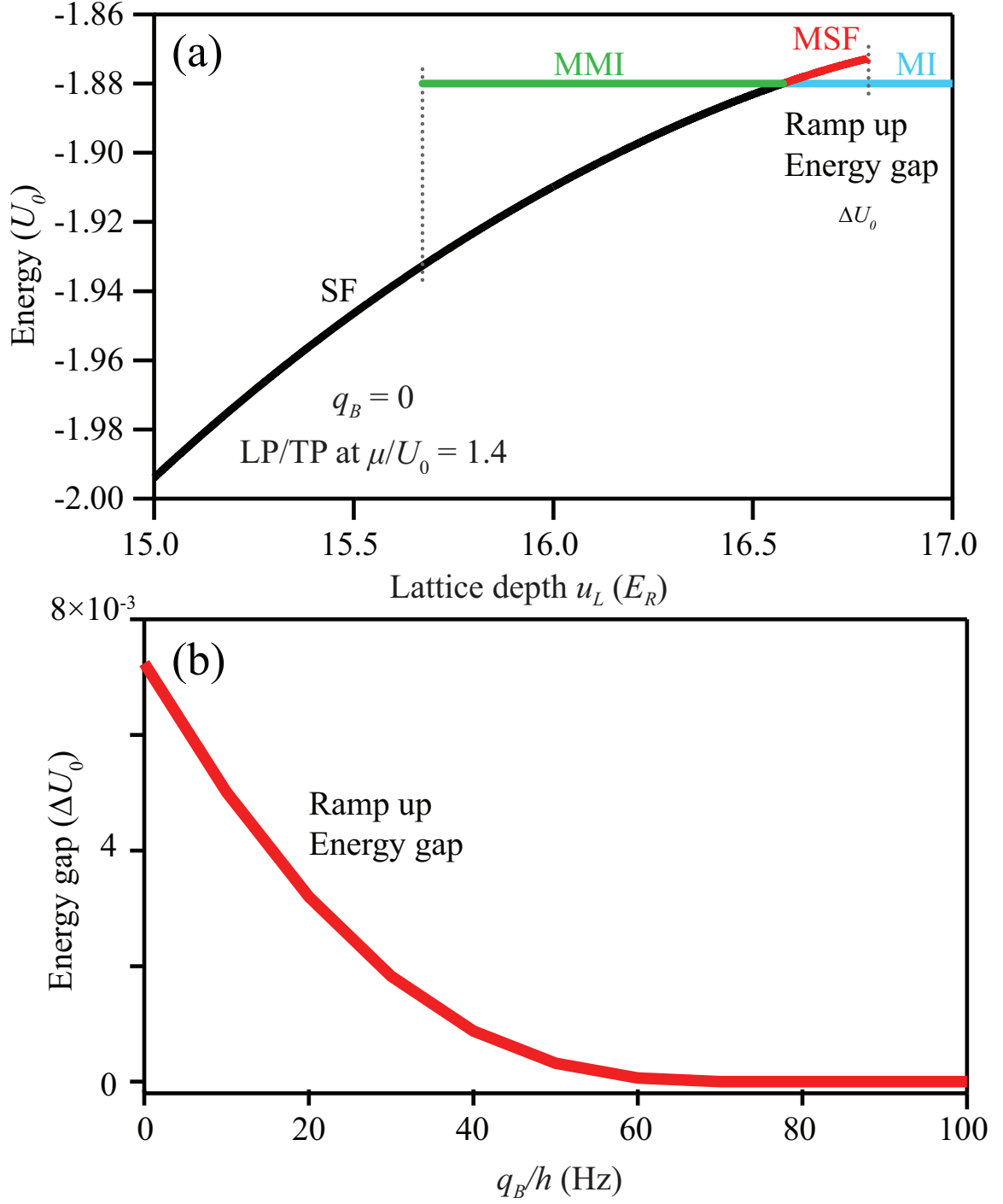


Figure 3.8: (a) Theoretical calculation of the energy gaps across the SF-MI phase transitions. Significant heating, resulted from these energy gaps when atoms cross the phase transitions, is regarded as a signature of the first-order SF-MI phase transitions. (b) The value of the energy gap between MSF and MI state (ramp up sequence) versus q_B .

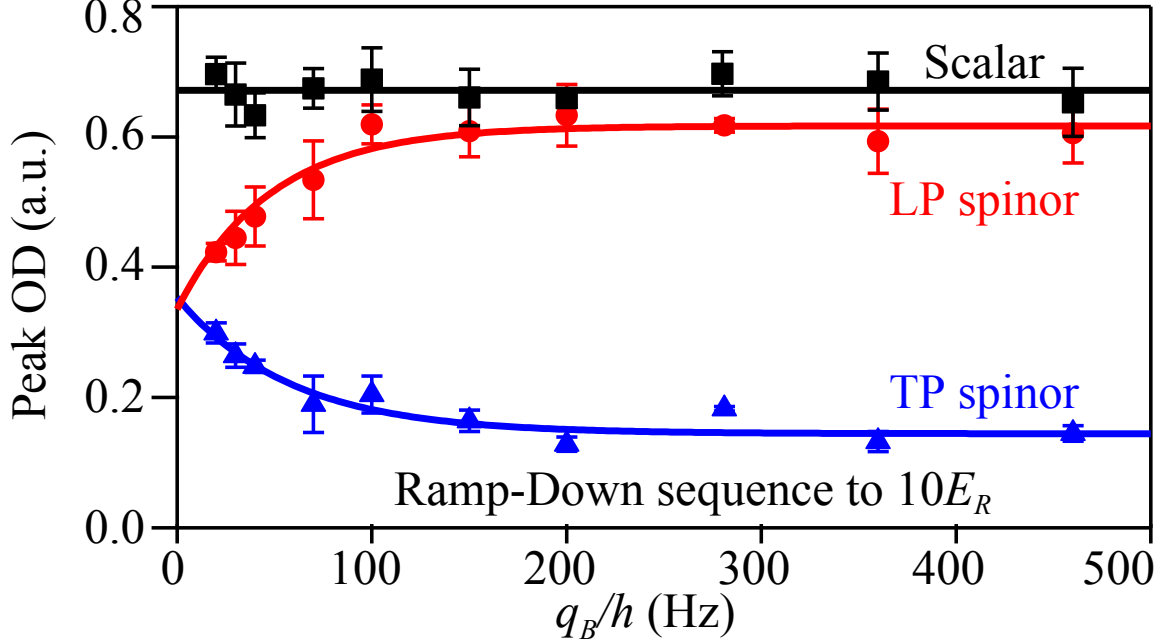


Figure 3.9: Peak OD of interference peaks versus q_B observed after lattice ramp-down sequences to $10E_R$. Markers are experimental data. Red and blue lines are exponential fits. The black line is a linear fit.

transitions.

We then compare scalar and spinor BECs within a wide range of magnetic fields, $20 \text{ Hz} \leq q_B/h \leq 500 \text{ Hz}$, after identical lattice ramp sequences to $u_L = 10E_R$. We choose $10E_R$ because it is apparently the lattice depth around which we observe the maximum interference contrast, with negligible difference in scalar and spinor BECs after ramp-up sequences at all q_B . This is consistent with Fig. 3.1 and Fig. 3.2, which predict all BECs studied in this work should be well in the SF phase at $10E_R$. However, the interference peak ODs show intriguing differences after ramp-down sequences to $10E_R$ (see Fig. 3.9): deviations from the maximal value appear for LP spinor BECs at low magnetic fields and the TP state at all positive q_B . We again attribute this to different amount of heatings across SF-MI transitions. Different extent of heatings may be produced due to different spin barriers as well as the amount of energy jump across the transitions. Hence, the maximum recovered OD is a good indicator for the appearance/disappearance of first-order SF-MI transitions. Notably, LP spinor BECs are found to behave very similarly to scalar BECs when $q_B \gg U_2$ (see Fig. 3.9). This observation is consistent with Fig. 3.3, in which the two MF curves

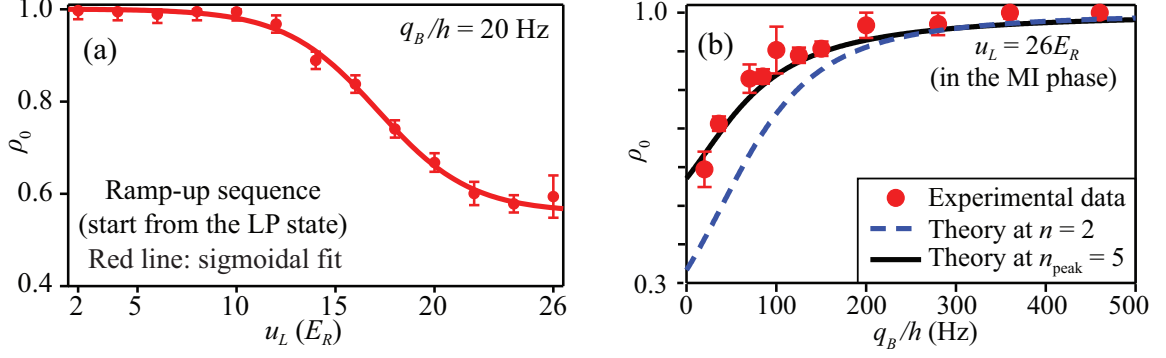


Figure 3.10: (a) Measured ρ_0 versus u_L after an initial LP spinor BEC undergoes ramp-up sequences to various final u_L at $q_B/h = 20$ Hz. The solid line is a sigmoidal fit. (b) Similar to (a) except that we set q_B at various values, and the final u_L at $26E_R$ to ensure atoms enter into the MI phase. The dashed (solid) line represents the MF result for $n = 2$ ($n_{\text{peak}} = 5$).

for the LP state merge indicating that meta-stable states disappear and SF-MI transitions become second order when $q_B/h > 70$ Hz. Furthermore, the difference between LP and TP spinor BECs appears to exponentially decrease as q_B approaches zero. Exponential fits to the data verify that LP and TP spinor BECs should show the same behavior at $q_B = 0$.

Figure 3.10(a) shows the change in the fractional population ρ_0 as the lattice is ramped up, which provides another evidence that is consistent with first-order SF-MI transitions. In the MF picture, the first-order transition is related to the formation of spin singlets in the even Mott lobes. Although the superfluid phase has to be solved numerically, the Mott-insulator phase can be understood analytically in the mean-field picture. This helps us understand the observed change in spin compositions as the depth of the optical lattice is ramped, which is shown in Fig. 3.10(a). The order parameter $\phi_{m_F} = 0$ in the Mott insulator phase, and the single-site Hamiltonian becomes

$$H_{\text{MI}} = \frac{U_0}{2}(n^2 - n) - \mu n + \frac{U_2}{2}(\vec{S}^2 - 2n) + q_B(n_1 + n_{-1}). \quad (3.1)$$

This Hamiltonian can be diagonalized at a fixed atom filling number since the total single-site number operator n commutes with the Hamiltonian. Here we focus on the $n = 2$ lobe, where first-order transitions occur. At $\mu = 1.4U_0$ for example, the ground state is in the $n = 2$ subspace. Other fillings can be solved similarly.

The first two terms in Eq. (3.1) drop off as a constant in the $n = 2$ subspace. Writing the last two terms out, we have

$$H_{\text{MI}}^{n=2} = \frac{1}{2}U_2b_1^\dagger b_1^\dagger b_1 b_1 + \frac{1}{2}U_2b_{-1}^\dagger b_{-1}^\dagger b_{-1} b_{-1} + U_2b_1^\dagger b_0^\dagger b_1 b_0 + U_2b_{-1}^\dagger b_0^\dagger b_{-1} b_0 - U_2b_1^\dagger b_{-1}^\dagger b_1 b_{-1} \\ + U_2b_0^\dagger b_0^\dagger b_1 b_{-1} + U_2b_1^\dagger b_{-1}^\dagger b_0 b_0 + q_B(n_1 + n_{-1}) \quad (3.2)$$

The occupation basis $|\vec{n}\rangle = |n_1, n_0, n_{-1}\rangle$ with $n = 2$ are $|110\rangle, |011\rangle, |200\rangle, |002\rangle, |020\rangle, |101\rangle$.

. The Hamiltonian can be written as a matrix in this basis:

$$H_{\text{MI}}^{n=2} = \begin{pmatrix} U_2 + q_B & 0 & 0 & 0 & 0 & 0 \\ 0 & U_2 + q_B & 0 & 0 & 0 & 0 \\ 0 & 0 & U_2 + 2q_B & 0 & 0 & 0 \\ 0 & 0 & 0 & U_2 + 2q_B & 0 & 0 \\ 0 & 0 & 0 & 0 & 0 & \sqrt{2}U_2 \\ 0 & 0 & 0 & 0 & \sqrt{2}U_2 & -U_2 + 2q_B \end{pmatrix}. \quad (3.3)$$

For $U_2 = 0.04U_0 > 0$ and $q_B > 0$, the ground state energy is

$$E_g = \frac{1}{2} \left(2q_B - U_2 - \sqrt{4q_B^2 - 4q_B U_2 + 9U_2^2} \right), \quad (3.4)$$

and the non-normalized ground state is

$$|\psi_g\rangle = \frac{U_2 - 2q_B + \sqrt{4q_B^2 - 4q_B U_2 + 9U_2^2}}{2\sqrt{2}U_2} |101\rangle - |020\rangle. \quad (3.5)$$

At $q_B = 0$, the Mott insulator ground state is the singlet state $|\psi_g(q_B = 0)\rangle = |S = 0, S_z = 0\rangle = \sqrt{\frac{2}{3}}|101\rangle - \sqrt{\frac{1}{3}}|020\rangle$. This singlet state has equal populations in all three hyperfine levels, i.e., $\rho_0 = \rho_1 = \rho_{-1} = 1/3$. As q_B increases, the amplitude of the $|101\rangle$ state decreases monotonically compared to that of $|020\rangle$. This is observed in the Figure 3.10(b).

Two predictions can be derived from this MF calculation: ρ_0 drastically decreases as atoms cross the first-order transition (from SF to MI) and ρ_0 rises with q_B in the $n = 2$ Mott lobe as well as in our $n_{\text{peak}} = 5$ inhomogeneous system.

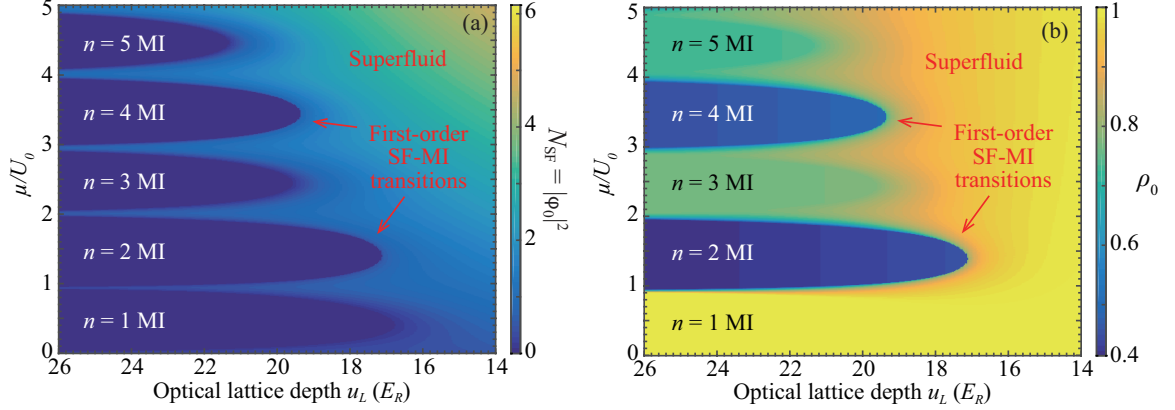


Figure 3.11: (a) N_{SF} and (b) the fractional population ρ_0 of the ground state at various chemical potential μ and lattice depth u_L with $q_B/h = 20$ Hz. Metastable states are not shown in these figures.

Our observations shown in Fig. 3.10(a) may be the first experimental confirmation of these predictions: an initial LP state is found to sigmoidally evolve to a state consisting of all three m_F components as u_L is ramped up at low magnetic fields, with the measured ρ_0 sigmoidally decreasing from one in the SF phase to around 0.6 in the MI phase ($u_L \geq 22E_R$). In addition, in the MI phase, the measured ρ_0 rises with q_B , and approaches one at $q_B \gg U_2$ where the ground state phase diagram of antiferromagnetic spinor BECs resembles the scalar BH model with only second-order SF-MI transitions (see Fig. 3.10(b)). This observation can be well understood by the MF calculation (the $n_{\text{peak}} = 5$ line in Fig. 3.10(b)). Note that the peak filling factor n_{peak} is five in our inhomogeneous system, the data in Fig. 3.10(a) thus represent an average of different atom fillings. In other words, the theoretical $n_{\text{peak}} = 5$ line in Fig. 3.10(b) represents a weighted average of the MF predictions at five different n (i.e., $n = 1, 2, 3, 4, 5$) based on the atom density distribution in a harmonic trap. Good agreements between our data and the MF theory suggest that the observed substantial change in ρ_0 at very low fields may be mainly due to the formation of spin singlets in the even lobe MI phase (after atoms cross the first-order transitions).

Additional predictions can be derived from the mean-field theory. Figure 3.11(a) shows N_{SF} at various chemical potential μ and lattice depth u_L in $q_B/h = 20$ Hz. Here $N_{\text{SF}} = |\phi_0|^2$ is the number of atoms in the superfluid phase on a single lattice site. We can see that $N_{\text{SF}} = |\phi_0|^2 = 0$ in the Mott lobes. The even lobe superfluid (SF) to Mott-insulator (MI)

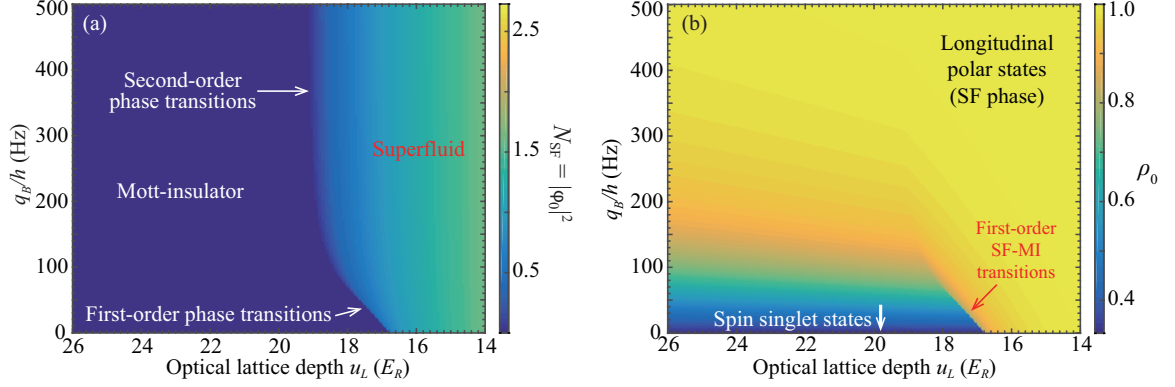


Figure 3.12: (a) N_{SF} and (b) the fractional population ρ_0 of the ground state at various quadratic Zeeman energy q_B and lattice depth u_L with $\mu/U_0 = 1.4$. Metastable states are not shown in these figures.

transition has a sharp boundary due to the first-order transition. Figure 3.2(b) depicts a line at $\mu/U_0 = 1.4$ drawn from this 2D diagram (metastable states are not shown here). Figure 3.11(b) plots ρ_0 at various μ and u_L with $q_B/h = 20$ Hz. Experimental data in Fig. 3.10 represent an average of different chemical potentials from this 2D figure. It can be seen that the change in ρ_0 is mainly due to the formation of spin singlets in the even Mott lobes.

Figure 3.12 shows similar plots at different q_B but fixed chemical potential $\mu/U_0 = 1.4$. We can see that the SF-MI phase transition shifts to a larger lattice depth as q_B increases. This is similar to what is shown in Fig. 3.2 (b) with the effect of metastable states included there. Figure 3.12(b) sketches the change in the fractional population with q_B . The theoretical $n = 2$ line in Fig. 3.10 (b) represents a line at $u_L = 26E_R$ from this 2D diagram. Here n is the occupation number per site. We have also conducted similar calculations at five different n , as shown in Fig. 3.13. The theoretical $n_{\text{peak}} = 5$ line in Fig. 3.10(b) represents a weighted average of the five theoretical curves in Fig. 3.13 based on the atom density distribution in a harmonic trap.

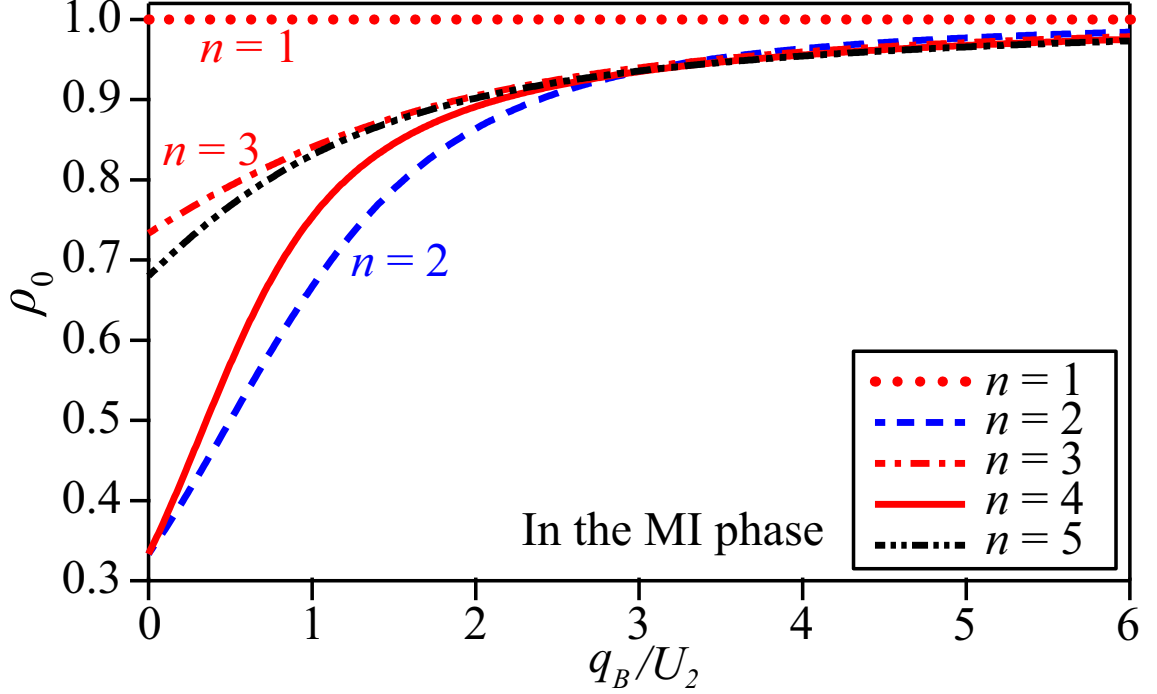


Figure 3.13: ρ_0 of the ground state as a function of q_B/U_2 for five different n (occupation number per site) in the MI phase.

3.3 Phase diagrams of spinor Mott-Insulators

In this section, we will discuss how we experimentally map the ground state phase diagram of antiferromagnetic spinor Bose-Einstein condensates in Mott-Insulator states at different q_B and different magnetizations m .

Since the occupation number in a single lattice site n is fixed in each Mott lobe, we may find the ground states in each Mott lobe separately. For instance, In the second Mott lobe when n equals two, the ground states should be in the $n = 2$ subspace. In this subspace, the occupation basis $|n_{m_F=1}, n_{m_F=0}, n_{m_F=-1}\rangle$ can be $|1, 1, 0\rangle$, $|0, 1, 1\rangle$, $|2, 0, 0\rangle$, $|0, 0, 2\rangle$, $|0, 2, 0\rangle$, and $|1, 0, 1\rangle$. We may then find the ground state by using a trial state

$$\begin{aligned}
 |\psi\rangle = & c_{110}|1, 1, 0\rangle + c_{011}|0, 1, 1\rangle + c_{200}|2, 0, 0\rangle \\
 & + c_{002}|0, 0, 2\rangle + c_{020}|0, 2, 0\rangle + c_{101}|1, 0, 1\rangle
 \end{aligned} \tag{3.6}$$

in this subspace, where c_{110} , c_{011} , c_{200} , c_{002} , c_{020} , and c_{101} are the undetermined coefficients.

We may then express the energy of the trial state $|\psi\rangle$ in the MI states as,

$$\begin{aligned}
E &= \langle \psi | H_{\text{MI}} | \psi \rangle \\
&= U_0 - 2\mu + (U_2 + q_B)(|c_{110}|^2 + |c_{011}|^2) \\
&\quad + (U_2 + 2q_B)(|c_{200}|^2 + |c_{002}|^2) + (2q_B - U_2)|c_{101}|^2 \\
&\quad + \sqrt{2}U_2(c_{101}^*c_{020} + c_{020}^*c_{101}) .
\end{aligned} \tag{3.7}$$

Note that the magnetization $m = (n_{m_F=+1} - n_{m_F=-1})/n$ commutes with H_{MI} and is thus conserved. Therefore, under a certain value of m , we need to require

$$\begin{aligned}
&\langle \psi | n_{m_F=+1} - n_{m_F=-1} | \psi \rangle / 2 \\
&= (|c_{110}|^2 - |c_{011}|^2)/2 + |c_{200}|^2 - |c_{002}|^2 \\
&= m .
\end{aligned} \tag{3.8}$$

In addition, the normalization of $|\psi\rangle$ also requires

$$|c_{110}|^2 + |c_{011}|^2 + |c_{200}|^2 + |c_{002}|^2 + |c_{020}|^2 + |c_{101}|^2 = 1 . \tag{3.9}$$

We may then find the ground states by looking for the minimum value of Eq. 3.7 under the restrictions, i.e., Eqs. 3.8 and 3.9.

First, we divide Eq. 3.7 into two parts, E_1 and E_2 :

$$E = E_1 + E_2 \tag{3.10}$$

$$\begin{aligned}
E_1 &= U_0 - 2\mu + (U_2 + q_B)(|c_{110}|^2 + |c_{011}|^2) \\
&\quad + (U_2 + 2q_B)(|c_{200}|^2 + |c_{002}|^2) ,
\end{aligned} \tag{3.11}$$

$$E_2 = (2q_B - U_2)|c_{101}|^2 + \sqrt{2}U_2(c_{101}^*c_{020} + c_{020}^*c_{101}) . \tag{3.12}$$

For E_1 , under the condition Eq. (3.8), it is easy to see that the minimum of E_1 occurs when $|c_{200}|^2 = m$, $|c_{002}|^2 = 0$, $|c_{110}|^2 = 0$ and $|c_{011}|^2 = 0$ if $m > 0$ or $|c_{200}|^2 = 0$, $|c_{002}|^2 = -m$, $|c_{110}|^2 = 0$ and $|c_{011}|^2 = 0$ if $m < 0$.

In this case, we have

$$|c_{110}|^2 + |c_{011}|^2 + |c_{200}|^2 + |c_{002}|^2 = |m| . \quad (3.13)$$

$$E_{1\min} = U_0 - 2\mu + (U_2 + 2q_B)|m| . \quad (3.14)$$

For E_2 , we suppose

$$|c_{110}|^2 + |c_{011}|^2 + |c_{200}|^2 + |c_{002}|^2 = x . \quad (3.15)$$

Therefore

$$|c_{020}|^2 + |c_{101}|^2 = 1 - x . \quad (3.16)$$

Suppose $c_{101} = a + bi$, $c_{101}^* = a - bi$, $c_{020} = c + di$ and $c_{020}^* = c - di$, then E_2 can be expressed as,

$$E_2 = (2q_B - U_2)(a^2 + b^2) + \sqrt{2}U_2(ac + bd) . \quad (3.17)$$

and Eq. 3.16 can be rewritten as,

$$a^2 + b^2 + c^2 + d^2 = 1 - x . \quad (3.18)$$

Under the restriction of Eq. 3.18, we construct a new function by using the Lagrange multiplier method as,

$$\begin{aligned} E^* = & (2q_B - U_2)(a^2 + b^2) + \sqrt{2}U_2(ac + bd) \\ & + \lambda(a^2 + b^2 + c^2 + d^2 + x - 1) . \end{aligned} \quad (3.19)$$

Here λ is the Lagrange multiplier.

We require

$$\frac{\partial E^*}{\partial a} = (2q_B - U_2)2a + 2\sqrt{2}cU_2 + 2\lambda a = 0 \quad (3.20)$$

$$\frac{\partial E^*}{\partial b} = (2q_B - U_2)2b + 2\sqrt{2}dU_2 + 2\lambda b = 0 \quad (3.21)$$

$$\frac{\partial E^*}{\partial c} = 2\sqrt{2}aU_2 + 2\lambda c = 0 \quad (3.22)$$

$$\frac{\partial E^*}{\partial d} = 2\sqrt{2}bU_2 + 2\lambda d = 0 . \quad (3.23)$$

On the basis of the aforementioned four equations, we can obtain

$$\frac{a}{c} = \frac{b}{d} = \frac{1}{2} \left[\frac{2q_B - U_2}{\sqrt{2}U_2} \pm \sqrt{4 + \frac{(2q_B - U_2)^2}{2U_2^2}} \right] . \quad (3.24)$$

Then we can derive

$$\begin{aligned} |c_{020}|^2 &= c^2 + d^2 \\ &= \frac{-2q_B + U_2 + \xi}{2\xi} (1 - x) \text{ or} \\ &= \frac{2q_B - U_2 + \xi}{2\xi} (1 - x) \end{aligned} \quad (3.25)$$

and

$$\begin{aligned} |c_{101}|^2 &= 1 - |m| - |c_{020}|^2 \\ &= \frac{2q_B - U_2 + \xi}{2\xi} (1 - x) \text{ or} \\ &= \frac{-2q_B + U_2 + \xi}{2\xi} (1 - x) . \end{aligned} \quad (3.26)$$

Here $\xi = \sqrt{4q_B^2 - 4q_B U_2 + 9U_2^2}$.

Since $\xi > |2q_B - U_2|$ and $\xi > 0$, we then express c_{020} and c_{101} as,

$$\begin{aligned} c_{020} &= \sqrt{\frac{-2q_B + U_2 + \xi}{2\xi}} \sqrt{1 - xe^{i\theta_1}} \text{ or} \\ &= \sqrt{\frac{2q_B - U_2 + \xi}{2\xi}} \sqrt{1 - xe^{i\theta_1}} \end{aligned} \quad (3.27)$$

and

$$\begin{aligned} c_{101} &= \sqrt{\frac{2q_B - U_2 + \xi}{2\xi}} \sqrt{1 - xe^{i\theta_2}} \text{ or} \\ &= \sqrt{\frac{-2q_B + U_2 + \xi}{2\xi}} \sqrt{1 - xe^{i\theta_2}} . \end{aligned} \quad (3.28)$$

The solutions above are only the extreme points and they may not be the minimum point. Therefore, we need to substitute the values of c_{020} and c_{101} into Eq. 3.12 to check them. Finally, we find $c_{020} = \sqrt{\frac{2q_B - U_2 + \xi}{2\xi}} \sqrt{1 - xe^{i\theta_1}}$ and $c_{101} = \sqrt{\frac{-2q_B + U_2 + \xi}{2\xi}} \sqrt{1 - xe^{i\theta_2}}$ correspond to the minimum of E_2 . Here $\theta_2 - \theta_1 = (2k + 1)\pi$, $k \in Z$.

And the minimum of E_2 is

$$E_{2\min}^* = (2q_B - U_2 - \xi) \frac{1 - x}{2} . \quad (3.29)$$

In order to meet the condition of Eqs. 3.8 and 3.15, we require $x \geq |m|$. When $x = |m|$, E_2 reaches its minimum:

$$E_{2\min} = (2q_B - U_2 - \xi) \frac{1 - |m|}{2} \leq E_{2\min}^* . \quad (3.30)$$

Note that $x = |m|$ agrees with Eq. 3.13, we can combine Eqs. 3.30 and 3.14. So the ground state energy may thus be expressed as follows,

$$E_g = \frac{1 - |m|}{2} (2q_B - U_2 - \xi) + |m| (U_2 + 2q_B) + U_0 - 2\mu , \quad (3.31)$$

and the coefficients of the ground state $|\psi_g\rangle$ may be written as,

$$\begin{aligned}
c_{110} &= c_{011} = 0 \\
|c_{200}|^2 &= \max(m, 0) \\
|c_{002}|^2 &= \max(-m, 0) \\
c_{020} &= \sqrt{1 - |m|} \sqrt{\frac{2q_B - U_2 + \xi}{2\xi}} e^{i\theta_1} \\
c_{101} &= \sqrt{1 - |m|} \sqrt{\frac{U_2 - 2q_B + \xi}{2\xi}} e^{i\theta_2} .
\end{aligned} \tag{3.32}$$

Here $\theta_2 - \theta_1 = (2k + 1)\pi$ and $k \in Z$.

By applying Eq. 3.32, ρ_0 , the fractional population of the $m_F = 0$ state in the ground states, may be written as,

$$\rho_0 = \langle \psi_g | n_{m_F=0} | \psi_g \rangle / 2 = (1 - |m|) \frac{2q_B - U_2 + \xi}{2\xi} . \tag{3.33}$$

In low magnetic fields where $q_B \ll U_2$, Eq. 3.33 gives $\rho_0 = (1 - |m|)/3$, $\rho_{+1} = \max(m, 0) + (1 - |m|)/3$, and $\rho_{-1} = \max(-m, 0) + (1 - |m|)/3$. In the opposite limit, i.e., high magnetic fields when $U_2 \ll q_B$, we find $\rho_0 = (1 - |m|)$, $\rho_{+1} = \max(m, 0)$, and $\rho_{-1} = \max(-m, 0)$.

The ground states in other Mott lobes can be solved similarly. Since the peak n is five in our system, we thus plot a weighted average of ρ_0 of the first five Mott lobes based on the atom density distribution in a harmonic trap, as shown in Fig. 3.14. We can find our experimental values (Fig. 3.14(a)) agree with the mean field prediction for $n_{\text{peak}} = 5$ (Fig. 3.14(c)) well.

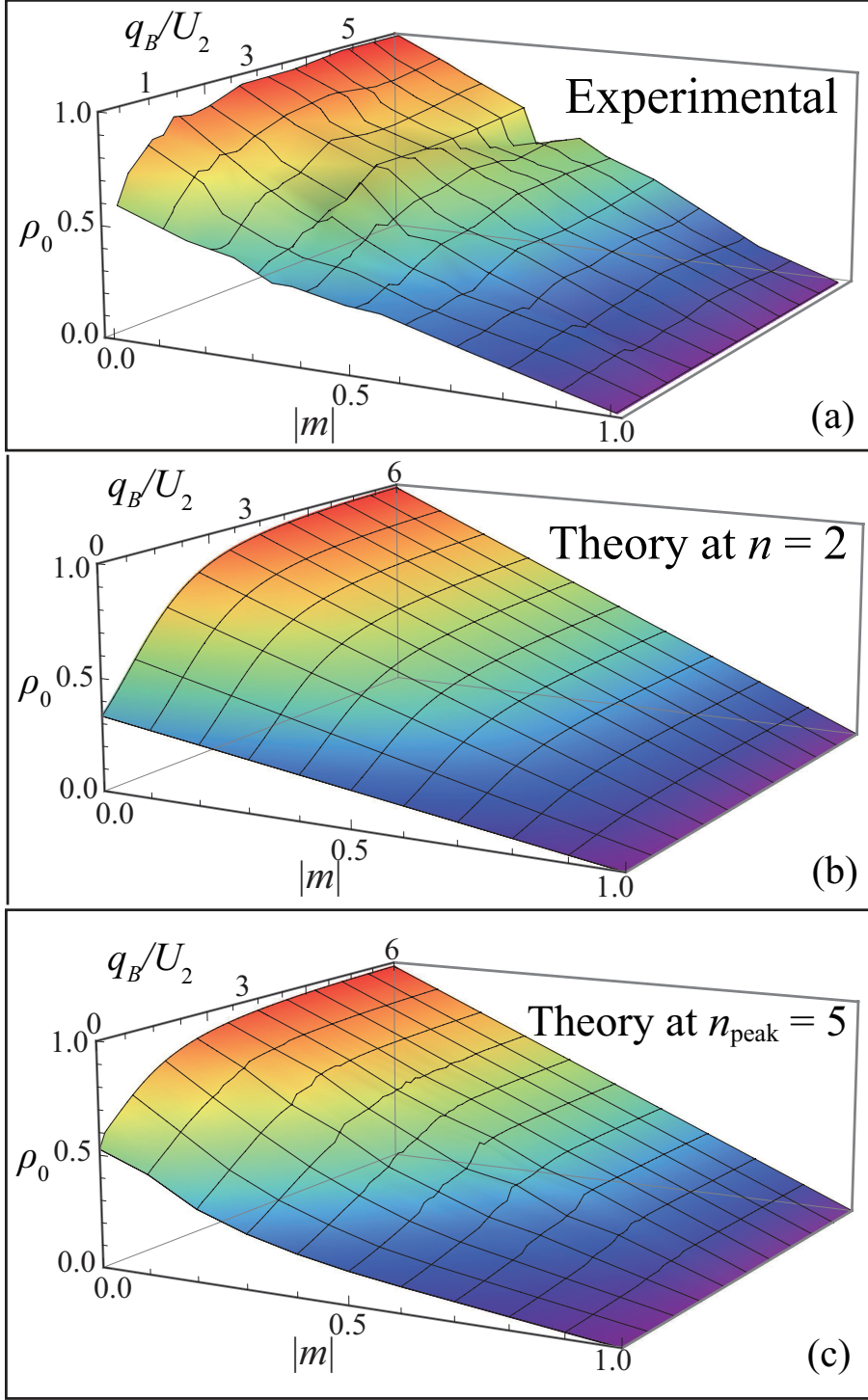


Figure 3.14: (a) Experimental ρ_0 in the ground state at various q_B/U_2 and magnetizations m in cubic lattices. (b) The predicted ρ_0 for $n = 2$ in the ground state at various q_B/U_2 and m . (c) The predicted ρ_0 for $n_{\text{peak}} = 5$ in the ground state at various q_B/U_2 and m .

CHAPTER IV

FIRST-ORDER SUPERFLUID TO MOTT-INSULATOR PHASE TRANSITIONS IN THREE-DIMENSIONAL MONOCLINIC LATTICES

This chapter discusses the superfluid to Mott-Insulator phase transition in spinor condensates confined in three dimensional monoclinic lattices.

Some published works have emphasized the effect of lattice geometries on the behavior of lattice-confined BECs (51, 53, 64, 65). However, they all focus on two-dimensional optical lattices. Though three-dimensional (3D) simple cubic lattices have been widely discussed, 3D lattices with different geometries remain less explored. For example, simply altering the angle θ between two horizontal beams in a 3D lattice setup can significantly change the value of the on-site interaction energy U_0 and the hopping energy J . In this chapter, we construct a 3D lattice geometrical model, which takes into account the effect of the angle θ between the two horizontal lattice beams. Based on this model, we build our monoclinic lattices with the angle of $\theta = \pi/4$. We find that the SF-MI transition point in our monoclinic lattices is less than that in cubic lattices. By taking into account the relation between our monoclinic and cubic lattices in our model, the experimental data are consistent with each other. We also discuss the change of ρ_0 (the fraction of atoms in the $m = 0$ hyperfine state) in our monoclinic lattices, i.e., ρ_0 lowers when we decrease magnetic fields or increase the final trap depth of ramp-up sequences. The results due to the formation of spin singlet pairs are similar to that observed in the cubic lattice experiments. The experimental results also coincide well for our monoclinic and cubic lattices based on our model and agree with the prediction of the mean-field theory.

4.1 Theoretical model

Here, we first theoretically discuss the relation of the J , U_0 with the angle θ between the two horizontal lattice beams (see Fig. 4.1(b)). The lattice potential for arbitrary θ is given as

$$V_T = 4V_s[\sin^2(ky) + \sin^2(ky \cos \theta - kx \sin \theta) + \sin^2(kz)] . \quad (4.1)$$

Since the square of optical trap frequencies is proportional to the second order derivative of the lattice potential, optical trap frequencies along the different directions are as follows,

$$\omega_{T_x} = \omega_{T_\eta} = \omega_c \sin \theta , \quad \omega_{T_y} = \omega_c \sqrt{1 + \cos^2 \theta} , \quad \omega_{T_z} = \omega_c . \quad (4.2)$$

The harmonic length $\beta = \sqrt{\frac{\hbar}{m\omega}}$ in monoclinic lattices can be written as,

$$\beta_{T_x} = \beta_{T_\eta} = \beta_c (\sin \theta)^{-1/2} , \quad \beta_{T_y} = \beta_c (\sqrt{1 + \cos^2 \theta})^{-1/2} , \quad \beta_{T_z} = \beta_c . \quad (4.3)$$

The nearest neighboring site distance a in monoclinic lattices can be written as,

$$a_{T_x} = a_{T_\eta} = a_c / \sin \theta , \quad a_{T_z} = a_c . \quad (4.4)$$

Here the subscripts T, c respectively stand for monoclinic and cubic lattices. The subscripts x, η stand for the two horizontal reciprocal lattices directions. The three directions x, y, z are orthogonal with each other (see Fig. 4.1(b)). $\omega_c = \sqrt{\frac{16V_s E_R}{\hbar^2}}$, the recoil energy $E_R = \frac{\hbar^2 k^2}{2m}$, m and \hbar are respectively the atomic mass and the reduced Planck constant, and k is the lattice wave-vector.

The geometrical mean of the trap frequency ω and the harmonic length β in monoclinic

lattices can be written as,

$$\begin{aligned}\overline{\omega_T} &= \sqrt[3]{\omega_{T_x}\omega_{T_y}\omega_{T_z}} = \omega_c(\sin\theta\sqrt{1+\cos^2\theta})^{1/3}, \\ \overline{\beta_T} &= \beta_c(\sin\theta\sqrt{1+\cos^2\theta})^{-1/6}.\end{aligned}\quad (4.5)$$

According to Refs. (32, 66), the on-site interaction U_0 and the hopping energy J can be written as follows,

$$U_0 = \frac{2\hbar\overline{\omega}}{\sqrt{2\pi}} \frac{a_s}{\overline{\beta}} \propto \frac{\overline{\omega}}{\overline{\beta}}, \quad (4.6)$$

$$J = \frac{\hbar\overline{\omega}}{8} \left[1 - \left(\frac{2}{\pi} \right)^2 \right] \left(\frac{a}{\overline{\beta}} \right)^2 e^{-\frac{1}{4} \left(\frac{a}{\overline{\beta}} \right)^2} \propto \overline{\omega} \left(\frac{a}{\overline{\beta}} \right)^2 e^{-\frac{1}{4} \left(\frac{a}{\overline{\beta}} \right)^2}. \quad (4.7)$$

Then the relation between J_T and J_c along the two reciprocal lattice directions can be written as,

$$J_{T_x} = J_{T_\eta} = \frac{\exp[-\frac{1}{4}(\frac{1}{\sin\theta} - 1)(\frac{a_c}{\beta_c})^2]}{(\sin\theta)^{2/3}(1+\cos^2\theta)^{-1/6}} J_c, \quad (4.8)$$

The relation between J_T and J_c along the z direction can be written as,

$$J_{T_z} = (\sin\theta\sqrt{1+\cos^2\theta})^{1/3} J_c. \quad (4.9)$$

The relation between $U_{0,T}$ and $U_{0,c}$ can be written as,

$$U_{0,T} = (\sin\theta\sqrt{1+\cos^2\theta})^{1/2} U_{0,c}. \quad (4.10)$$

Then the relation between $J_T/U_{0,T}$ and $J_c/U_{0,c}$ along the two reciprocal lattice directions

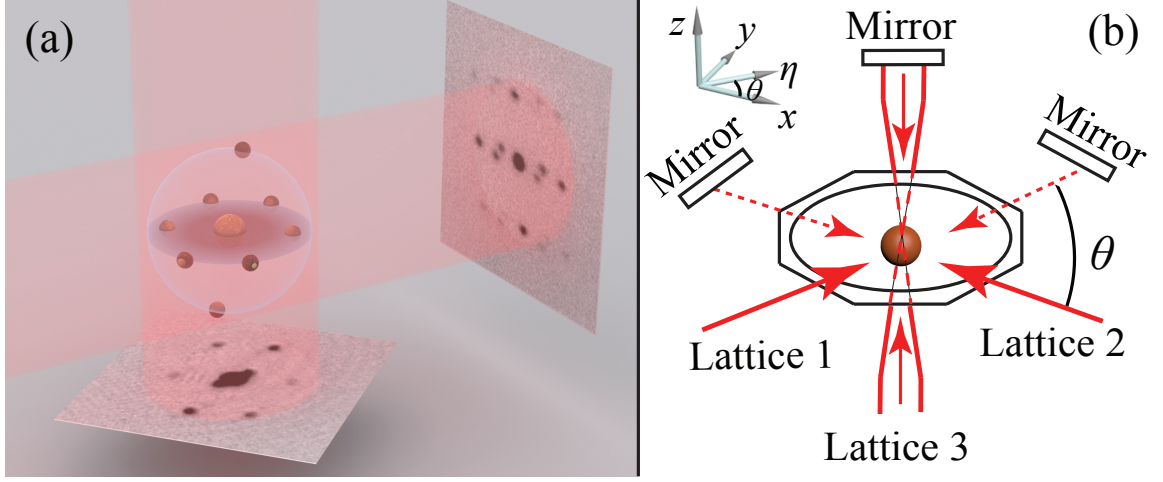


Figure 4.1: (a) Schematic of reciprocal lattice and TOF images from top and side views taken after lattices are abruptly released. The imaging beams are shown by the red area. (b) Schematic of our monoclinic lattices setup. We set $\theta = \pi/4$.

is shown below:

$$\frac{J_{T_x}}{U_{0,T}} = \frac{J_{T_\eta}}{U_{0,T}} = \frac{\exp[-\frac{1}{4}(\frac{1}{\sin \theta} - 1)(\frac{a_c}{\beta_c})^2]}{(\sin \theta)^{7/6}(1 + \cos^2 \theta)^{1/12}} \frac{J_c}{U_{0,c}}, \quad (4.11)$$

The relation between $J_T/U_{0,T}$ and $J_c/U_{0,c}$ along z direction is shown below:

$$\frac{J_{T_z}}{U_{0,T}} = (\sin \theta \sqrt{1 + \cos^2 \theta})^{-1/6} \frac{J_c}{U_{0,c}}. \quad (4.12)$$

The ratio J/U_0 is the arithmetic mean of the three directions x, η, z .

4.2 Superfluid to Mott-insulator phase transition in monoclinic lattices

Similar to our previous work, a $F = 1$ BEC of 1.2×10^5 atoms is obtained by an optical cooling process and fully polarized to the $|F = 1, m = -1\rangle$ state by an applied weak magnetic field gradient. Then an rf-pulse resonant with a fixed magnetic field is imposed to create a spinor BEC with zero magnetization (16). By holding the spinor BEC for several

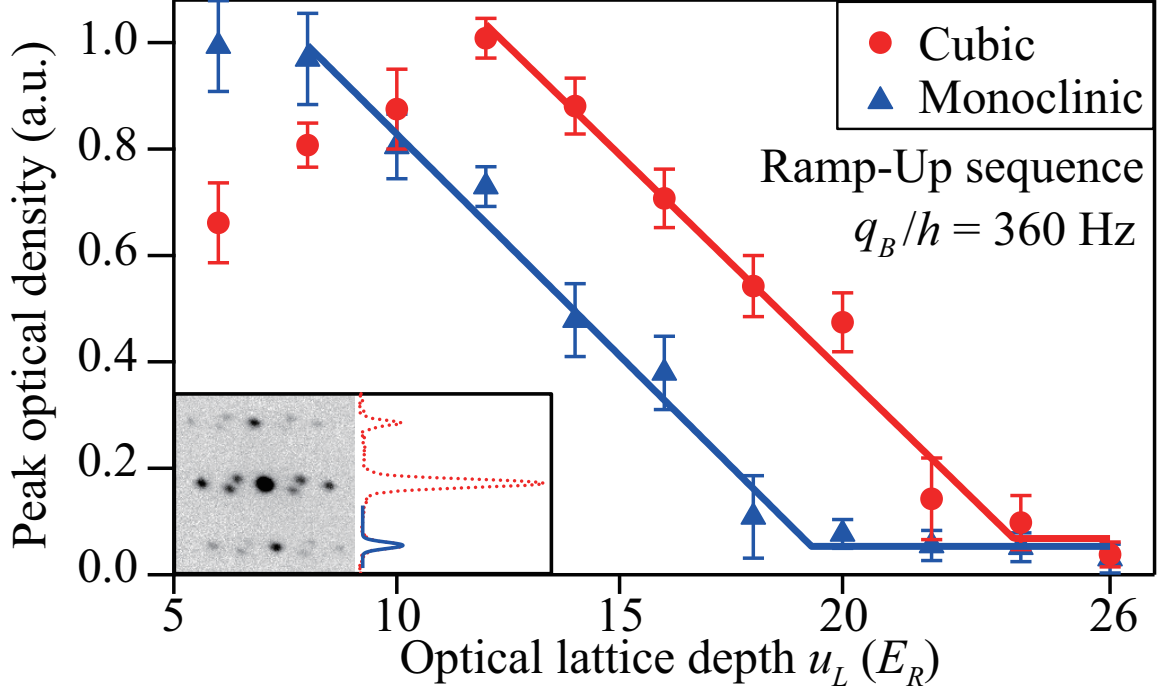


Figure 4.2: Peak optical density of interference peaks versus u_L after our cubic and monoclinic lattices ramp-up sequences. Experimental data are shown by different makers, and lines are two linear fits to the data. Here cubic lattices data are copied from our paper (44). Inset: It shows how we extract the peak optical density from a TOF image. The blue solid line is a gaussian fit to the side peak. Here the magnetic field is set at $q_B/h = 360$ Hz.

seconds we can get the initial longitudinal polar (LP) ground state (42). After quenching q_B to a desired value, the spinor BEC is adiabatically loaded into a cubic or a monoclinic optical lattice with the lattice trap depth u_L being raised at a rate of $2E_R/\text{ms}$.

A 1064 nm single-mode laser is used to construct both our 3D cubic optical lattices and monoclinic lattices. For our monoclinic lattices, θ is $\pi/4$ and the setup is shown in Fig. 4.1. In Fig. 4.1(a), the six first-order and two second order diffracted peaks can be clearly seen in the time-of-flight (TOF) images both from the side view and top view.

First we study the SF-MI transition points in both monoclinic and cubic lattices. A LP state BEC is created at large q_B and loaded into a 3D lattice with the lattice depth being ramped up. Here we choose $q_B/h = 360\text{Hz}$ so the transition is second order and the transition points for ramp-up and ramp-down sequences are the same. Hence we can only focus on the ramp-up sequence. Fig. 4.2 shows the peak optical density of interference peaks

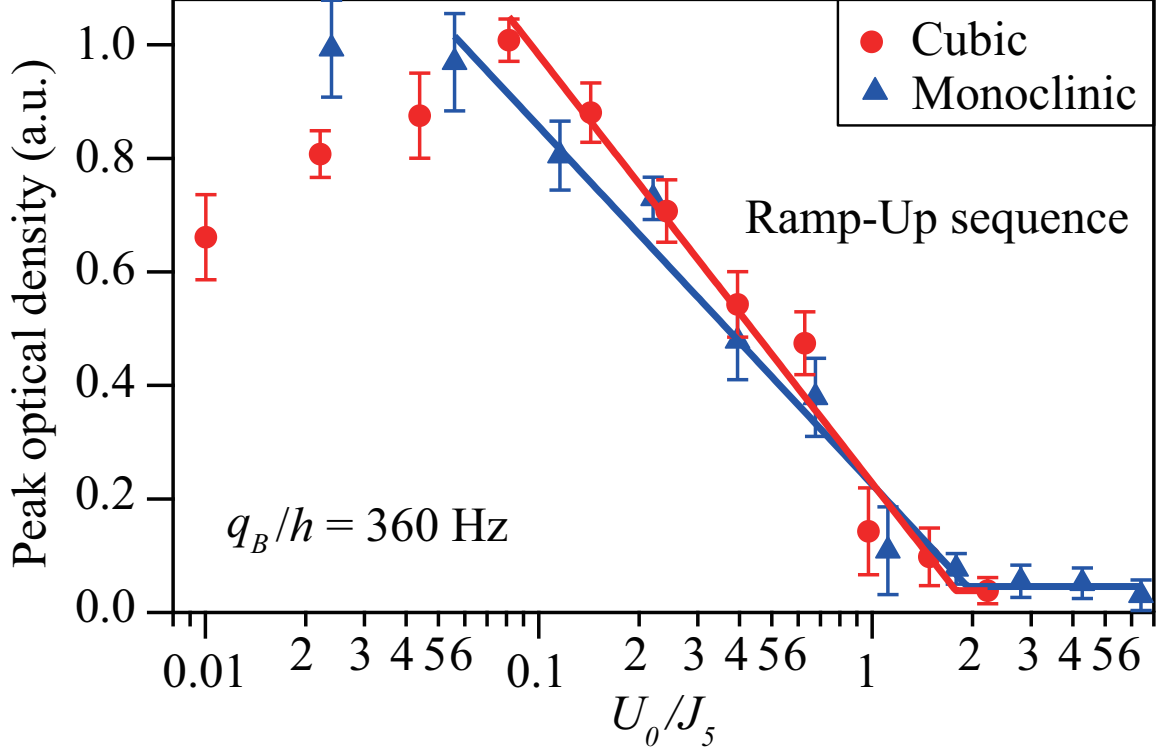


Figure 4.3: Peak optical density of interference peaks taken in our monoclinic and cubic lattice experiments versus J_5/U_0 . Solid lines are exponential fits to the experimental data. Here the magnetic field is set at $q_B/h = 360$ Hz.

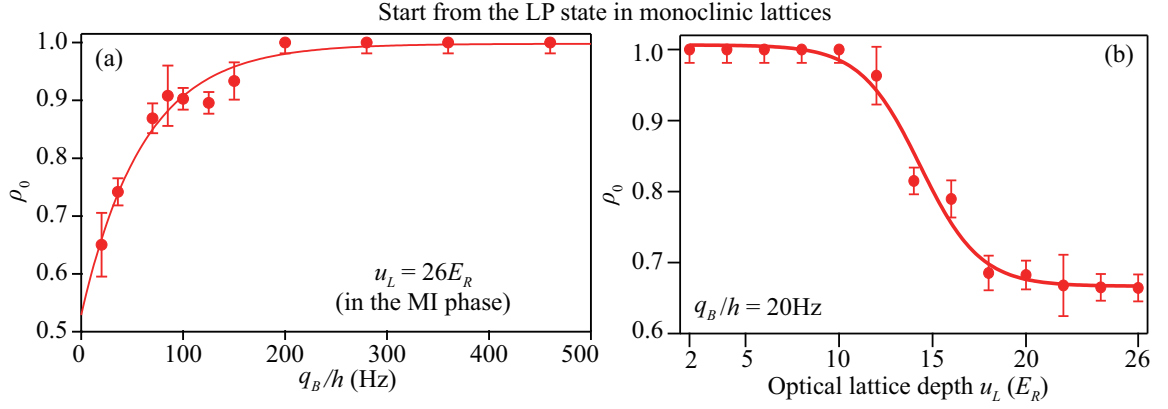


Figure 4.4: (a) We measured ρ_0 at various q_B in monoclinic lattices. In order to ensure all atoms enter into the MI phase, we set the final u_L at $26E_R$. (b) Similar to Panel (a) but we set $q_B/h = 20$ Hz. Solid lines in Panels (a) and (b) are exponential and sigmoidal fits, respectively.

versus u_L for BECs in both monoclinic and cubic lattices. The transition points are drafted for both monoclinic lattice ($\sim 20E_R$) and cubic lattice ($\sim 24E_R$). Clearly the transition in our monoclinic lattice happens much earlier than that in cubic lattices. Comparing with the

cubic lattices, the volume of each site in the monoclinic lattices is increased and the lattice trap frequency in the same trap depth is lowered. The distance between the nearest neighbor sites is enlarged. Therefore, both J and U_0 are reduced. So the value of J/U_0 is changed and the transition point is shifted. Quantitatively, we define $J_n = v(2n+1+2\sqrt{n(n+1)})J$, v is the number of nearest neighbor sites (67). For our 3D cubic and monoclinic lattices, $v = 6$. n is the occupation number per lattice site. n is around five for our cubic and monoclinic lattices. By using Eq. (4.11), we get the values of U_0/J_5 at different trap depths both for our monoclinic and cubic lattices, and the relationship between U_0/J_5 and peak optical density. The results are shown in Fig. 4.3 where data for two different lattice geometries coincide, and the transitions happen at nearly the same U_0/J_5 . The result indicates our model works well in our monoclinic lattices.

We then compare spinor BECs in our cubic and monoclinic lattices within a wide range of magnetic fields, $20 \text{ Hz} \leq q_B/h \leq 500 \text{ Hz}$, after identical lattice ramp sequences are applied. Similar to what happens in cubic lattices (44), in our monoclinic lattices, a state including all three m components forms during the evolving process starting from the initial LP ground state as u_L is ramped up at low magnetic field (Fig. 4.4(b)). We may attribute it to the formation of spin singlets in the even Mott lobe. In addition, Fig. 4.4(a) shows, in the MI phase ($26E_R$), ρ_0 increases with q_B . And its value is almost one at $q_B/h \geq 150 \text{ Hz} > U_2$ where the ground state phase diagram of antiferromagnetic spinor BECs resembles that of the scalar BECs with only second-order SF-MI transitions. Then by considering $U_2 \simeq 0.04U_0$ and the peak filling factor n being five, we can get the value of q_B/U_2 as shown in Fig. 4.5(b). The results of the two lattice geometries coincide with the mean-field predictions (44).

4.3 Differences induced by the purification of initial states

There are two types of polar states in spinor BECs at zero magnetization m : the longitudinal polar (LP) state with $\rho_0 = 1$, and the transverse polar (TP) state with $\rho_0 = 0$. At zero q_B , TP and LP states are degenerate in energy, which can be seen in Eq. (1.5). At $q_B > 0$

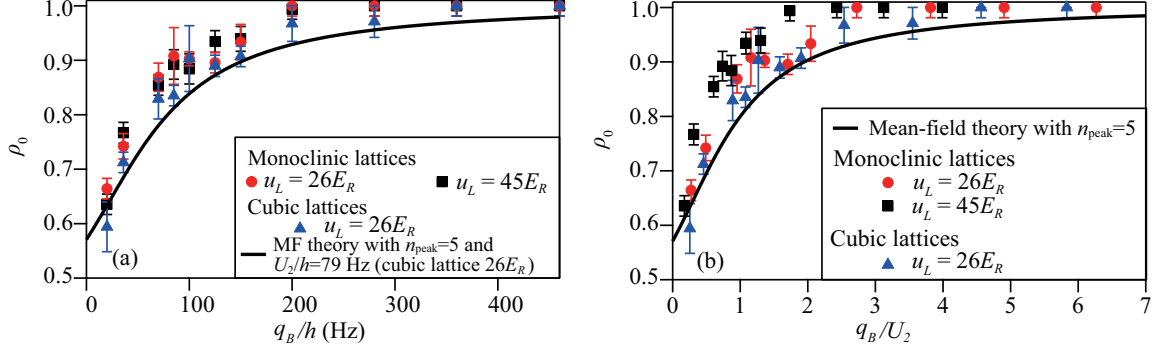


Figure 4.5: (a) Measured ρ_0 versus q_B/h (b) Measured ρ_0 versus q_B/U_2 and the final u_L at $26E_R$ and $45E_R$ in monoclinic lattices, and at $26E_R$ in cubic lattices. Solid lines are the MF results at various occupation number n . Here the maximum of n is five.

and $m = 0$, the ground state is always the LP state, while the meta-stable TP state also exists (15, 42). The preparation methods for LP and TP states were explained in Chapter-3.

As explained in the previous sections and chapters, the ratio q_B/U_2 is a key factor to understand spinor BECs under external magnetic fields in 3D optical lattices. At high magnetic fields where $q_B \gg U_2$, the three spin components in $F = 1$ spinor BECs are well separated away from each other. In other words, the spin-dependent interaction is negligible, and spinor BECs and scalar BECs behave similarly at $q_B \gg U_2$. In the opposite limit, U_2 is dominant at low magnetic fields. In antiferromagnetic spinor BECs, U_2 penalizes high-spin configurations as spin-singlet pairs are formed to minimize the energy, which leads to the enlarged Mott lobes at even occupation numbers n . Thus, superfluid to Mott-insulator phase transitions in antiferromagnetic spinor BECs can be first order and second order, although there are only second-order SF-MI phase transitions in scalar BECs and ferromagnetic BECs (44). In the second-order SF-MI phase transitions, we find that the lattice ramp-up and ramp-down sequences are symmetrical and have an almost identical phase transition point. On the other hand, in the first-order SF-MI phase transitions, we observe hysterical effect, substantial changes in the $m_F = 0$ spin component, and substantial heatings as atoms cross the SF-MI phase transitions in both monoclinic and cubic optical lattices (44).

Figure 4.6 shows that atoms stay in the LP state after the lattice is adiabatically ramped

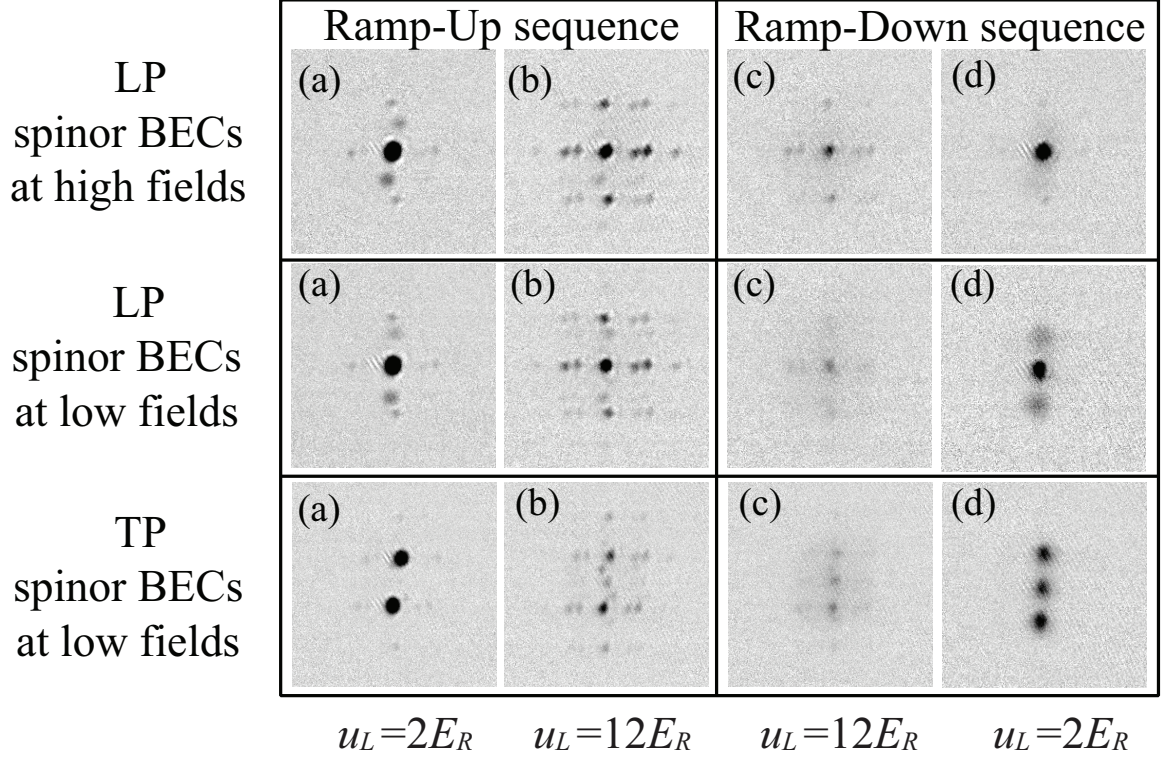


Figure 4.6: Interference patterns observed after we abruptly release TP and LP spinor BECs at $q_B/h = 360$ Hz (a high magnetic field) and $q_B/h = 20$ Hz (a low magnetic field) at various u_L and a 4.5-ms Stern-Gerlach separation during a 5.5-ms TOF. Panels (a)-(b) are taken after ramp-up sequences to a final $u_L = 2E_R$ and $12E_R$. Panels (c)-(d) are taken after first ramping up the lattice to $26E_R$ and then ramping the lattice down to a final u_L of $12E_R$ and $2E_R$. The lattice ramp speed is $2E_R$ per one millisecond.

up and down at high magnetic fields (e.g. $q_B/h = 360$ Hz). This indicates that the SF-MI phase transition is second order at sufficiently high magnetic fields (44). In contrast, at low magnetic fields (e.g. $q_B/h = 20$ Hz), we find that atoms evolve from the LP state to a state consisting of all three spin components (i.e., substantial fractions of the $m_F = \pm 1$ components). This observation can be understood by the formation of spin singlets (where $\rho_0 = 1/3$) in the even Mott lobe, and can be regarded as a trustworthy signature for the first-order SF-MI phase transitions. We also observed the similar changes in ρ_0 in the cubic lattices and have discussed it in the previous chapter (44).

The TP state is more complicated, since it is not the ground state at $q_B > 0$. In other words, spin population oscillations and energy dissipations cannot be ignored, and thus atoms cannot stay in the TP state at both high and low magnetic fields. As shown in

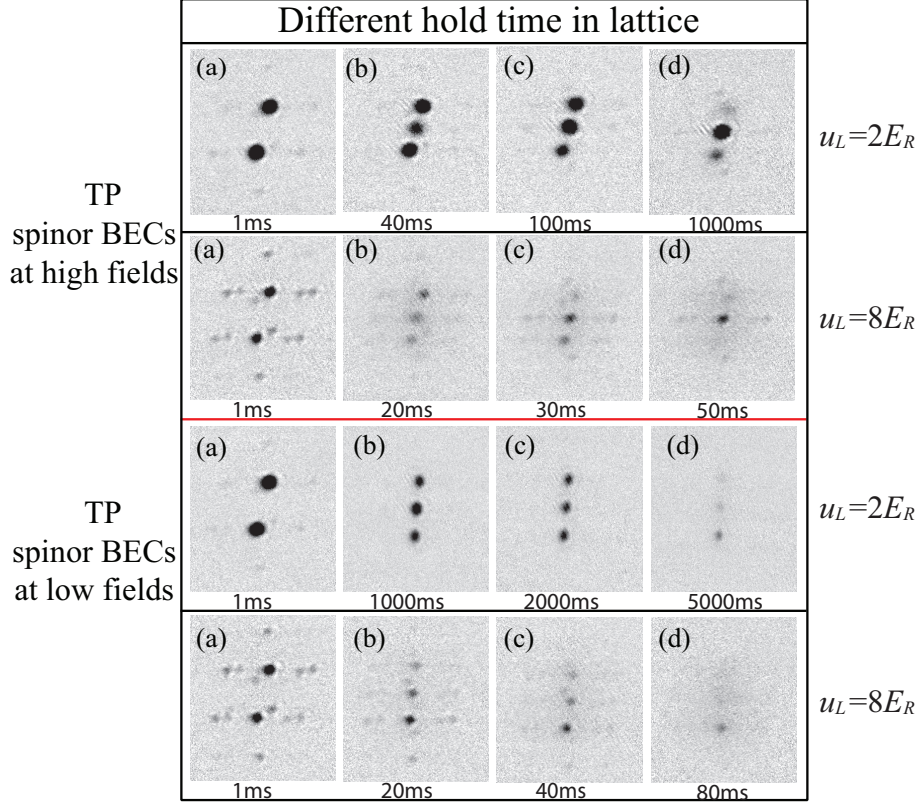


Figure 4.7: Absorption images taken after linearly ramping up the lattice to a final u_L ($2E_R$ or $8E_R$), holding TP states at the final u_L for various time, abruptly releasing atoms from the lattices, and a 5.5-ms TOF (including a 4.5-ms Stern-Gerlach separation) at $q_B/h = 360$ Hz and 20 Hz.

our recent publication (42), the speed of energy dissipations in spinor BECs increases with q_B , i.e., the strength of external magnetic fields. To understand the time evolution of the lattice-trapped TP state well, we ramp up lattices and monitor atoms after holding them in lattices for various amounts of time. As shown in Fig. 4.7, the energy dissipation in the TP states is found to be very slow (in the order of a few seconds) at low magnetic fields, and becomes much faster (in the order of tens of ms) at high magnetic fields. Note that the typical time period of the lattice ramp-up and ramp-down sequences in this report is shorter than 30 ms. Therefore, at low magnetic fields, energy dissipations can be ignored and only the coherent spin population oscillations are considered. In the opposite limit, at high magnetic fields, energy dissipation is the dominant mechanism and spin population oscillations are completely suppressed. It is well known that extra heatings can be generated by energy dissipations rather than a coherent spin population oscillation. At low magnetic

fields, it is thus expected that interference patterns observed in TP spinor BECs after lattices are ramped up and down should be as sharp as those in the LP states. This is well confirmed by our data shown in Fig. 4.6. Two more useful conclusions can be obtained from Fig. 4.6. First, due to coherent spin population oscillations, atoms cannot stay in the TP states after lattice ramp-up and ramp-down sequences, i.e., we observe substantial fractions of the $m_F = 0$ component after the ramp sequences. Second, similar to the LP state at low magnetic fields, extra heatings are observed after the lattice ramp-down sequences (after atoms crosses the SF-MI phase transitions twice) in the TP state at low magnetic fields. As explained in the previous sections, this is a convincing signature for the first-order SF-MI phase transitions.

CHAPTER V

LATTICE-INDUCED RAPID FORMATION OF SPIN SINGLETS IN SPIN-1 SPINOR CONDENSATES

This chapter discusses our efficient experimental scheme to rapidly create spin-singlet states with lattice-confined antiferromagnetic spinor condensates. One paper related to these topics was published:

- L. Zhao, T. Tang, Z. Chen, and Y. Liu, *Lattice-induced rapid formation of spin singlets in spin-1 spinor condensates*, arXiv:1801.00773. Included in Appendix C.

5.1 Create spin singlet states in free space or with optical lattices

In Chapter III, we discuss the ground states at various q_B in spinor BECs in three-dimensional cubic lattices. At $q_B = 0$, the ground state is a spin-singlet state. Many-body spin singlet states, in which multiple spin components of zero total spin are naturally entangled, have been widely suggested as ideal candidates in investigating quantum metrology and quantum memories (68, 69, 70, 71, 72, 73, 74, 75, 76, 77, 78, 79, 80, 81). Advantages of spin singlets in the quantum information research include long lifetimes and enhanced tolerance to environmental noises (69, 70). These advantages may become more pronounced if the singlets consist of ultracold spin-1 particles (68). A spin singlet is the ground state of many types of spinor gases, however, its experimental realizations have proven to be very

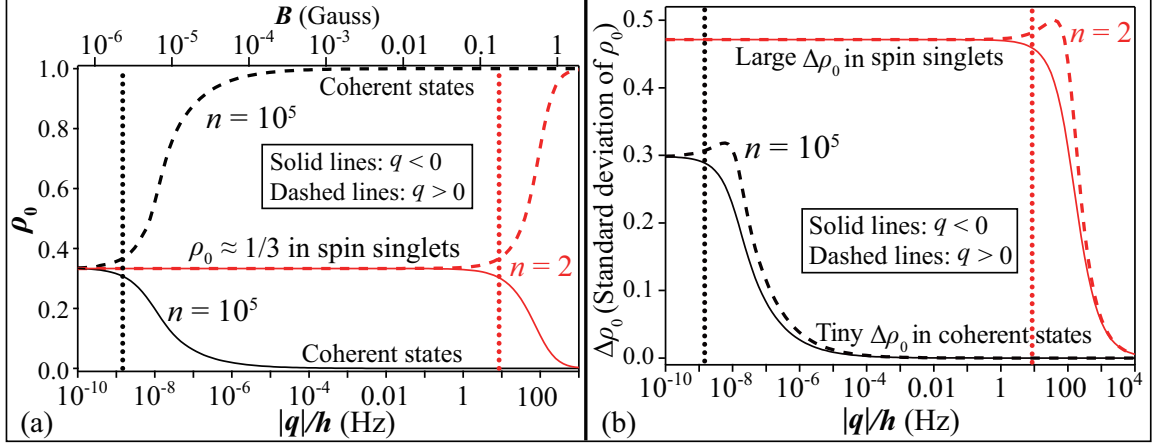


Figure 5.1: (a) and (b): vertical black (red) dotted lines mark q_{\max} , the maximum allowed q for spin singlets, in $F=1$ sodium spinor BECs of $n = 10^5$ atoms in free space (in the $n=2$ Mott lobe at $u_L = 26E_R$). All panels are derived from MFT at zero m with solid (dashed) lines representing the $q < 0$ ($q > 0$) region, and black (red) lines representing spinor gases in free space (spinor Mott insulators). (a) Predicted ρ_0 versus $|q|$ at $n = 2$ (red) and 10^5 (black). The top horizontal axis lists the corresponding B when $q > 0$. (b) Predicted $\Delta\rho_0$ versus $|q|$ at $n = 2$ (red) and 10^5 (black).

challenging mainly due to its fragilities (70, 77, 79, 80, 81, 82). Allowed parameter ranges for spin singlets of spin-1 atoms are strictly limited to the vicinity of zero quadratic Zeeman energy q and zero magnetization m , and the ranges drastically shrink when the atom number increases (77, 78, 79, 80). Another constraint is the formation of spin singlets requires atoms remaining adiabatic for a long time duration (80). Here we experimentally demonstrate that combining a spinor Bose-Einstein condensate (BEC) with cubic optical lattices significantly relaxes these strict constraints and enables creating spin singlets of spin-1 atoms rapidly. Our observations confirm that spin singlets are brought into experimentally accessible regions by two key lattice-modified parameters, which are the lattice-enhanced interatomic interactions and substantially reduced atom number in individual lattice sites. Lattice-confined spinor BECs present degeneracies in spin and spatial domains, which provide perfect platforms to simulate quantum mesoscopic systems and study rich physics of fragmentation (74, 79).

We start each experimental cycle with an antiferromagnetic $F=1$ spinor BEC of $n = 1.2 \times 10^5$ sodium atoms and zero m in its free-space ground state, i.e., a longitudinal polar (LP) state in the $q > 0$ region or a transverse polar (TP) state when $q < 0$ (15, 30, 39, 42, 44, 62).

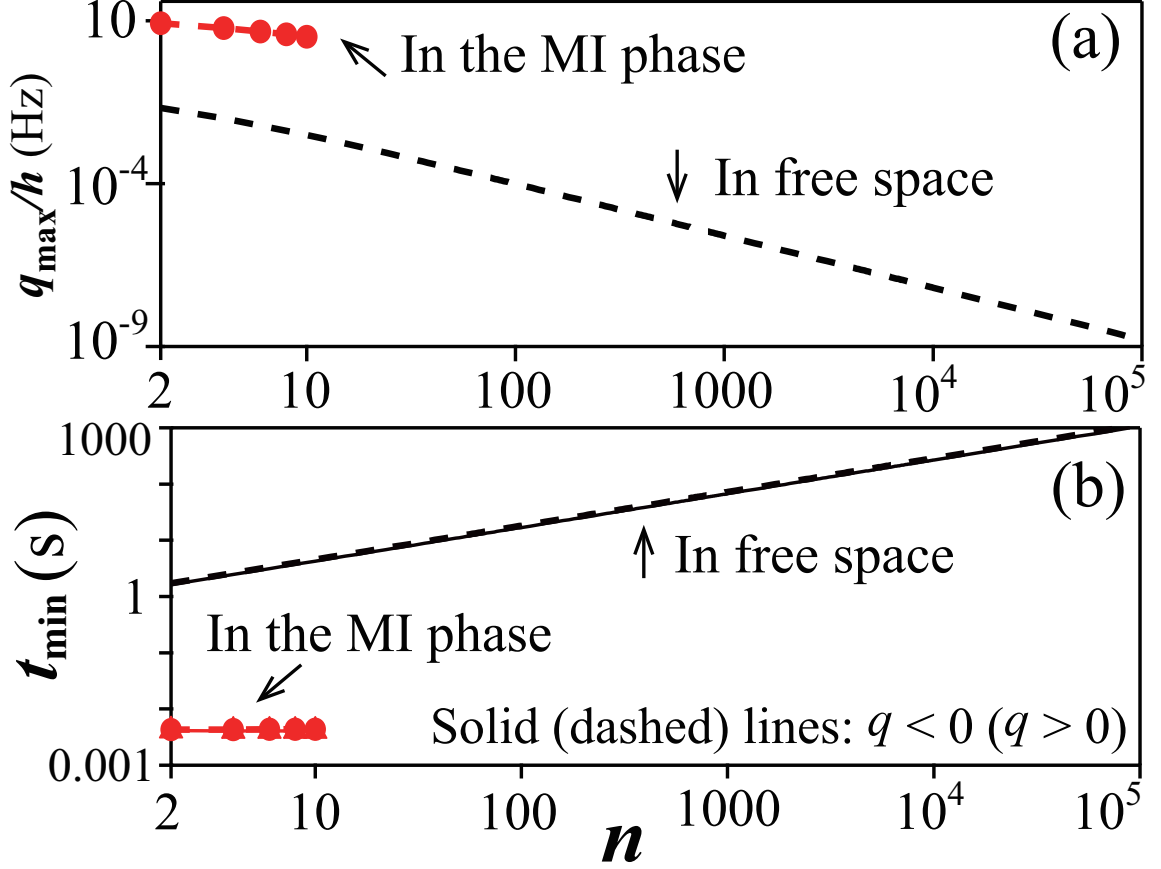


Figure 5.2: (a) Predicted q_{\max} versus n . (b) The minimum time t_{\min} versus n for generating singlets of sodium atoms via an adiabatic sweep at its corresponding $\pm q_{\max}$.

The atoms are then loaded into cubic lattices and enter into the MI phase with the peak occupation number per lattice site being five, $n_{\text{peak}} = 5$. We express the Hamiltonian of the spinor Mott insulators by ignoring the hopping energy in the site-independent Bose-Hubbard model as (44):

$$\hat{H} = \frac{U_0}{2}(\hat{n}^2 - \hat{n}) - \mu\hat{n} + \frac{U_2}{2}(\hat{\mathbf{S}}^2 - 2\hat{n}) + q(\hat{n}_1 + \hat{n}_{-1}) . \quad (5.1)$$

Here U_0 (U_2) is the spin-independent (spin-dependent) interaction, μ is the chemical potential, $\hat{\mathbf{S}}$ is the spin operator, and $\hat{n} = \sum_{m_F} \hat{n}_{m_F}$ is the number operator of all hyperfine m_F states. We obtain the ground states of spinor Mott insulators by diagonalizing Eq. (5.1) at a given n . For example, the ground states are spin singlets at zero q in the even Mott lobes.

Sufficiently deep cubic lattices localize atoms and lower n by five orders of magnitude in a typical BEC system. Figure 5.1 illustrates how this enormous reduction in n together with the lattice-enhanced interatomic interactions can make spin singlets realizable in experimentally accessible regions. Figure 5.1 is derived from the mean-field theory (MFT) and based on two notable signatures of a spin singlet, i.e., each of its m_F states has an identical fractional population ρ_{m_F} and a big $\Delta\rho_{m_F}$ (the standard deviation of ρ_{m_F}) (58, 77, 83). For example, spin singlets of $F=1$ atoms should have $\rho_0 \approx \rho_{\pm 1} \approx 1/3$ and $\Delta\rho_0 = 2\Delta\rho_{\pm 1} > 0.29$. In sharp contrast, $\rho_0 = 0$ and $\rho_{\pm 1} = 0.5$ ($\rho_0 = 1$ and $\rho_{\pm 1} = 0$) with negligible $\Delta\rho_{m_F}$ are found in coherent TP (LP) states when $q < 0$ ($q > 0$) (42). The allowed q range for spin singlets is $0 \leq |q| \leq q_{\max}$, which is determined by considering $\Delta\rho_{m_F} \gg 0$ and $\rho_0 = (1 + 0.1)/3$ at $q = q_{\max}$ (that corresponds to $\rho_0 \simeq (1 - 0.1)/3$ at $q = -q_{\max}$) in MFT. An expansion of ten orders of magnitude in q_{\max} is marked by vertical dotted lines in Figs. 5.1(a) and 5.1(b), i.e., from a narrow region of $|q|/h < 2 \times 10^{-9}$ Hz in a free-space spinor BEC of 10^5 atoms to a much broader range of $|q|/h < 9$ Hz in $n=2$ spinor Mott insulators. Here h is the Planck constant. This drastic raise in q_{\max} as n decreases is also shown in Fig. 5.2(a) for a wide range of achievable n . In addition, the lattice-induced big reduction in n can relax the magnetization constraint on creating spin singlets by five orders of magnitude, because $|m| \lesssim 0.15/n$ is required for singlets at zero q . Figure 5.2(b) indicates another big improvement made by cubic lattices: t_{\min} can be dramatically decreased by three orders of magnitude after a free-space spinor BEC enters the MI phase. Here t_{\min} is the minimum time for generating singlets via adiabatically sweeping one parameter, such as q and the lattice depth u_L . Spin singlets of $F=1$ atoms can thus be created in realistic experimental setups, e.g., in the spinor Mott insulators of $|m| \leq 0.05$ as confirmed by our experimental data in Figs. 5.5 and 5.6.

Similar to Ref. (77), we diagonalize the Hamiltonian in Eq. (1.30) in the $|n, F, M\rangle$ basis, and find the ground state of the spinor BEC is $|G\rangle = |n, F, M = F\rangle = (F!(n-F)!!(n+F+1)!!/(2F+1)!!)^{-1/2} a_1^{\dagger F} (S^\dagger)^{(n-F)/2} |\text{vac}\rangle$ at a given magnetization m and $q = 0$. Here n is the total number of atoms, F is the total atomic spin, $M = m \cdot n$ is the projection of F along the z direction, $S^\dagger = a_0^{\dagger 2} - 2a_1^\dagger a_{-1}^\dagger$ is the creation operator for a singlet pair. The

double factorial $!!$ of a number n is the product of the integers from 1 up to n that have the same parity (odd or even) as n . The fractional population of hyperfine m_F state is defined as ρ_{m_F} , and the standard deviation of ρ_{m_F} is $\Delta\rho_{m_F}$. Because $m = F/n$ and $\Delta\rho_0 = \Delta n_0/n$, both ρ_0 and $\Delta\rho_0$ are strong functions of m at $q = 0$ as:

$$\rho_0(m) = (1 - |m|)/(2|m|n + 3) ,$$

$$\Delta\rho_0(m) = \frac{\langle (a_0^\dagger a_0 - \langle a_0^\dagger a_0 \rangle)^2 \rangle^{1/2}}{n} = \frac{2}{3 + 2n|m|} \sqrt{\frac{(1 - |m|)(1 + n|m|)(3 + n + n|m|)}{(5 + 2n|m|)n}} . \quad (5.2)$$

Eq. 5.2 is simplified to $\Delta\rho_0(0) = \sqrt{4/45 + 4/(15n)}$ and $\rho_0(0) = 1/3$ at $m = 0$. The allowed region for spin singlets is $0 \leq |m| < m_{\max}$. The value of m_{\max} is determined by $\rho_0(m_{\max}) = 0.9\rho_0(0)$, which leads to $\Delta\rho_0(m_{\max}) > 0.9\Delta\rho_0(0)$. Figure 5.3 shows how the magnetization constraint on the formation of spin singlets changes with n .

In each experimental cycle, we prepare a LP or TP state at $q/h = 40$ Hz by pumping all atoms in the undesired m_F states of a $F=1$ spinor BEC to the $F=2$ state with resonant microwave pulses, and blasting away these $F=2$ atoms via a resonant laser pulse. We then quench q to a proper value in microwave dressing fields (16), and load atoms into a cubic

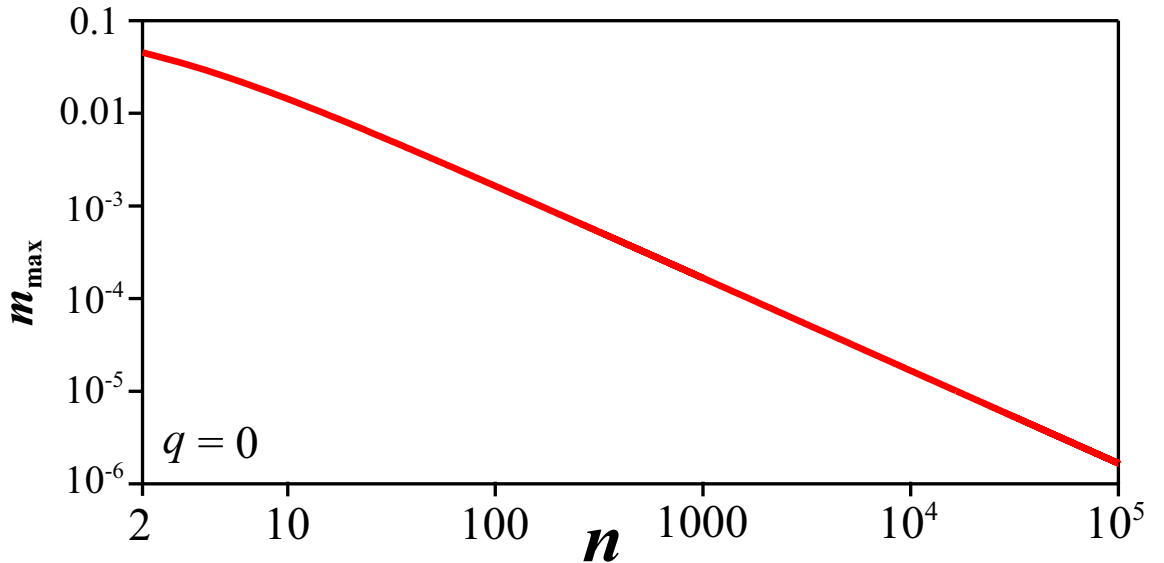


Figure 5.3: The maximum allowed m for spin singlets at $q = 0$, derived from the mean-field theory for $F=1$ sodium spinor BECs.

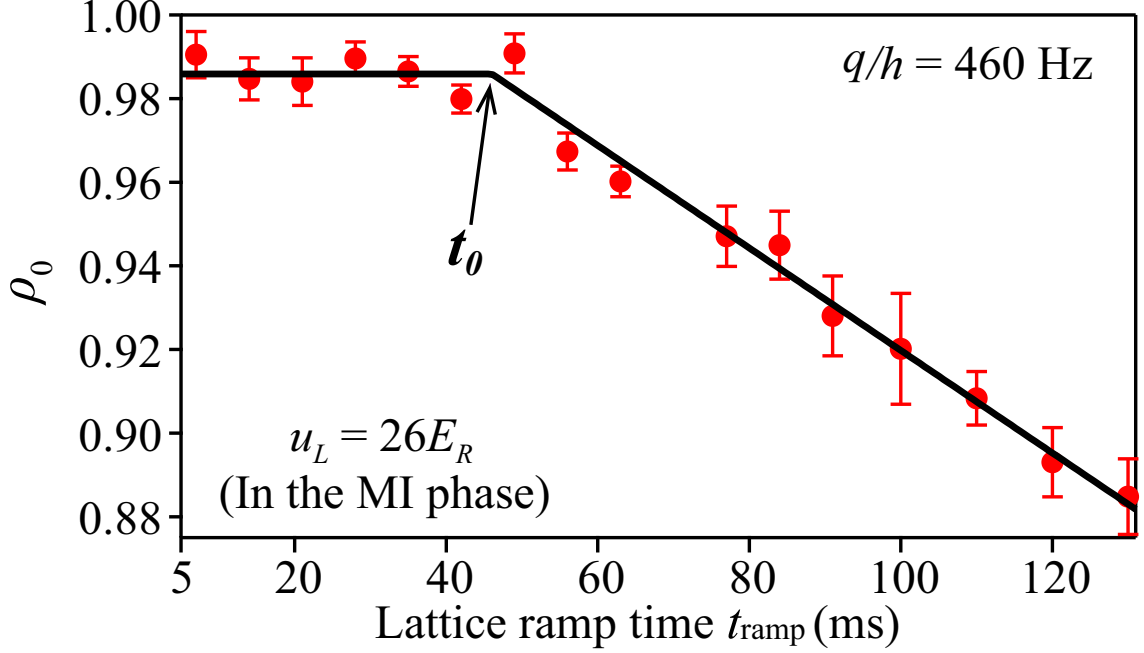


Figure 5.4: Measured ρ_0 versus t_{ramp} after an initial LP spinor BEC enters the MI phase in a high field. Black lines are two linear fits. We estimate t_0 , the ideal t_{ramp} , from the intersection point of these two lines (see text).

lattice. Each data point in this paper is collected after atoms being abruptly released from a lattice at a fixed u_L and expanding ballistically within a given time of flight t_{TOF} . The standard Stern-Gerlach absorption imaging is a good method to measure ρ_{m_F} of spinor gases in the SF phase. Stern-Gerlach separations become indiscernible, when atoms completely lose phase coherence in the MI phase and the signal-to-noise ratio diminishes in TOF images. To measure ρ_0 in spinor Mott insulators, we develop a two-step microwave imaging method as follows: 1) count the $m_F=0$ atoms with the first imaging pulse preceded by transferring all atoms in the $|F=1, m_F=0\rangle$ state to the $F=2$ state; 2) count all remaining atoms that are in the $m_F = \pm 1$ states with the second imaging pulse. We compare these two imaging methods using a free-space spinor BEC, and find they give similar ρ_0 with a negligible difference (unless specified, all quoted uncertainties are 2 standard errors).

To ensure atoms adiabatically enter the MI phase, a cubic lattice is linearly ramped up within time t_{ramp} to $u_L = 26E_R$. Here E_R is the recoil energy (30). We carefully select t_{ramp} based on three criteria. First, t_{ramp} should be long enough to satisfy $du_L/dt \ll 32\pi E_R^2/h$,

the interband adiabaticity requirement (49). Second, t_{ramp} should be larger than the MFT predicted t_{min} , as explained in Figure 5.2(b). These two criteria set $t_{\text{ramp}} > 5$ ms for our system. On the other hand, t_{ramp} should be sufficiently short, with $t_{\text{ramp}} \leq t_0$ to ensure lattice-induced heating is negligible and atom losses are not greater than 10%. Figure 5.4 explains how we determine t_0 from the observed relationship between t_{ramp} and ρ_0 in spinor Mott insulators at $u_L = 26E_R$ and $q/h = 460$ Hz. In such a high field, SF-MI phase transitions are second order because $U_2 = 0.04U_0 > 0$ and $q \gg U_2$ at this u_L for the sodium atoms (44). Atoms initially in a LP state should thus stay in the LP state with $\rho_0 \simeq 1$, as they adiabatically cross the phase transitions and enter into the MI phase (44). The value of ρ_0 quickly drops when inevitable heating is induced by lattices in a non-adiabatic lattice ramp sequence. We extract t_0 from the intersection point of two linear fits to the data in Fig. 5.4, which yields $t_{\text{ramp}} \leq t_0 \approx 45$ ms. Within this acceptable t_{ramp} range, a slower lattice ramp is preferred because it could more easily keep the system adiabatic. The ideal lattice ramp speed is therefore set at $du_L/dt = 26E_R/t_0$ for our system.

5.2 Experimental signatures of spin-singlet states

Different methods have been proposed for detecting spin singlets. The first approach is to measure the population of each spin component, as atoms in a spin singlet should be evenly distributed into all spin states (58, 83). The second method is to verify a spin singlet is invariant after its spin is rotated by a resonant Rf-pulse (69, 76, 79, 83, 84). Another signature of a spin singlet is its high level of spin squeezing shown in quantum non-demolition measurements (69, 71, 72, 73). A spin singlet can also be identified by its high-order correlation functions, e.g., its zero spin nematicity detected by light scattering measurements (79, 85). Other detectable parameters of a spin singlet include large population fluctuations in each of its spin components, and its excitation spectra mapped by Bragg scattering (58, 77). In this section, we apply the first two methods to demonstrate that most of spin-1 atoms in a lattice-confined spinor BEC can form spin singlets, immediately after the atoms cross first-order superfluid (SF) to Mott-insulator (MI) phase transitions in a microwave dressing

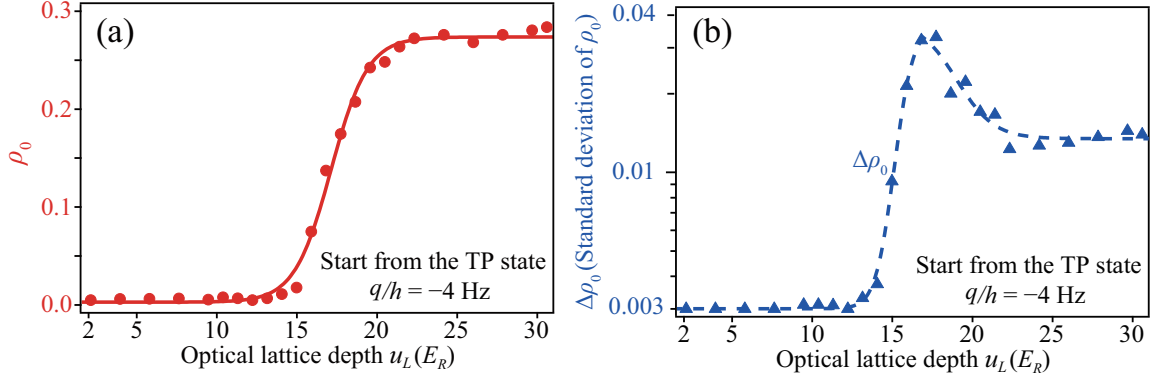


Figure 5.5: (a) Measured ρ_0 (red circles) and (b) $\Delta\rho_0$ (blue triangles) versus u_L after an initial TP spinor BEC undergoes the ideal lattice sequence to various final u_L in a weak field near zero q . The solid line is a sigmoidal fit, and the dashed line is to guide the eye.

field.

The opposite limit is $|q| \ll U_2$ near zero q , where SF-MI phase transitions are first order and spin singlets are the ground state of $F=1$ spinor gases in the even Mott lobes (44). We may thus identify the formation of spin singlets from evolutions of ρ_0 and $\Delta\rho_0$ during a first-order SF-MI transition. Figure 5.5 shows two such evolutions when atoms initially in the TP state are adiabatically loaded into the cubic lattice at the ideal lattice ramp speed to various final u_L in $q/h = -4$ Hz. These evolutions have three distinct regions. In the SF phase where $0 \leq u_L \leq 15E_R$, atoms remain in the TP state with $\rho_0 = 0$ and negligible $\Delta\rho_0$. As atoms cross first-order SF-MI transitions in $15E_R \leq u_L \leq 18E_R$, ρ_0 and $\Delta\rho_0$ sigmoidally increase with u_L . When all atoms enter into the MI phase at $u_L \geq 21E_R$, both ρ_0 and $\Delta\rho_0$ reach their equilibrium values of $\rho_0 \approx 0.3$ and $\Delta\rho_0 \gg 0$. These observations qualitatively agree with the characteristics of spin singlets. Despite that other factors can also increase $\Delta\rho_0$ in the MI phase, the measured $\Delta\rho_0$ is much smaller than the MFT prediction shown in Fig. 5.1(b). This may be due to the fact that the observed $\Delta\rho_0$ is an average over all 5×10^4 lattice sites in our system. Unless one can detect single lattice site precisely, the value of $\Delta\rho_0$ may not be used to verify spin singlets in lattice-confined spinor gases. We also monitor the time evolution of atoms at fixed u_L and q after the ideal lattice ramp sequence. No spin oscillations are found at each q studied in this paper, which confirms atoms always stay at their ground states in these ideal lattice sequences.

Another way to detect the spin singlet state is by measuring the spin state after rotating the spin of the atoms by $\pi/2$. In the free space, the atoms with total number n are in the coherent state. Take the TP state as an example, the ground state can be expressed as $\psi = \sum_{j=0}^{[n/2]} C_j (e^{i\varphi_j} |j, 0, n-j\rangle + e^{i\varphi_{n-j}} |n-j, 0, j\rangle)$. Here, we use the numbers of different spin components as basis, i.e., $|n_1, n_0, n_{-1}\rangle$ where n_k is the number of spin k atoms. As a typical TP state at $n = 2$: $\psi_{n=2} = \frac{1}{2}|0, 0, 2\rangle + \frac{1}{\sqrt{2}}e^{i\varphi_1}|1, 0, 1\rangle + \frac{1}{2}e^{i\varphi_2}|2, 0, 0\rangle$. And the state after spin rotation can be derived as:

$$\begin{aligned} \hat{R}_x \psi_{n=2} = & ((1 + e^{i\varphi_2})\frac{1}{8} - e^{i\varphi_1}\frac{1}{4})|0, 0, 2\rangle \\ & + (1 - e^{i\varphi_2})\frac{i}{4}|0, 1, 1\rangle - (1 - e^{i\varphi_2})\frac{i}{4}|1, 1, 0\rangle - ((1 + e^{i\varphi_2})\frac{1}{4} - e^{i\varphi_1}\frac{1}{2})|0, 2, 0\rangle \\ & - ((1 + e^{i\varphi_2})\frac{1}{4\sqrt{2}} + e^{i\varphi_1}\frac{1}{4})|1, 0, 1\rangle + ((1 + e^{i\varphi_2})\frac{1}{8} - e^{i\varphi_1}\frac{1}{4})|2, 0, 0\rangle, \end{aligned} \quad (5.3)$$

where $\hat{R}_x = \exp(-i\frac{\pi}{2}\hat{S}_x)$ is the spin rotation operator along the x-axis and S_x is the x-component of the spin operator. The above expression shows that ρ_0 depends on φ_j and can not be a fixed value. As a numerical example, when $\varphi_j = 0$, $\hat{R}_x \psi_{n=2} = -|0, 2, 0\rangle$ (Longitudinal polar (LP) state) while when $\varphi_2 = 0$ and $\varphi_1 = \pi$, $\hat{R}_x \psi_{n=2} = \frac{1}{2}|0, 0, 2\rangle - \frac{1}{\sqrt{2}}|1, 0, 1\rangle + \frac{1}{2}|2, 0, 0\rangle$ (TP state). This result may due to the interference between states after the spin rotation.

However, the ground states of the spinor BEC in deep lattice behave differently after the spin rotation. As a simple example, for the atom filling factor $n = 2$ in each lattice site, the ground states can be express as $\psi_{\text{MI}(n=2)} = C_0 e^{i\varphi} |0, 2, 0\rangle + C_1 |1, 0, 1\rangle$, where φ is the relative phase between the states $|0, 2, 0\rangle$ and $|1, 0, 1\rangle$ (44), and C_0 and C_1 are the functions of q . Then we can derive that $\rho_0 = \frac{\langle \psi_{\text{MI}(n=2)} | \hat{R}_x^\dagger a_0^\dagger \hat{R}_x | \psi_{\text{MI}(n=2)} \rangle}{n} = (-C_1 \frac{1}{\sqrt{2}})^2 = \frac{1}{2} C_1^2$ is independent of φ . This may be understood that since only $|1, 0, 1\rangle$ state has contribution to ρ_0 after a $\pi/2$ spin rotation, φ has no contribution to the expectation value of the ρ_0 measurement.

For $n = 4$ situation, the ground state in the MI state can be written as $\psi_{\text{MI}(n=4)} = C_0 |0, 4, 0\rangle + C_1 e^{i\varphi_1} |1, 2, 1\rangle + C_2 e^{i\varphi_2} |2, 0, 2\rangle$. After the spin rotation, ρ_0 can be solved as $\rho_0 = \frac{1}{4} C_1^2 + \frac{1}{2} C_2^2$ for this $\pi/2$ spin rotated state, which is also independent of φ . For other n , our numerical calculations through Mathematica show the same conclusion.

As we shown above, for the ground states in free space like the TP state, the outcome after spin rotation is randomized and highly dependent on the initial relative phase. In contrast, in the optical lattices, the ground state can be a state with a predictable ρ_0 after a $\pi/2$ spin rotation.

We observe similar ρ_0 and $\Delta\rho_0$ evolutions within a wide range of q near zero field. The measured ρ_0 versus q in spinor Mott insulators at $u_L = 26E_R$ is shown in Fig. 5.6. These Mott insulators of $n_{\text{peak}} = 5$ are inhomogeneous systems, in which ρ_0 at a fixed q may be given by the weighted average over all Mott lobes:

$$\rho_0 = \sum_{j=1}^5 \rho_{0j} \chi_j . \quad (5.4)$$

Here ρ_{0j} is the MFT predicted ρ_0 in the ground state ψ_j of the $n=j$ Mott lobe, and χ_j represents mean-field atom density distributions in a harmonic trap (44). The prediction of Eq. (5.4) shown by red dashed lines in Fig. 5.6, however, appears to largely disagree with our data. A resonant Rf-pulse is also applied to rotate the spin of atoms by 90 degrees. In this paper, the spin rotation operator $\hat{R}_x = \exp(-i\frac{\pi}{2}\hat{S}_x)$ is along the x -axis, which is orthogonal to the quantization axis (z -axis). After $\pi/2$ spin rotations, ρ_{0j} in Eq. (5.4) changes to $\rho_{0j}^r = \frac{\langle \psi_j | \hat{R}_x^\dagger \hat{n}_0 \hat{R}_x | \psi_j \rangle}{\langle \psi_j | \hat{R}_x^\dagger \hat{n} \hat{R}_x | \psi_j \rangle}$ in the $n=j$ Mott lobe. The prediction of Eq. (5.4) after these spin rotations is shown by the upper red dashed line in Fig. 5.6. The two data sets in Fig. 5.6 respectively represent projections of the atomic spin along two orthogonal axes.

Our data taken with and without the $\pi/2$ spin rotations appear to converge to a value around $\rho_0 \approx 1/3$ as q gets closer to zero in Fig. 5.6. This indicates the spinor Mott insulators become more rotationally invariant near zero field. As the spin rotational invariance is one unique signature of spin singlets, the reduced gap between the two data sets in Fig. 5.6 implies significant amounts of atoms may form spin singlets when q approaches zero. In our system, about 10% of atoms stay in the $n=1$ Mott lobe where no spin singlet can be formed. This accounts for the observed small gap between the two data sets near zero q in Fig. 5.6, and limits the maximum f_{ss} realizable in our system to about 90%. Here f_{ss} represents the fraction of atoms forming spin singlets in spinor gases. Similar phenomena

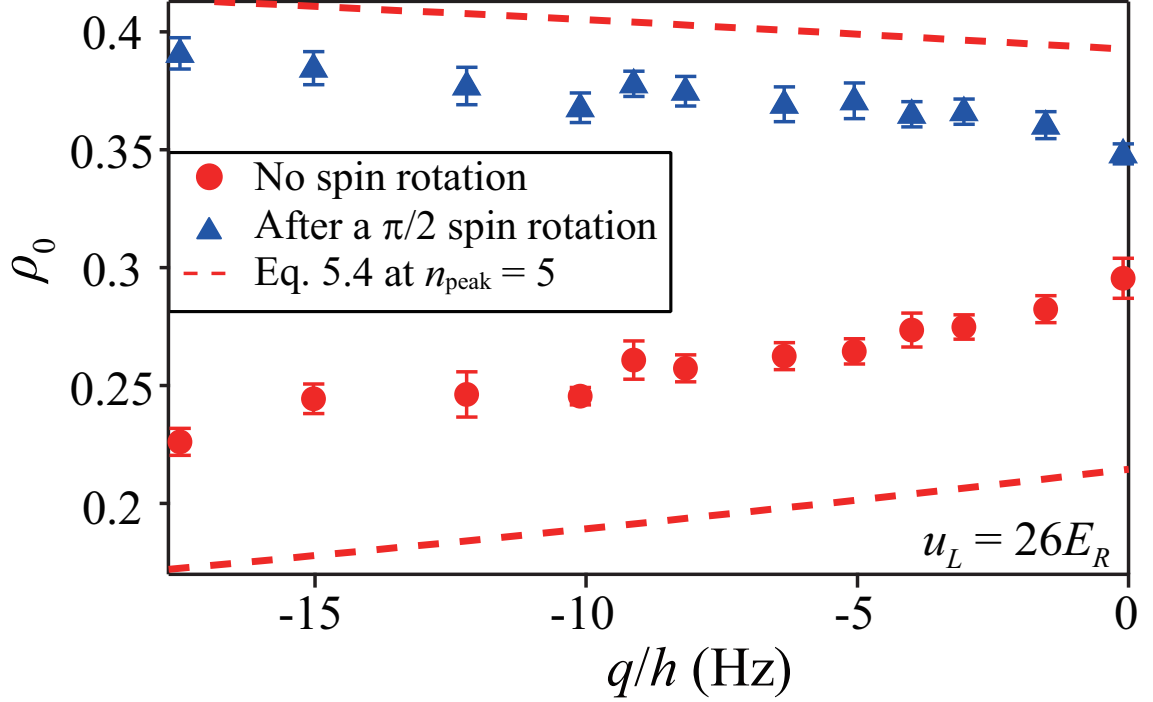


Figure 5.6: (a) Red circles (blue triangles) are the measured ρ_0 in spinor Mott insulators without (with) atoms being rotated by resonant $\pi/2$ pulses at various q . The red dashed line is the prediction of Eq. (5.4). The insulators are created after an initial TP spinor BEC undergoes the ideal lattice ramp sequence.

is also observed in spinor Mott insulators generated after atoms initially in the LP state cross first-order SF-MI transitions in the ideal lattice ramp sequences when $q > 0$.

5.3 Light-scattering measurements

In this section we discuss how to identify a spin singlet state with another detection method, i.e., using light-scattering measurements to detect optical birefringence effects and thus confirm the spin nematicity of a spin singlet state is zero (85). In the conventional Stern-Gerlach imaging method, different spin components are first separated by a magnetic field gradient and then imaged via an optical absorption process. This imaging method is destructive and can only be used to extract populations of different spin components. In contrast, the light-scattering method elaborated below is non-destructive and can detect a few different physical properties, e.g., the spin nematicity. It is therefore a very useful tool to study spin

properties of atomic systems.

The spin nematicity N is a symmetric tensor which can be expressed by the following 3×3 matrix:

$$N = \begin{pmatrix} N_{xx} & N_{xy} & N_{xz} \\ N_{yx} & N_{yy} & N_{yz} \\ N_{zx} & N_{zy} & N_{zz} \end{pmatrix} \quad (5.5)$$

In a spin singlet state, each of the nine elements of this matrix is 0. We can measure values of diagonal and off-diagonal elements by two different methods because the diagonal elements are proportional to ρ_{m_F} while the off-diagonal elements induce birefringence effects. Similar to Ref. (85), interactions between light and atoms can be described by the dielectric tensor ϵ as follows:

$$\epsilon = I + \beta_0 \langle \chi \rangle I - i\beta_1 \begin{pmatrix} 0 & S_z & -S_y \\ -S_z & 0 & S_x \\ S_y & -S_x & 0 \end{pmatrix} + \beta_2 \langle N \rangle, \quad (5.6)$$

in which I is the unit matrix, χ is the density of atoms, S_i ($i = x, y, z$) is the spin operator, and the coefficients $\beta_{0,1,2}$ are related to the linewidth Γ of the atomic transition. In this equation, the second term is related to the spontaneous emission, the third term describes the Faraday rotation, and the last term induces birefringence effects. It is important to note that the Faraday rotation and the birefringence effect can both change the polarization of the input light. In order to measure the off-diagonal elements of a nematicity matrix N , we start with a ground state in which there is no Faraday rotation. Therefore, only the off-diagonal elements of the spin nematicity matrix N can change the polarization of the input beam. One proper optical setup for the light-scattering experiment is shown in Fig. 5.7. We define $E^{(0)}$ as the electrical field of the input light. E , which is orthogonal to $E^{(0)}$, is the electrical field of the light after it passes through the BEC. The input light is red-detuned, linearly polarized, and propagates along a direction that forms an angle θ with respect to the z -axis (i.e., the direction of the applied magnetic field). After the detection light passes through the atomic gases, we record the readings of PD1 and PD2. With different optical

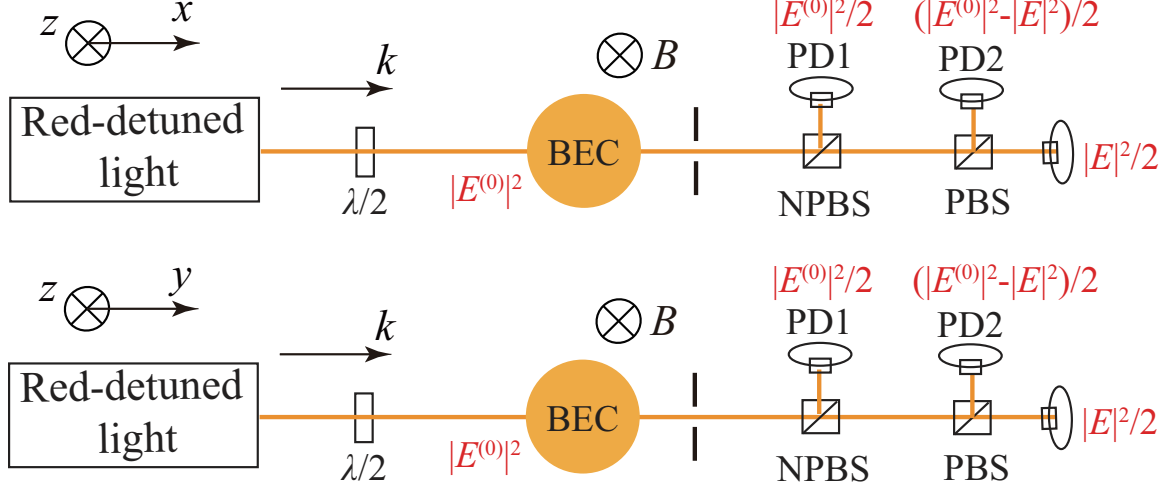


Figure 5.7: The optical setup of light-scattering measurements. Here PDs are photodetectors and PBS is a polarized beam-splitter.

setups, we can detect different off-diagonal elements. For example, we can detect N_{yz} if the input light propagates along the x -direction and the magnetic field points along the z -axis, as shown in the upper panel in Fig. 5.7. If we change the propagation direction of the input light from the x -axis to the y -axis, as shown in the lower panel in Fig. 5.7, the off-diagonal element N_{xz} can be detected. Similarly, we can measure N_{xy} if we change the magnetic field direction to the x -axis and let the input light propagate along the z -direction. Now we take the first setup shown in the upper panel in Fig. 5.7 as an example to explain how we detect the off-diagonal element N_{yz} . For this optical setup (the upper panel in Fig. 5.7), the nematicity matrix can be simplified as

$$N = \begin{pmatrix} N_{xx} & 0 & 0 \\ 0 & N_{yy} & N_{yz} \\ 0 & N_{zy} & N_{zz} \end{pmatrix} \quad (5.7)$$

And we can find N_{yz} from the relationship between E and $E^{(0)}$ as follows (85):

$$E = E^{(0)} \frac{i\omega\beta_2}{2c} \int dy (N_{yz}), \quad (5.8)$$

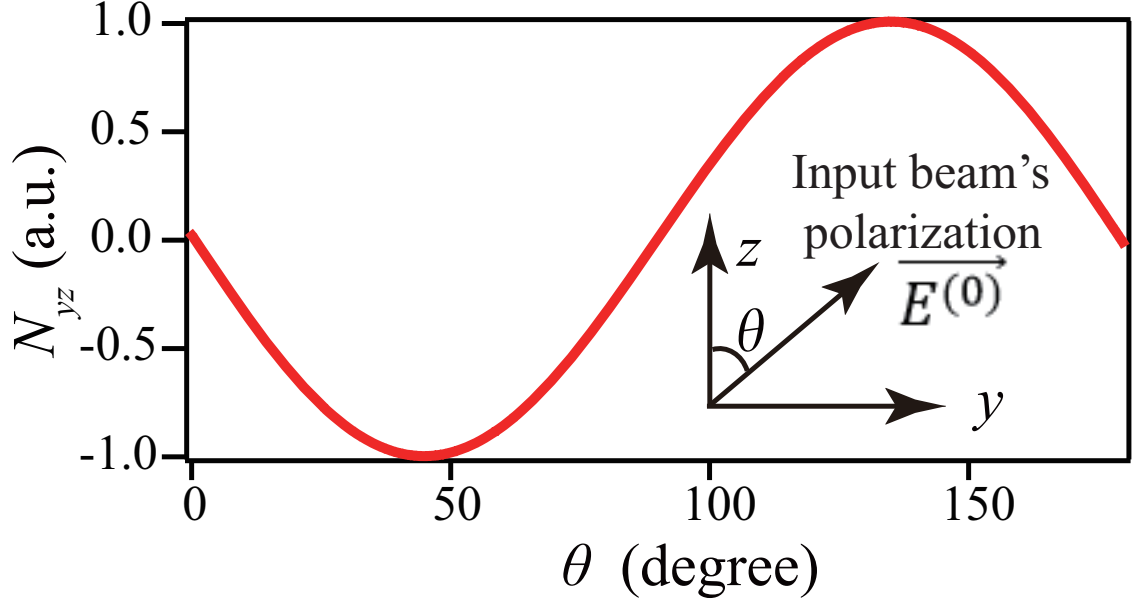


Figure 5.8: The relation between the off-diagonal element N_{yz} of the nematicity matrix and the angle θ (see text).

where c is the speed of light, and ω is the frequency of the input beam. By measuring the ratio of E to $E^{(0)}$ (obtained from the data taken by PD1 and PD2 as shown in Fig. 5.7), N_{yz} can be extracted. From a simple calculation, we can find the relationship between θ and N_{yz} , as shown in Fig. 5.8. This figure clearly shows that N_{yz} reach its maximum at $\theta = 45^\circ$.

The single spatial mode approximation is not valid in deep optical lattices, so we also need to consider spatial distributions of the nematicity matrix N for lattice-confined spinor BECs. Similar to Ref. (85), we can predict spatial distributions of the nematicity matrix N by assuming the wavefunction of atoms is $\psi(y, z) = (\exp[-(y^2 + z^2)/(2d_{ho}^2)], 1.5(y + iz), \exp[-(y^2 + z^2)/(2d_{ho}^2)])$ in the $m_F = (1, 0, -1)$ basis. Here d_{ho} is the harmonic oscillator length. In our system, $d_{ho} = 1.4\mu\text{m}$. One typical simulation result for a linearly-polarized input light is shown in Fig. 5.9.

We can calculate the ratio of E to $E^{(0)}$ within a wide range of the frequency detunings for two different ground states in our system: the longitudinal polar state (LP) and the scalar state. Here we choose the direction of the linearly polarized input light based on

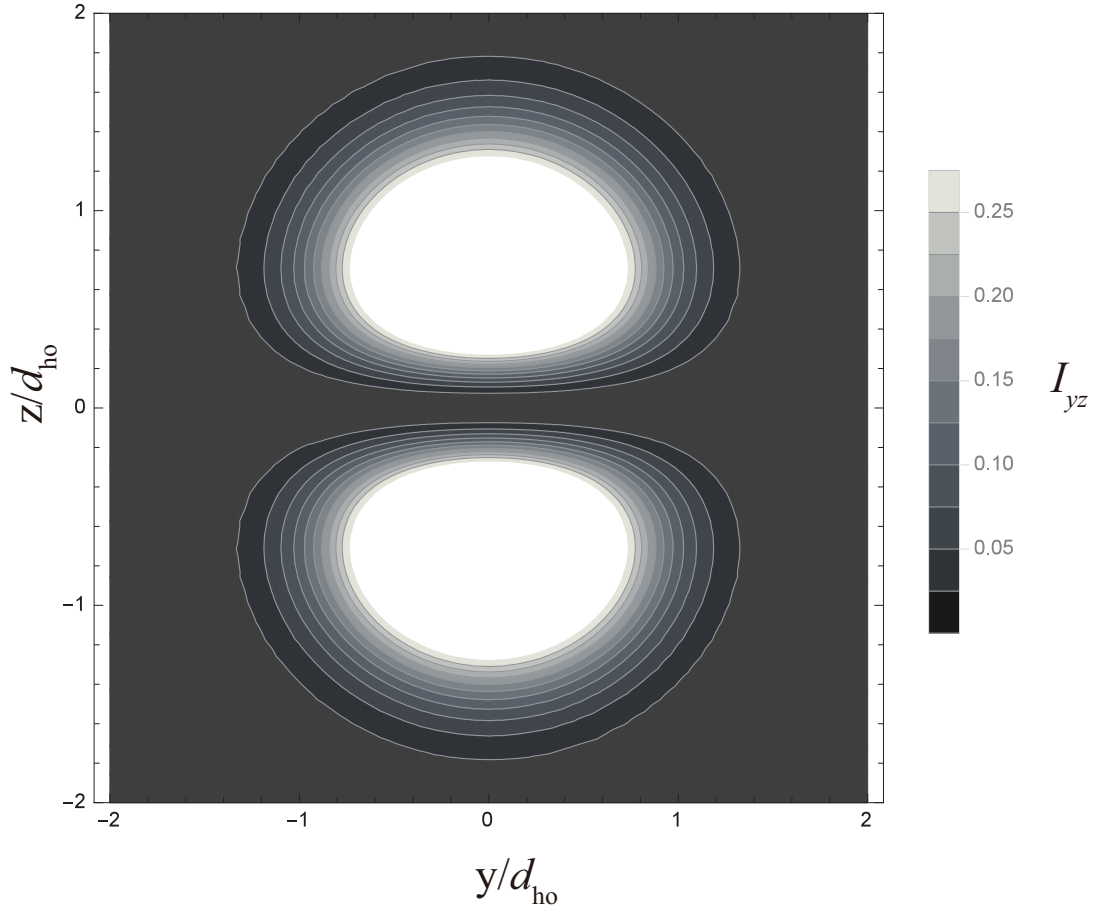


Figure 5.9: Predicted spatial distributions of I_{yz} when the light-scattering beam is linearly polarized. Here I_{yz} is proportional to $|\int \psi(y, z)^* N_{yz} \psi(y, z) dx|^2$, and can be experimentally recorded by replacing one photodetector (i.e., PD2) in Fig. 5.7 with an ultra-sensitive CCD camera.

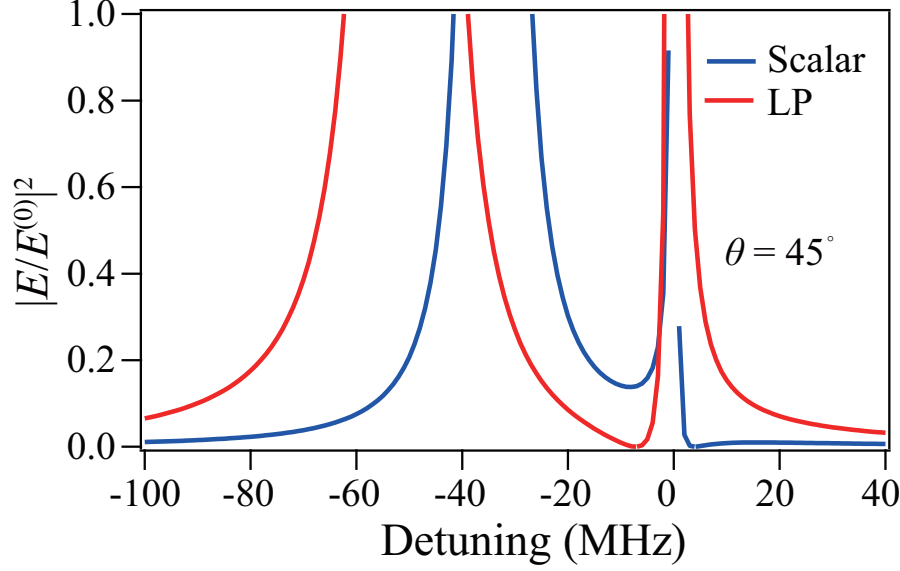


Figure 5.10: The value of $|E/E^{(0)}|^2$ versus the frequency detuning. The red and blue lines correspond to the LP state and scalar state, respectively. The simulation is derived at $\theta = 45^\circ$.

our simulation results shown in Fig. 5.10. According to our calculations, for circularly polarized beams, all off-diagonal terms of the nematicity matrix are zero for the LP and scalar ground states. For a blue-detuned linearly-polarized detection beam, the difference between the two states is not as large as that for a red-detuned linearly-polarized beam. A few different relationship of $E/E^{(0)}$ and the frequency detunings are shown in Fig. 5.10. When the frequency detuning is between -100 MHz and -50 MHz, the value of $E/E^{(0)}$ should vary drastically between the LP and the scalar BECs. When the detuning is more than -50 MHz, e.g., -40 MHz, the ratio of E to $E^{(0)}$ for both the LP and scalar states are very large. On the other hand, when the detuning is less than -100 MHz, e.g., -120 MHz, the ratio of E to $E^{(0)}$ is small for both states. Moreover, if we choose the detuning to be close to zero, the spontaneous emission term cannot be neglected. Therefore, we select the range of the frequency detuning to be between -100 MHz and -50 MHz. We have also taken data by setting the frequency detuning at -120 MHz and -40 MHz. At each frequency detuning, we took around $15 - 20$ data points for each of the initial ground states (LP or scalar BECs).

In our experiments with a carefully chosen detection beam, the spontaneous emission is

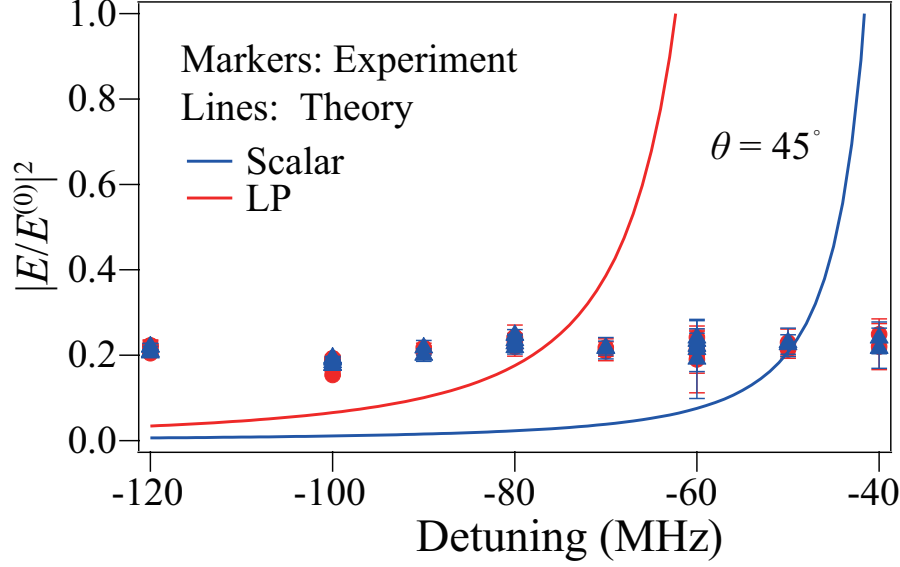


Figure 5.11: The value of $|E/E^{(0)}|^2$ versus the frequency detuning at $\theta = 45^\circ$. The lines are the theoretical predictions and the markers are our experimental data. The red (blue) color corresponds to the LP (scalar) state.

negligible. The detection pulse duration is around 500 ns that is much shorter than the Larmor period. We compare our experimental results with the simulation shown in Fig. 5.11.

We find a large discrepancy between our data and the theoretical predictions. This discrepancy may be due to the fact that we use two independent PDs to separately measure two orthogonal components of the output beam. This technical problem can be solved by replacing the two PDs with a sensitive auto-balanced photodetector. We will try to repeat the above experiments with such an auto-balanced photodetector. If we obtain reasonable results, we will apply this method to a spin singlet state. For spin singlet states, the ratio of E to $E^{(0)}$ should be very close to zero. Then by properly changing the optical setup as elaborated in the previous subsection, other off-diagonal elements of the spin nematicity matrix can be measured in the similar way. The diagonal elements can be obtained by measuring the spin fractional population ρ_{m_F} via the standard Stern-Gerlach absorption imaging or our two-stage microwave imaging method.

In principle, this optical setup can also be applied to detect the Faraday effect. We have tried such Faraday detections at different initial states (i.e., a spinor BEC with $\rho_0 = 0.5$

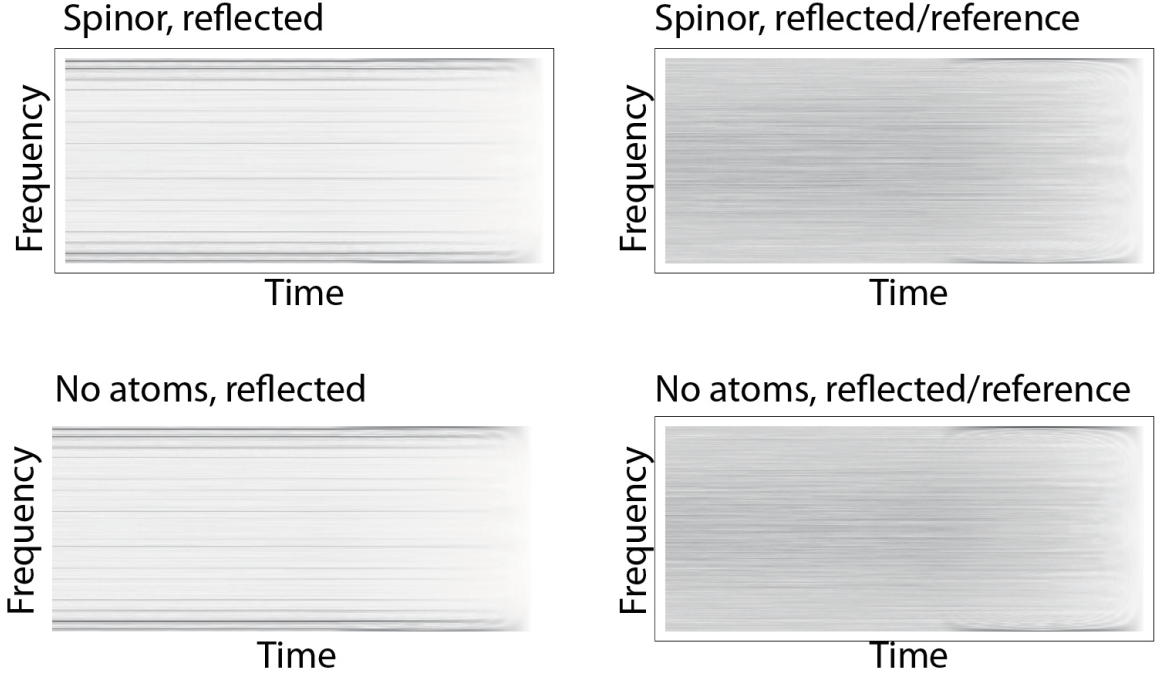


Figure 5.12: The Fourier transformation results for the vacuum state and a spinor BEC ($\rho_0 = 0.5$, $m = 0$).

and $m = 0$, and the vacuum state in which there are no atoms) by increasing the detuning frequency of the input beam to 1 GHz, as shown in Fig. 5.7. Fig. 5.12 shows the Fourier transformation of our experimental data. The Fourier transformation of the reflected beam (i.e., collected by PD1) for the vacuum state shows similar results to that of the spinor BEC state with $\rho_0 = 0.5$ and $m = 0$.

In short, this light-scattering detection method can be easily operated to measure the spin nematicity of the atoms, and is non-destructive.

CHAPTER VI

FUTURE DIRECTIONS

6.1 First-order superfluid to Mott-Insulator phase transition in a homogeneous system

A lot of publications have theoretically studied first-order SF-MI quantum phase transitions in lattice-trapped antiferromagnetic spinor BECs in the last ten years (54, 57, 58, 60, 61). However, due to many technical difficulties, our research group is the first to conduct experimental studies on the first-order phase transitions. As shown in the previous sections and our recent publication, we have presented a few convincing evidence for the first-order transitions (44). Therefore, our immediate research directions are to confirm additional signatures of the first-order SF-MI phase transitions and map out the phase diagram of many-body correlated states (i.e., the ground state phase diagram of lattice-trapped antiferromagnetic spinor BECs). In order to achieve this goal, we have to limit the atom occupation number per lattice site to $n = 2$, since the first-order SF-MI phase transitions only exist in the even Mott lobe. In our current experimental setup, the peak occupation number n_{peak} is five with even and odd atom fillings coexisting, which makes it difficult to observe discontinuous jumps in order parameters associated with the first-order SF-MI phase transitions. We plan to transfer spinor BECs from a tight optical dipole trap (ODT) to a shallower ODT, before loading them to 3D optical lattices. Our calculations predict that this method should be able to reduce n_{peak} from five to two or even one.

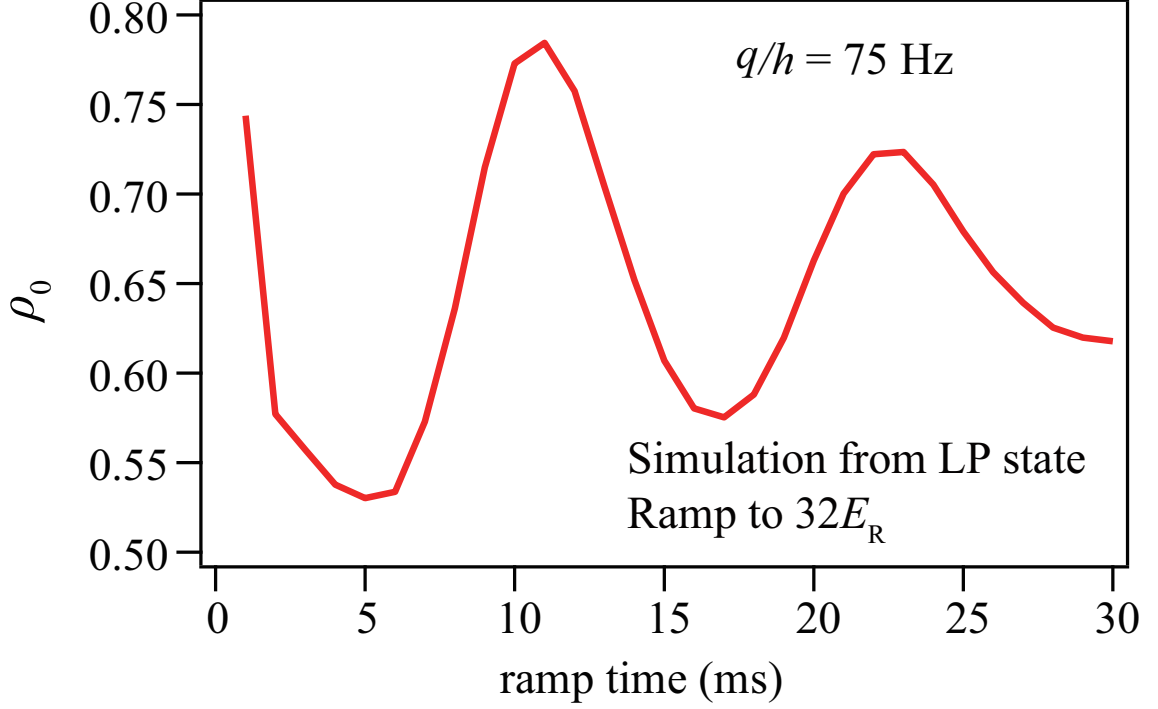


Figure 6.1: Simulation results for an initial LP state crossing the superfluid to the Mott-Insulator phase transitions at $u_L = 32E_R$ in $q/h = 75\text{Hz}$.

6.2 Non-equilibrium dynamics of spinor BECs in optical lattices

Chapter V implies that the lattice ramp time is a key factor, as shown in Fig. 5.4. In fact, the value of ρ_0 strongly depends on the lattice ramp time in various magnetic fields q . We simulate a lattice ramp sequence in which the lattice depth is linearly ramped from zero to $32E_R$ with the initial state being the LP state at different q . A typical simulation result is shown in Fig. 6.1. We find the value of ρ_0 oscillates with the lattice ramp time. There is a characteristic dip time corresponding to the first minimum of ρ_0 at each q .

Figure 6.2 and Figure 6.3 show the dip time and the spin oscillation amplitude as a function of the quadratic Zeeman energy q at $U_2/U_0=0.036$. Since the dip time is very short, the system can't remain adiabatic. The dip time is thus related to the band-gap energy between the ground state and the first excited state. We will confirm it experimentally in the near

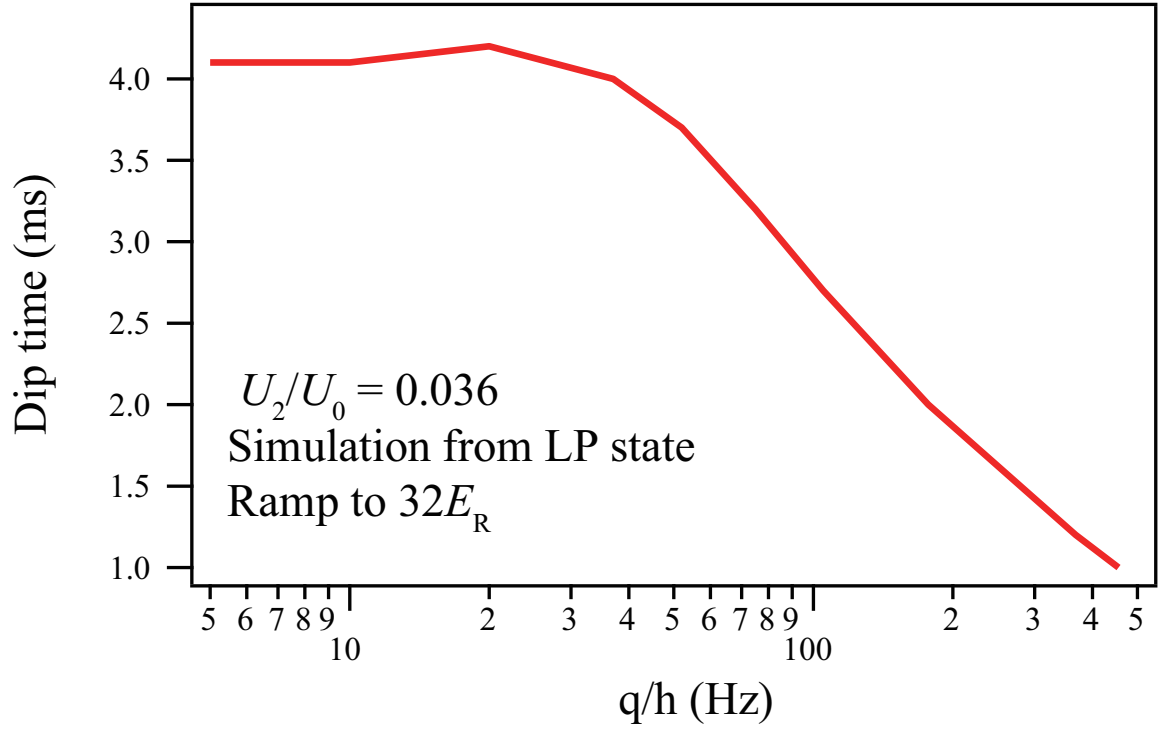


Figure 6.2: The dip time as a function of the quadratic Zeeman energy q .

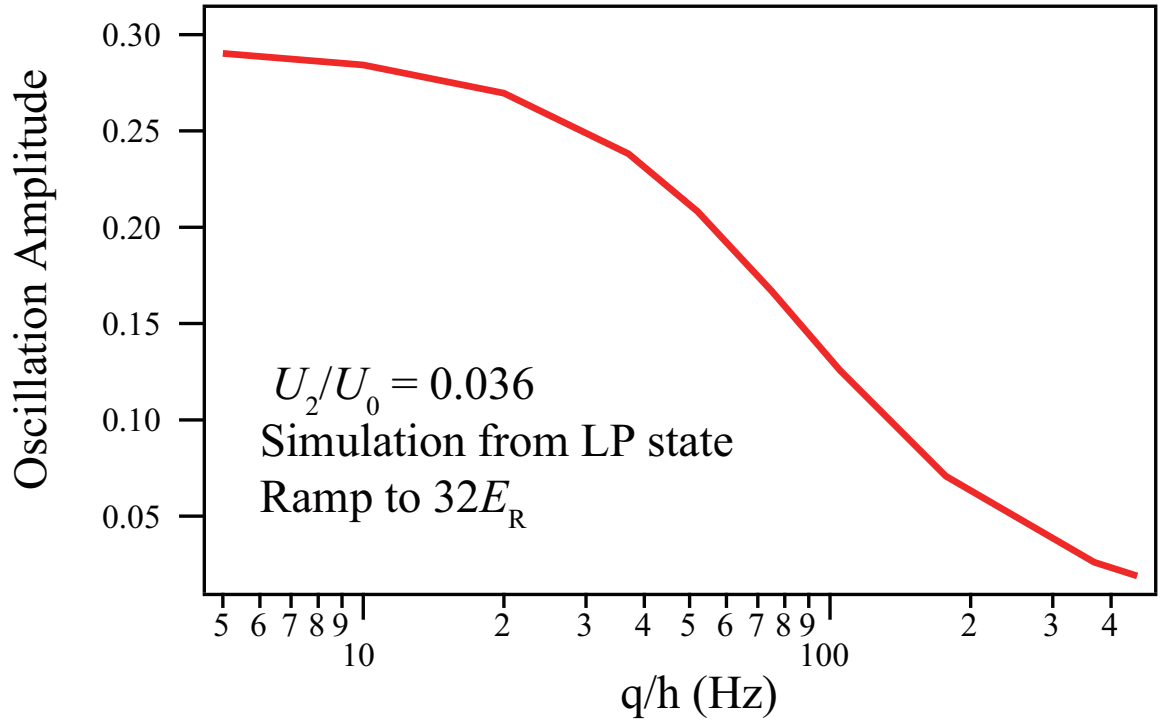


Figure 6.3: Amplitude of spin oscillations as a function of the quadratic Zeeman energy q .

future.

The aforementioned lattice ramp experiment is a good example of the effect of the non-equilibrium dynamics. In fact, non-equilibrium dynamics happens after a quench process (86), i.e, after an initial state is prepared, the Hamiltonian of the system is suddenly changed. This results in a non-equilibrium state, and a dynamical evolution will be induced. Studies of non-equilibrium dynamics are always difficult since we are not sure whether a steady state appears, and if so, what are properties of this state? Moreover, how can we describe evolutions of non-equilibrium dynamic processes? There have been studies performed on these dynamic processes based on the two-point correlation function (87) and the atomic density fluctuation (86, 88). However, these studies utilize the conventional imaging techniques, and thus are limited by the fact that only the spatial information can be detected while the spin information cannot be easily extracted. Our new light-scattering detection method explained in Chapter 5 may provide a more convenient method to study non-equilibrium dynamics by monitoring the spin nematicity.

6.3 Applications in quantum information science

Another research direction is to generate spin squeezing with antiferromagnetic spinor BECs. In the past twenty years, spin squeezing has attracted much attention because of its ability to significantly enhance the precision of spin-related measurements. For example, our calculations predict that spin-squeezed sodium spinor BECs can be applied to develop an ultra-precise magnetic field sensor. We propose to generate spin squeezing via two different methods: through coherent atomic collisions that naturally exist in spinor BECs; or through nonlinear interactions between atoms and a light field, which can be induced by a quantum non-demolition measurement (e.g., Faraday rotation spectroscopy) (89). Our calculations also indicate that optical lattices can be used to create much greater spin squeezing, since lattices can largely enhance interatomic interactions and suppress tunnelling among lattice sites.

REFERENCES

- [1] Einstein, A. “Quantentheorie des einatomigen idealen gases.” Sitzungsberichte der Preussischen Akademie der Wissenschaften **1**, 3 (1925).
- [2] Anderson, M. H., Ensher, J. R., Matthews, M. R., Wieman, C. E., and Cornell, E. A. “Observation of bose-einstein condensation in a dilute atomic vapor.” Science **269**, 198–201 (1995).
- [3] Chu Steven, Hollberg L., Bjorkholm J. E., Cable Alex , and Ashkin A. “Threedimensional viscous confinement and cooling of atoms by resonance radiation pressure.” Phys. Rev. Lett. **55**, 48 (1985).
- [4] Davis, K. B., Mewes, M. O., Andrews, M. R., van Druten, N. J., Durfee, D. S., Kurn, D. M., and Ketterle, W. “Bose-einstein condensation in a gas of sodium atoms.” Phys. Rev. Lett. **75**, 3969–3973 (1995).
- [5] Bradley, C. C., Sackett, C. A., Tollett, J. J., and Hulet, R. G. “Evidence of bose-einstein condensation in an atomic gas with attractive interactions.” Phys. Rev. Lett. **75**, 1687–1690 (1995).
- [6] Fried, Dale G., Killian, Thomas C., Willmann, Lorenz, Landhuis, David, Moss, Stephen C., Kleppner, Daniel, and Greytak, Thomas J. “Bose-einstein condensation of atomic hydrogen.” Phys. Rev. Lett. **81**, 3811–3814 (1998).
- [7] Cornish, S. L., Claussen, N. R., Roberts, J. L., Cornell, E. A., and Wieman, C. E. “Stable ^{85}Rb bose-einstein condensates with widely tunable interactions.” Phys. Rev. Lett. **85**, 1795–1798 (2000).

- [8] Roati, G., Zaccanti, M., D’Errico, C., Catani, J., Modugno, M., Simoni, A., Inguscio, M., and Modugno, G. “ ^{39}K bose-einstein condensate with tunable interactions.” *Phys. Rev. Lett.* **99**, 010403 (2007).
- [9] Weber, Tino, Herbig, Jens, Mark, Michael, Ngerl, Hanns-Christoph, and Grimm, Rudolf. “Bose-einstein condensation of cesium.” *Science* **299**, 232–235 (2003).
- [10] Takasu, Yosuke, Maki, Kenichi, Komori, Kaduki, Takano, Tetsushi, Honda, Kazuhito, Kumakura, Mitsutaka, Yabuzaki, Tsutomu, and Takahashi, Yoshiro. “Spin-singlet bose-einstein condensation of two-electron atoms.” *Phys. Rev. Lett.* **91**, 040404 (2003).
- [11] Griesmaier, Axel, Werner, Jörg, Hensler, Sven, Stuhler, Jürgen, and Pfau, Tilman. “Bose-einstein condensation of chromium.” *Phys. Rev. Lett.* **94**, 160401 (2005).
- [12] Stamper-Kurn, D. M., Andrews, M. R., Chikkatur, A. P., Inouye, S., Miesner, H.-J., Stenger, J., and Ketterle, W. “Optical confinement of a bose-einstein condensate.” *Phys. Rev. Lett.* **80**, 2027–2030 (1998).
- [13] Hall, D. S. *Emergent Nonlinear Phenomena in Bose-Einstein Condensates: Theory and Experiment*. Springer Series on Atomic, Optical, and Plasma Physics, Vol. 45.
- [14] Tsuchiya, S., Kurihara, S., and Kimura, T. “SuperfluidMott insulator transition of spin-1 bosons in an optical lattice.” *Phys. Rev. A* **70**, 043628 (2004).
- [15] Stamper-Kurn, Dan M. and Ueda, Masahito. “Spinor bose gases: Symmetries, magnetism, and quantum dynamics.” *Rev. Mod. Phys.* **85**, 1191–1244 (2013).
- [16] Zhao, L., Jiang, J., Tang, T., Webb, M., and Liu, Y. “Dynamics in spinor condensates tuned by a microwave dressing field.” *Phys. Rev. A* **89**, 023608 (2014).
- [17] Zhang, Wenxian, Zhou, D. L., Chang, M.-S., Chapman, M. S., and You, L. “Coherent spin mixing dynamics in a spin-1 atomic condensate.” *Phys. Rev. A* **72**, 013602 (2005).

- [18] Gerbier, Fabrice, Widera, Artur, Fölling, Simon, Mandel, Olaf, and Bloch, Immanuel. “Resonant control of spin dynamics in ultracold quantum gases by microwave dressing.” *Phys. Rev. A* **73**, 041602 (2006).
- [19] Leslie, S. R., Guzman, J., Vengalattore, M., Sau, Jay D., Cohen, Marvin L., and Stamper-Kurn, D. M. “Amplification of fluctuations in a spinor bose-einstein condensate.” *Phys. Rev. A* **79**, 043631 (2009).
- [20] Bookjans, E. M., Vinit, A., and Raman, C. “Quantum phase transition in an antiferromagnetic spinor bose-einstein condensate.” *Phys. Rev. Lett.* **107**, 195306 (2011).
- [21] Leslie, Sabrina Rose Ann. *On Spinor Condensates as Amplifiers, Sensors and Tunable Quantum Playgrounds for Studies of Spin*. Ph.D. thesis, University of California, Berkeley (2008).
- [22] Santos, L., Fattori, M., Stuhler, J., and Pfau, T. “Spinor condensates with a laser-induced quadratic zeeman effect.” *Phys. Rev. A* **75**, 053606 (2007).
- [23] Greiner, M. *Ultracold quantum gases in three-dimensional optical lattice potentials*. Ph.D. thesis, Ludwig Maximilian University of Munich (2003).
- [24] Zwerger, W. “Mott-Hubbard transition of cold atoms in optical lattices.” *arXiv:cond-mat/0211314* (2003).
- [25] Cheng, C., Rudolf, G., Paul, J., and Eite, T. “Feshbach resonances in ultracold gases.” *Rev. Mod. Phys.* **82**, 1225–1286 (2010).
- [26] Bloch, I., Dalibard, J., Paul, J., and Zwerger, W. “Many-body physics with ultracold gases.” *Rev. Mod. Phys.* **80**, 885–964 (2008).
- [27] Mahmud, K. W. and Tiesinga, E. “Dynamics of spin-1 bosons in an optical lattice: Spin mixing, quantum-phase-revival spectroscopy, and effective three-body interactions.” *Phys. Rev. A* **88**, 023602 (2013).

- [28] Gretchen, K. C., Jongchul, M., Micah, B., Patrick, M., Aaron, E. L., Luis, G. M., David, E. P., and Wolfgang, K. “Imaging the Mott Insulator Shells by Using Atomic Clock Shifts.” *Science* **313**, 649–652 (2006).
- [29] Bloch, Felix. “über die quantenmechanik der elektronen in kristallgittern.” *Zeitschrift für Physik* **52**, 555–600 (1929).
- [30] Zhao, L., Jiang, J., Tang, T., Webb, M., and Liu, Y. “Antiferromagnetic spinor condensates in a two-dimensional optical lattice.” *Phys. Rev. Lett.* **114**, 225302 (2015).
- [31] Denschlag, J. H., Simsarian, J. E., Häffner, H., McKenzie, C., Browaeys, A., Cho, D., Helmerson, K., Rolston, S. L., and Phillips, W. D. “A Bose-Einstein condensate in an optical lattice.” *J. Phys. B: At. Mol. Opt. Phys.* **35**, 3095-3110 (2002).
- [32] Jaksch, D., Bruder, C., Cirac, J. I., Gardiner, C. W., and Zoller, P. “Cold bosonic atoms in optical lattices.” *Phys. Rev. Lett.* **81**, 3108–3111 (1998).
- [33] Fisher, Matthew P. A., Weichman, Peter B., Grinstein, G., and Fisher, Daniel S. “Boson localization and the superfluid-insulator transition.” *Phys. Rev. B* **40**, 546–570 (1989).
- [34] Mobarak, M. *Spinor Bose Gases in Cubic Optical Lattice*. Ph.D. thesis, Free University of Berli (2013).
- [35] Knoop, S., Schuster, T., Scelle, R., Trautmann, A., Appmeier, J., Oberthaler, M. K., Tiesinga, E., and Tiemann, E. “Feshbach spectroscopy and analysis of the interaction potentials of ultracold sodium.” *Phys. Rev. A* **83**, 042704 (2011).
- [36] Crubellier, A., Dulieu, O., Masnou-Seeuws, F., Elbs, M., Knckel, H., and Tiemann, E. “Simple determination of Na₂ scattering lengths using observed bound levels at the ground state asymptote.” *Eur. Phys. J. D* **6**, 211–220 (1999).
- [37] Kawaguchi, Yuki and Ueda, Masahito. “Spinor boseeinstein condensates.” *Physics Reports* **520**, 253 – 381 (2012). Spinor Bose–Einstein condensates.

- [38] Van Abeelen, F. A., and Verhaar, B. J. “Determination of collisional properties of cold Na atoms from analysis of bound-state photoassociation and Feshbach resonance field data.” *Phys. Rev. A* **59**, 578 (1999).
- [39] Ho, Tin-Lun. “Spinor bose condensates in optical traps.” *Phys. Rev. Lett.* **81**, 742–745 (1998).
- [40] Ramesh V. P., Sheshadri, K., and Pandit, R. “Phases and transitions in the spin-1 Bose-Hubbard model: Systematics of a mean-field theory.” *Phys. Rev. B* **77**, 014503 (2008).
- [41] Wagner, A. *Spinor condensates in optical superlattices*. Ph.D. thesis, University of Basel (2012).
- [42] Jiang, J., Zhao, L., Webb, M., and Liu, Y. “Mapping the phase diagram of spinor condensates via adiabatic quantum phase transitions.” *Phys. Rev. A* **90**, 023610 (2014).
- [43] Zhang, Z., and Duan, L. “Generation of Massive Entanglement through an Adiabatic Quantum Phase Transition in a Spinor Condensate.” *Phys. Rev. Lett.* **111**, 180401 (2013).
- [44] Jiang, J., Zhao, L., Wang, S., Chen, Z., Tang, T., Duan, L., and Liu, Y. “First-order superfluid-to-Mott-insulator phase transitions in spinor condensates.” *Phys. Rev. A* **93**, 063607 (2016).
- [45] Zhao, L., Tang, T., Chen, Z. and Liu, Y. “Lattice-induced rapid formation of spin singlets in spin-1 spinor condensates.” *arXiv:1801.00773* (2018)
- [46] Steck, D. A. “Sodium D Line Data.” available at <http://steck.us/alkalidata/sodiumnumbers.1.6.pdf>.
- [47] Zhao, L., Jiang, J., and Liu, Y. “Optimizing a spin-flip zeeman slower.” *arXiv:1401.7181* (2014).

- [48] Markus Greiner, Tilman Esslinger Theodor W. Hänsch, Olaf Mandel and Bloch, Immanuel. “Quantum phase transition from a superfluid to a mott insulator in a gas of ultracold atoms.” *Nature* **415**, 39 (2002).
- [49] Chin, J. K., Miller, D. E., Liu, Y., Stan, C., Setiawan W., Sanner, C., Xu, K., and Ketterle, W. “Evidence for superfluidity of ultracold fermions in an optical lattice.” *Nature* **443**, 961–964 (2006).
- [50] Lignier, H., Sias, C., Ciampini, D., Singh, Y., Zenesini, A., Morsch, O., and Arimondo, E. “Dynamical Control of Matter-Wave Tunneling in Periodic Potentials.” *Phys. Rev. Lett.* **99**, 220403 (2007).
- [51] Windpassinger, P., and Sengstock, K. “Engineering novel optical lattices.” *Rep. Prog. Phys.* **76**, 086401 (2013).
- [52] Heinze, J., Götze, S., Krauser, J. S., Hundt, B., Fläschner, N., Lühmann, D. S., Becker, C., and Sengstock, K. “Multiband Spectroscopy of Ultracold Fermions: Observation of Reduced Tunneling in Attractive Bose-Fermi Mixtures.” *Phys. Rev. Lett.* **107**, 135303 (2011).
- [53] Soltan-Panahi, P., Struck, J., Hauk, P., Bick, A., Plenkers, W., Meineke, G., Becker, C., Windpassinger, P., Lewenstein, M., and Sengstock, K. “Multi-component quantum gases in spin-dependent hexagonal lattices.” *Nat. Phys.* **7**, 434–440 (2011).
- [54] Batrouni, G. G., Rousseau, V. G., S., and Scalettar, R. T. “Magnetic and Superfluid Transitions in the One-Dimensional Spin-1 Boson Hubbard Model.” *Phys. Rev. Lett.* **102**, 140402 (2009).
- [55] Natu, S. S., Pixley, J. H., and Das Sarma, S. “Static and dynamic properties of interacting spin-1 bosons in an optical lattice.” *Phys. Rev. A* **91**, 043620 (2015).
- [56] Shinozaki, M., Tsuchiya, S., Abe, S., Ozaki, T., and Nikuni, T. “Elementary Excitations of Antiferromagnetic Spin-1 Bosons in an Optical Lattice.” *J. Low Temp. Phys.* **175**, 236–242 (2014).

- [57] Demler, E., and Zhou, F. “Spinor Bosonic Atoms in Optical Lattices: Symmetry Breaking and Fractionalization.” *Phys. Rev. Lett.* **88**, 163001 (2002).
- [58] Imambekov, A., Lukin, M., and Demler, E. “Spin-exchange interactions of spin-one bosons in optical lattices: Singlet, nematic, and dimerized phases.” *Phys. Rev. A* **68**, 063602 (2003).
- [59] Krutitsky, K. V., Timmer, M., and Graham, R. “First- and second-order superfluidMott-insulator phase transitions of spin-1 bosons with coupled ground states in optical lattices.” *Phys. Rev. A* **71**, 033623 (2005).
- [60] Kimura, T., Tsuchiya, S., and Kurihara, S. “Possibility of a First-Order SuperfluidMott-Insulator Transition of Spinor Bosons in an Optical Lattice.” *Phys. Rev. Lett.* **94**, 110403 (2005).
- [61] Yamamoto, D., Ozaki, T., Sa de Melo, C. A. R., and Danshita, I. “First-order phase transition and anomalous hysteresis of Bose gases in optical lattices.” *Phys. Rev. A* **88**, 033624 (2013).
- [62] Ohmi, T., and Machida, K. “Bose-Einstein Condensation with Internal Degrees of Freedom in Alkali Atom Gases.” *J. Phys. Soc. Jpn.* **67**, 1822–1825 (1998).
- [63] Xu, K., Liu, Y., Miller, D. E., Chin, J. K., Setiawan, W., and Ketterle, W. “Observation of strong quantum depletion in a gaseous bose-einstein condensate.” *Phys. Rev. Lett.* **96**, 180405 (2006).
- [64] Becker, C, Soltan-Panahi, P, Kronjäger, J, Drscher, S, Bongs, K., and Sengstock, K. “Ultracold quantum gases in triangular optical lattices.” *New Journal of Physics* **12**, 065025 (2010).
- [65] Struck, J., Weinberg, M., Ölschläger, C., Windpassinger, P., Simonet, J., Sengstock, K., Höppner, R., Eckardt, A., Lewenstein, M., and Mathey, L. “Engineering Ising-XY spin-models in a triangular lattice using tunable artificial gauge fields.” *Nat. Phys.* **9**, 738 (2013).

- [66] van Oosten, D., van der Straten, P., and Stoof, H. T. C. “Quantum phases in an optical lattice.” *Phys. Rev. A* **63**, 053601 (2001).
- [67] Xu, K., Liu, Y., Abo-Shaeer, J. R., Mukaiyama, T., Chin, J. K., Miller, D. E., Ketterle, W., Jones, K. M., and Tiesinga, E. “Sodium Bose-Einstein condensates in an optical lattice.” *Phys. Rev. A* **72**, 043604 (2005).
- [68] Huang, C. C., Chang, M. S., and Yip, S. K. “Preparation of two-particle total-hyperfine-spin-singlet states via spin-changing dynamics.” *Phys. Rev. A* **86**, 013403 (2012).
- [69] Tóth, G., and Mitchell, M. W. “Generation of macroscopic singlet states in atomic ensembles.” *New J. Phys.* **12**, 053007 (2010).
- [70] Sun, H., Xu, P., Pu, H., and Zhang, W. “Efficient generation of many-body singlet states of spin-1 bosons in optical superlattices.” *Phys. Rev. A* **95**, 063624 (2017).
- [71] Behbood, N., Martin Ciurana, F., Colangelo, G., Napolitano M., Tóth, G., Sewell, R. J., and Mitchell, M. W. “Generation of Macroscopic Singlet States in a Cold Atomic Ensemble.” *Phys. Rev. Lett.* **113**, 093601 (2014).
- [72] Eckert, K., Zawitkowski, L., Sanpera, A., Lewenstein M., and Polzik, E. S. “Quantum Polarization Spectroscopy of Ultracold Spinor Gases.” *Phys. Rev. Lett.* **98**, 100404 (2007).
- [73] Tóth, G. “Entanglement detection in optical lattices of bosonic atoms with collective measurements.” *Phys. Rev. A* **69**, 052327 (2004).
- [74] Ashhab, S., Leggett, A. J. “Bose-Einstein condensation of spin-1/2 atoms with conserved total spin.” *Phys. Rev. A* **68**, 063612 (2003).
- [75] Ciccarello, F., Paternostro, M., Bose, S., Browne, D. E., Palma, G. M., and Zarcone, M. “Physical model for the generation of ideal resources in multipartite quantum networking.” *Phys. Rev. A* **82**, 030302(R) (2010).

- [76] Urizar-Lanz, I., Hyllus, P., Egusquiza, I. L., Mitchell, M. W., and Tóth, G. “Macroscopic singlet states for gradient magnetometry.” *Phys. Rev. A* **88**, 013626 (2013).
- [77] Ho, T. L., and Yip, S. K. “Fragmented and Single Condensate Ground States of Spin-1 Bose Gas.” *Phys. Rev. Lett.* **84**, 4031 (2000).
- [78] Law, C. K., Pu, H., and Bigelow, N. P. “Quantum Spins Mixing in Spinor Bose-Einstein Condensates.” *Phys. Rev. Lett.* **81**, 5257 (1998).
- [79] Mueller, E. J., Ho, T. L., Ueda, M., and Baym, G. “Fragmentation of Bose-Einstein condensates.” *Phys. Rev. A* **74**, 033612 (2006).
- [80] Sala, A., Núñez, D. L., Martorell, J., De Sarlo, L., Zibold, T., Gerbier, F., Polls, A., and Juliá-Díaz, B. “Shortcut to adiabaticity in spinor condensates.” *Phys. Rev. A* **94**, 043623 (2016).
- [81] De Sarlo, L., Shao, L., Corre, V., Zibold, T., Jacob, D., Dalibard, J., and Gerbier, F. “Spin fragmentation of BoseEinstein condensates with antiferromagnetic interactions.” *New J. Phys.* **15**, 113039 (2013).
- [82] Eto, Y., Ikeda, H., Suzuki, H., Hasegawa, S., Tomiyama, Y., Sekine, S., Sadgrove, M., and Hirano T. “Spin-echo-based magnetometry with spinor Bose-Einstein condensates.” *Phys. Rev. A* **88**, 031602(R) (2013).
- [83] Javanainen, J. “Measurement theory for spinor condensates.” *J. Phys. B* **33**, 5493 (2000).
- [84] Zhou, F. “Quantum Spin Nematic States in BoseEinstein Condensates.” *Int. J. Mod. Phys. B* **17**, 2643 (2003).
- [85] Carusotto, I., and Mueller, E. J. “Imaging of spinor gases.” *J. Phys. B At. Mol. Opt. Phys.* **37**, S115 (2004).
- [86] Langen, T., Geiger, R., and Schmiedmayer J. “Ultracold atoms out of equilibrium.” *Annu. Rev. Condens. Matter Phys.* **6**, 201–217 (2015).

- [87] Langen, T., Erne, S., Geiger, R., Rauer, B., Schweigler, T., Kuhnert, M., Rohringer, W., Mazets, I. E., Gasenzer, T., and Schmiedmayer, J. “Experimental observation of a generalized Gibbs ensemble.” *Science* **348**, 207 (2015).
- [88] Vinit, A., Bookjans, E. M., Sa de Melo, C. A. R. and Raman C. “Antiferromagnetic Spatial Ordering in a Quenched One-Dimensional Spinor Gas.” *Phys. Rev. Lett.* **110**, 165301 (2013).
- [89] Kuzmich, A., Molmer, K., and Polzik, E. S. “Spin Squeezing in an Ensemble of Atoms Illuminated with Squeezed Light.” *Phys. Rev. Lett.* **79**, 4782 (1997).

APPENDICES

APPENDIX A

DYNAMICS IN SPINOR CONDENSATES TUNED BY A MICROWAVE DRESSING FIELD

This appendix includes a reprint of Ref. (16): L. Zhao, J. Jiang, T. Tang, M. Webb, and Y. Liu, Dynamics in spinor condensates tuned by a microwave dressing field, Phys. Rev. A 89, 023608 (2014).

Dynamics in spinor condensates tuned by a microwave dressing field

L. Zhao, J. Jiang, T. Tang, M. Webb, and Y. Liu*

Department of Physics, Oklahoma State University, Stillwater, Oklahoma 74078, USA

(Received 24 October 2013; revised manuscript received 16 December 2013; published 10 February 2014)

We experimentally study spin dynamics in a sodium antiferromagnetic spinor condensate as a result of spin-dependent interactions c and microwave dressing field interactions characterized by the net quadratic Zeeman effect q_{net} . In contrast to magnetic fields, microwave dressing fields enable us to access both negative and positive values of q_{net} . We find an experimental signature to determine the sign of q_{net} and observe harmonic spin population oscillations at every q_{net} except near each separatrix in phase space where spin oscillation period diverges. No spin domains and spatial modes are observed in our system. Our data in the negative q_{net} region exactly resembles what is predicted to occur in a ferromagnetic spinor condensate in the positive q_{net} region. This observation agrees with an important prediction derived from the mean-field theory: spin dynamics in spin-1 condensates substantially depends on the sign of q_{net}/c . This work uses only one atomic species to reveal mean-field spin dynamics, especially the remarkably different relationship between each separatrix and the magnetization, of spin-1 antiferromagnetic and ferromagnetic spinor condensates.

DOI: [10.1103/PhysRevA.89.023608](https://doi.org/10.1103/PhysRevA.89.023608)

PACS number(s): 67.85.Hj, 32.60.+i, 03.75.Kk, 03.75.Mn

I. INTRODUCTION

An atomic Bose-Einstein condensate (BEC) is a state where all atoms have a single collective wave function for their spatial degrees of freedom. The key benefit of spinor BECs is the additional spin degree of freedom. Together with Feshbach resonances and optical lattices which tune the interatomic interactions, spinor BECs constitute a fascinating collective quantum system offering an unprecedented degree of control over such parameters as spin, temperature, and the dimensionality of the system [1,2]. Spinor BECs have become one of the fastest-moving research frontiers in the past 15 years. A number of atomic species have proven to be perfect candidates in the study of spinor BECs, such as $F = 1$ and $F = 2$ hyperfine spin states of ^{87}Rb atoms [1–7] and $F = 1$ hyperfine spin manifolds of ^{23}Na atoms [8–12]. Many interesting phenomena due to the interconversion among multiple spin states and magnetic field interactions have been experimentally demonstrated in spinor BECs, such as spin population dynamics [1–9], quantum number fluctuation [10,13], various quantum phase transitions [1,9,11,12], and quantum spin-nematic squeezing [14]. Spinor BEC systems have been successfully described with a classical two-dimensional phase space [1,2,15–17], a rotor model [18], or a quantum model [13,17].

In this paper, we experimentally study spin-mixing dynamics in a $F = 1$ sodium spinor condensate starting from a nonequilibrium initial state, driven by the net quadratic Zeeman energy $q_{\text{net}} = q_M + q_B$ and antiferromagnetic spin-dependent interactions c . Here q_B and q_M are the quadratic Zeeman shifts induced by magnetic fields and microwave dressing fields, respectively. The spin-dependent interaction energy c is proportional to the mean BEC density and the difference in the $f = 0$ and $f = 2$ s -wave scattering lengths, where f is the summed spin angular momentum in a collision. It is well known that $c > 0$ (or $c < 0$) in $F = 1$ antiferromagnetic ^{23}Na (or ferromagnetic ^{87}Rb) spinor BECs. In contrast to a magnetic field, a microwave dressing

field enables us to access both negative and positive values of q_{net} . A method to characterize microwave dressing fields and an approach to adiabatically sweep q_{net} from $-\infty$ to $+\infty$ are also explained. In both negative and positive q_{net} regions, we observe spin population oscillations resulting from coherent collisional interconversion among two $|F = 1, m_F = 0\rangle$ atoms, one $|F = 1, m_F = +1\rangle$ atom, and one $|F = 1, m_F = -1\rangle$ atom. In every spin oscillation studied in this paper, our data show that the population of the $m_F = 0$ state averaged over time is always larger (or smaller) than its initial value as long as $q_{\text{net}} < 0$ (or $q_{\text{net}} > 0$). This observation provides a clear experimental signature to determine the sign of q_{net} . We also find a remarkably different relationship between the total magnetization m and a separatrix in phase space where spin oscillation period diverges: The position of the separatrix moves slightly with m in the positive q_{net} region, while the separatrix quickly disappears when m is away from zero in the negative q_{net} region. Our data agree with an important prediction derived by Ref. [17]: The spin-mixing dynamics in $F = 1$ spinor condensates substantially depends on the sign of $R = q_{\text{net}}/c$. This work uses only one atomic species to reveal mean-field spin dynamics, especially the relationship between each separatrix and the magnetization, which are predicted to appear differently in $F = 1$ antiferromagnetic and ferromagnetic spinor condensates.

Because no spin domains and spatial modes are observed in our system, the single spatial mode approximation (SMA), in which all spin states have the same spatial wave function, appears to be a proper theoretical model to understand our data. Similarly to Refs. [1,16], we take into account the conservation of the total atom number and the total magnetization m . Spin-mixing dynamics in a $F = 1$ spinor BEC can thus be described with a two-dimensional (ρ_0 versus θ) phase space, where the fractional population ρ_{m_F} and the phase θ_{m_F} of each m_F state are independent of position. The BEC energy E and the time evolution of ρ_0 and θ may be expressed as [1,16]

$$\begin{aligned} E &= q_{\text{net}}(1 - \rho_0) \\ &\quad + c\rho_0[(1 - \rho_0) + \sqrt{(1 - \rho_0)^2 - m^2} \cos \theta], \\ \dot{\rho}_0 &= -(2/\hbar)\partial E/\partial \theta, \dot{\theta} = (2/\hbar)\partial E/\partial \rho_0. \end{aligned} \quad (1)$$

*yingmei.liu@okstate.edu

Here $\theta = \theta_{+1} + \theta_{-1} - 2\theta_0$ is the relative phase among the three m_F spin states and \hbar is the reduced Planck constant. The induced linear Zeeman shift remains the same during the collisional spin interconversion and is thus ignored. The total magnetization is $m = \rho_{+1} - \rho_{-1}$. Spin dynamics in $F = 1$ antiferromagnetic and ferromagnetic spinor BECs have been studied in magnetic fields where $q_{\text{net}} = q_B \propto B^2 > 0$ with ^{23}Na and ^{87}Rb atoms, respectively [1]. A few methods have been explored for generating a negative quadratic Zeeman shift, such as via a microwave dressing field [1, 11, 19–21] or through a linearly polarized off-resonant laser beam [22]. In this paper, we choose the first method.

II. EXPERIMENTAL SETUP

The experimental setup is similar to that illustrated in our previous work [23]. Hot ^{23}Na atoms are slowed by a spin-flip Zeeman slower, captured in a standard magneto-optical trap, cooled through a polarization gradient cooling process to 40 μK , and loaded into a crossed optical dipole trap originating from a linearly polarized high-power infrared laser at 1064 nm. After an optimized 6-s forced evaporative cooling process, a pure $F = 1$ BEC of 1.0×10^5 sodium atoms is created. The spin healing length and the Thomas-Fermi radii of a typical condensate studied in this paper are 13 μm and (6.1, 6.1, 4.3) μm , respectively. We can polarize atoms in the $F = 1$ BEC fully to the $|F = 1, m_F = -1\rangle$ state by applying a weak magnetic field gradient during the first half of the forced evaporation (or fully to the $|F = 1, m_F = 0\rangle$ state by adding a very strong magnetic bias field during the entire 6-s forced evaporation). We then ramp up a small magnetic bias field with its strength B being 271.5(4) mG, while turning off the field gradient. An rf-pulse resonant with the linear Zeeman splitting is applied to prepare an initial state with any desired combination of the three m_F states, which is followed by abruptly switching on an off-resonant microwave pulse to generate a proper microwave dressing field. To create sufficiently large q_{net} , a microwave antenna designed for a frequency near the $|F = 1\rangle \leftrightarrow |F = 2\rangle$ transition is placed a few inches above the center of the magneto-optical trap and connected to a function generator outputting a maximum power of 10 W. The actual power used in this paper is ~ 8 W. After various hold times t in the optical dipole trap, the microwave dressing fields are quickly turned off. Populations of the multiple spin states are then measured via the standard absorption imaging preceded by a 3-ms Stern-Gerlach separation and a 7-ms time of flight.

The exact value of q_{net} is carefully calibrated from a few experimental parameters, such as the polarization and frequency of a microwave pulse. Similarly to Refs. [19, 21], we express the value of q_{net} as

$$\begin{aligned} q_{\text{net}} &= q_B + q_M \\ &= aB^2\hbar + \frac{\delta E|_{m_F=1} + \delta E|_{m_F=-1} - 2\delta E|_{m_F=0}}{2}, \\ \delta E|_{m_F} &= \frac{\hbar}{4} \sum_{k=0, \pm 1} \frac{\Omega_{m_F, m_F+k}^2}{\Delta_{m_F, m_F+k}} \\ &= \frac{\hbar}{4} \sum_{k=0, \pm 1} \frac{\Omega_{m_F, m_F+k}^2}{\Delta - [(m_F + k)/2 - (-m_F/2)]\mu_B B}, \end{aligned} \quad (2)$$

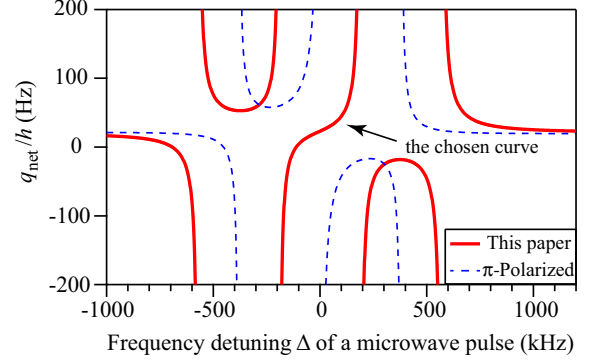


FIG. 1. (Color online) q_{net} as a function of Δ . The residual magnetic field is $B = 271.5(4)$ mG. Dashed blue lines represent the predictions derived from Eq. (2) when the microwave pulse is purely π polarized and its corresponding on-resonance Rabi frequencies are $\Omega_{-1,-2} = \Omega_{0,-1} = \Omega_{1,0} = \Omega_{-1,0} = \Omega_{0,1} = \Omega_{1,2} = 0$, $\Omega_{-1,-1} = \Omega_{1,1} = 4.2$ kHz, and $\Omega_{0,0} = 4.9$ kHz. Solid red lines represent the predictions from Eq. (2) for a typical microwave pulse used in this paper. The specially chosen polarization of this pulse yields nine on-resonance Rabi frequencies as follows: $\Omega_{-1,-2} = 5.1$ kHz, $\Omega_{0,-1} = 3.6$ kHz, and $\Omega_{1,0} = 2.1$ kHz are from the σ^- -polarized component of the pulse; $\Omega_{-1,-1} = \Omega_{0,0} = \Omega_{1,1} = 0$ are from the π -polarized component of the pulse; and $\Omega_{-1,0} = 2.3$ kHz, $\Omega_{0,1} = 3.9$ kHz, and $\Omega_{1,2} = 5.5$ kHz are from the σ^+ -polarized component of the pulse (see text). In this paper, Δ is tuned within the range of -190 kHz to 190 kHz from the $|F = 1, m_F = 0\rangle \leftrightarrow |F = 2, m_F = 0\rangle$ transition.

where $a \approx 277 \text{ Hz/G}^2$ (or $a \approx 71 \text{ Hz/G}^2$) for $F = 1$ ^{23}Na (or ^{87}Rb) atoms, the microwave pulse is detuned by Δ from the $|F = 1, m_F = 0\rangle \leftrightarrow |F = 2, m_F = 0\rangle$ transition, and \hbar is the Planck constant. We define k as 0 or ± 1 for a π - or a σ^\pm -polarized microwave pulse, respectively. For a given polarization k , the allowed transition is $|F = 1, m_F\rangle \leftrightarrow |F = 2, m_F + k\rangle$ and its on-resonance Rabi frequency is $\Omega_{m_F, m_F+k} \propto \sqrt{I_k} C_{m_F, m_F+k}$, where C_{m_F, m_F+k} is the Clebsch-Gordan coefficient of the transition and I_k is the intensity of this purely polarized microwave pulse. We also define $\Delta_{m_F, m_F+k} = \Delta - [(m_F + k)/2 - (-m_F/2)]\mu_B B$ as the frequency detuning of the microwave pulse with respect to the $|F = 1, m_F\rangle \rightarrow |F = 2, m_F + k\rangle$ transition, where μ_B is the Bohr magneton.

A purely π -polarized microwave pulse has been a popular choice in some publications [1, 20, 21]. However, we apply microwave pulses of a specially chosen polarization, in order to continuously scan q_{net} from large negative values to big positive values at a moderate microwave power. Figure 1 compares microwave dressing fields induced by a typical microwave pulse used in this paper and a purely π -polarized microwave pulse. This comparison clearly shows that it is possible to continuously or adiabatically sweep q_{net} from $-\infty$ to $+\infty$ simply by continuously tuning Δ from -190 kHz to 190 kHz with our specially chosen microwave pulses at a power of 8 W. Another advantage of choosing such microwave pulses is to conveniently place the microwave antenna on our apparatus without blocking optical components. To ensure an accurate calibration of q_{net} based on Eq. (2), we measure the nine on-resonance Rabi frequencies Ω daily through monitoring the number of atoms excited by a resonant microwave pulse

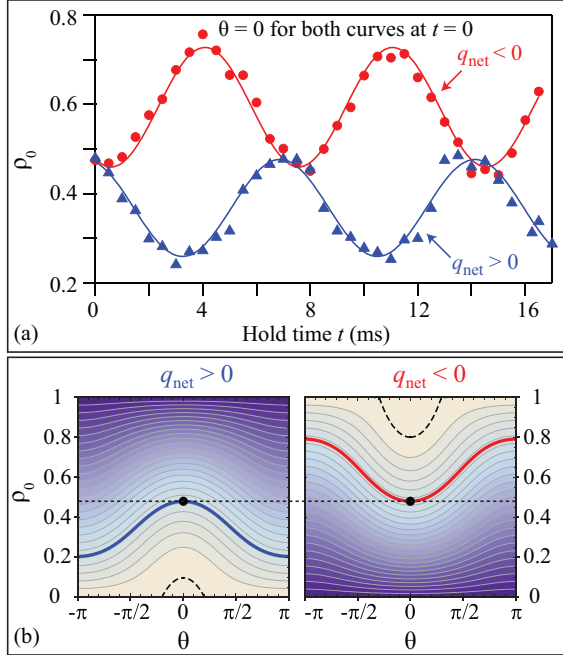


FIG. 2. (Color online) (a) Time evolutions of ρ_0 at $q_{\text{net}}/h = +93\text{Hz} > 0$ (solid blue triangles) and $q_{\text{net}}/h = -83\text{ Hz} < 0$ (solid red circles) with $m = 0$ and $c/h = 52(1)\text{ Hz}$. It is important to note that the two curves start from the same initial state with $\theta|_{t=0} = 0$. Solid lines are sinusoidal fits to the data. (b) Equal-energy contour plots based on Eq. (1) for the two experimental conditions shown in Fig. 2(a), i.e., $q_{\text{net}} > 0$ (left) and $q_{\text{net}} < 0$ (right). The heavy solid blue and red lines represent the energy of the above two experimental conditions, respectively. The dotted black horizontal line is to emphasize the fact that the above two experiments start with the same initial state which is marked by the solid black circles. Dashed black lines represent the energy of the separatrix between the running and oscillatory phase solutions. Darker colors correspond to lower energies.

to the $F = 2$ state as a function of the pulse duration. A typical example of the Rabi frequency measurement is shown in Fig. 3(a). We find that uncertainties of Ω and q_{net} are $\sim 2\%$ and $\sim 5\%$, respectively.

III. DYNAMICS OF SPINOR CONDENSATES IN MICROWAVE DRESSING FIELDS

We observe spin oscillations at every given value of q_{net} within a wide range, i.e., $-240\text{ Hz} \leq q_{\text{net}}/h \leq 240\text{ Hz}$. Typical time evolutions of ρ_0 starting with the same nonequilibrium initial state at a negative and a positive q_{net} are shown in Fig. 2(a). We find that these evolutions can be well fit by sinusoidal functions of the similar oscillation period T and amplitude A . Note that the hold time t is kept between zero and $2T < 100\text{ ms}$, in order to ensure accurate measurements of spin dynamics and avoid significant atom losses due to the presence of off-resonant microwave pulses. On the other hand, our data in Fig. 2(a) show that the value of $\langle \rho_0 \rangle$ drastically differs in the two spin oscillations: $\langle \rho_0 \rangle > \rho_0|_{t=0}$ as long as $q_{\text{net}} < 0$, while $\langle \rho_0 \rangle < \rho_0|_{t=0}$ if $q_{\text{net}} > 0$. Here $\langle \rho_0 \rangle$ is the average value of ρ_0 over time in a spin oscillation and $\rho_0|_{t=0}$ is

the initial value of ρ_0 . This phenomenon is observed at every value of q_{net} when spin oscillations start with the same initial state, although the period T and amplitude A change with q_{net} . The above observations agree well with predictions from the mean-field SMA theory [i.e., Eq. (1)] as shown by the heavy solid lines in Fig. 2(b): ρ_0 is limited between $(\rho_0|_{t=0} - 2A)$ and $\rho_0|_{t=0}$ at $q_{\text{net}} > 0$, while it is restricted between $\rho_0|_{t=0}$ and $(\rho_0|_{t=0} + 2A)$ at $q_{\text{net}} < 0$. We can thus use the phenomenon to conveniently determine the sign of q_{net} , i.e., by comparing the value of $\langle \rho_0 \rangle$ of a spin oscillation to the value of $\rho_0|_{t=0}$.

The value of T as a function of q_{net} is then plotted in Fig. 3 for $m = 0$ and $m = 0.2$, which demonstrates two interesting results. First, when $m = 0$, the spin oscillation is harmonic except near the critical values (i.e., $q_{\text{net}}/h = \pm 52\text{ Hz}$) where the period diverges. This agrees with the predictions derived from Eq. (1), as shown by the dotted red line in Fig. 3. The energy contour E_{sep} where the oscillation becomes anharmonic is defined as a separatrix in phase space. A point on the separatrix satisfies the equation $\dot{\rho}_0 = \dot{\theta} = 0$ according to the mean-field SMA theory. In fact, for our sodium system with $c > 0$, $E_{\text{sep}} = q_{\text{net}}$ for $q_{\text{net}} > 0$, while $E_{\text{sep}} = 0$ at $m = 0$ for $q_{\text{net}} < 0$. Figure 3 shows that the T versus q_{net} curve is symmetric with respect to the $q_{\text{net}} = 0$ axis at $m = 0$. The period T decreases rapidly with increasing $|q_{\text{net}}|$ when $|q_{\text{net}}|$ is large, which corresponds to the “Zeeman regime” with running phase solutions. In the opposite limit, the period only weakly depends on $|q_{\text{net}}|$, which represents the “interaction regime” with oscillatory phase solutions. Here $|q_{\text{net}}|$ is the absolute value of q_{net} . The value of θ is (or is not) restricted in the regions with oscillatory (or running) phase solutions. References [8,9] reported observations of the similar phenomena for $q_{\text{net}} > 0$ with a $F = 1$ antiferromagnetic spinor condensate; however, they did not access the negative q_{net} region.

Figure 3 also demonstrates a remarkably different relationship between the total magnetization m and the separatrix in phase space: the position of the separatrix moves slightly with m in the positive q_{net} region, while the separatrix quickly disappears when m is away from zero in the negative q_{net} region. Good agreements between our data and the mean-field SMA theory are shown in the inset [Fig. 3(b)] and the main figure in Fig. 3. Interestingly, we find that the spin dynamics which appear in our antiferromagnetic sodium system in the negative q_{net} region exactly resembles what is predicted to occur in a ferromagnetic spinor condensate in the positive q_{net} region [16,17]. Note that $R = q_{\text{net}}/c$ is negative in both of these two cases. This observation agrees with an important prediction made by Ref. [17]: The spin-mixing dynamics in $F = 1$ spinor condensates substantially depends on the sign of R . As a matter of fact, our results in the negative q_{net} region are similar to those reported with a $F = 1$ ferromagnetic ^{87}Rb spinor condensate in magnetic fields where $q_{\text{net}} > 0$ [1,3]. It is worth noting that our data in Fig. 3 may also be extrapolated to understand the relationship between the separatrix and m in the ferromagnetic Rb system, although this relationship has not been experimentally explored yet. This paper may thus be the first to use only one atomic species to reveal mean-field spin dynamics, especially the different relationship between each separatrix and the magnetization of $F = 1$ antiferromagnetic and ferromagnetic spinor condensates.

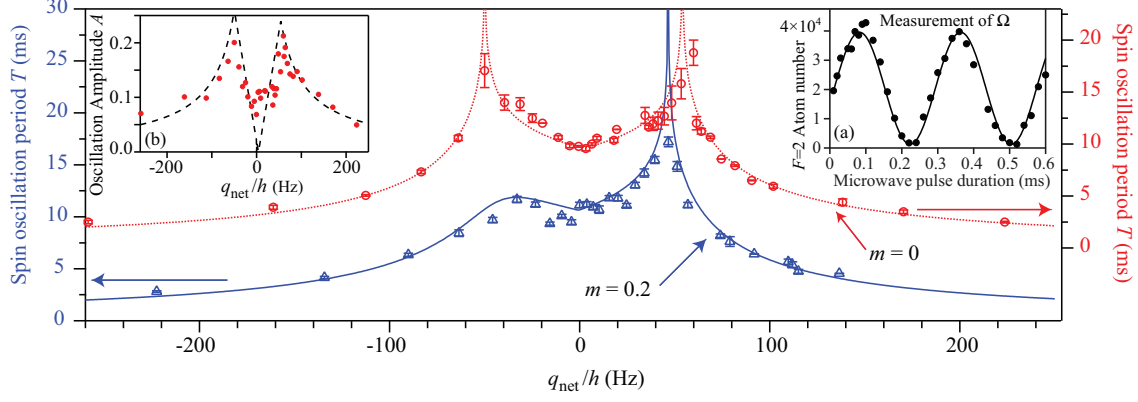


FIG. 3. (Color online) The spin oscillation period as a function of q_{net} for $m = 0$ (open red circles) and $m = 0.2$ (open blue triangles). The lines are fits based on Eq. (1), which yield the following fit parameters: $\rho_0|_{t=0} = 0.48$, $\theta|_{t=0} = 0$, and $c/h = 52(1)$ Hz for $m = 0$ and $\rho_0|_{t=0} = 0.48$, $\theta|_{t=0} = 0$, and $c/h = 47(1)$ Hz for $m = 0.2$. The fit parameters are within the 5% uncertainty of our measurements. Note the different scales of the left and right vertical axes. Inset (a): The number of $F = 2$ atoms excited by a resonant microwave pulse as a function of the pulse duration. The solid line is a sinusoidal fit to extract the on-resonance Rabi frequency Ω of the pulse. Inset (b): Amplitudes A of spin oscillations shown in the main figure as a function of q_{net} at $m = 0$. The dashed black line is a fit based on Eq. (1) with the same set of fit parameters as that applied in the main figure.

IV. CONCLUSION

In conclusion, we have experimentally studied spin dynamics of a sodium spinor condensate in a microwave dressing field. In both negative and positive q_{net} regions, we have observed harmonic spin oscillations and found that the sign of q_{net} can be determined by comparing $\langle \rho_0 \rangle$ to $\rho_0|_{t=0}$. Our data also demonstrate that the position of the separatrix in phase space moves slightly with m in the positive q_{net} region, while the separatrix quickly disappears when m is away from zero in the negative q_{net} region. Our data can be well fit by the mean-field theory and agree with one of its important predictions: The spin-mixing dynamics in $F = 1$ spinor condensates substantially depends on the sign of $R = q_{\text{net}}/c$. This work uses only one atomic species to reveal mean-field spin dynamics and the different dependence of each

separatrix on m in $F = 1$ antiferromagnetic and ferromagnetic spinor condensates. In addition, microwave pulses used in this paper can be applied to cancel out stray magnetic fields and adiabatically sweep q_{net} from $-\infty$ to $+\infty$. This allows studies on interesting but unexplored phenomena at $q_{\text{net}} = 0$, for example, realizing a maximally entangled Dicke state with antiferromagnetic spinor condensates through quantum phase transitions [24].

ACKNOWLEDGMENTS

We thank the Army Research Office, Oklahoma Center for the Advancement of Science and Technology, and Oak Ridge Associated Universities for financial support. M.W. thanks the Niblack Research Scholar program.

- [1] D. M. Stamper-Kurn and M. Ueda, *Rev. Mod. Phys.* **85**, 1191 (2013).
- [2] Y. Kawaguchi and M. Ueda, *Phys. Rep.* **520**, 253 (2012).
- [3] M.-S. Chang, Q. Qin, W. Zhang, L. You, and M. S. Chapman, *Nat. Phys.* **1**, 111 (2005).
- [4] A. Widera, F. Gerbier, S. Fölling, T. Gericke, O. Mandel, and I. Bloch, *New J. Phys.* **8**, 152 (2006).
- [5] J. Kronjäger, C. Becker, P. Navez, K. Bongs, and K. Sengstock, *Phys. Rev. Lett.* **97**, 110404 (2006).
- [6] H. Schmaljohann, M. Erhard, J. Kronjäger, M. Kottke, S. van Staa, L. Cacciapuoti, J. J. Arlt, K. Bongs, and K. Sengstock, *Phys. Rev. Lett.* **92**, 040402 (2004).
- [7] T. Kuwamoto, K. Araki, T. Eno, and T. Hirano, *Phys. Rev. A* **69**, 063604 (2004).
- [8] A. T. Black, E. Gomez, L. D. Turner, S. Jung, and P. D. Lett, *Phys. Rev. Lett.* **99**, 070403 (2007).
- [9] Y. Liu, S. Jung, S. E. Maxwell, L. D. Turner, E. Tiesinga, and P. D. Lett, *Phys. Rev. Lett.* **102**, 125301 (2009).
- [10] Y. Liu, E. Gomez, S. E. Maxwell, L. D. Turner, E. Tiesinga, and P. D. Lett, *Phys. Rev. Lett.* **102**, 225301 (2009).
- [11] E. M. Bookjans, A. Vinit, and C. Raman, *Phys. Rev. Lett.* **107**, 195306 (2011).
- [12] D. Jacob, L. Shao, V. Corre, T. Zibold, L. De Sarlo, E. Mimoun, J. Dalibard, and F. Gerbier, *Phys. Rev. A* **86**, 061601 (2012).
- [13] L. Chang, Q. Zhai, R. Lu, and L. You, *Phys. Rev. Lett.* **99**, 080402 (2007).
- [14] C. D. Hamley, C. S. Gerving, T. M. Hoang, E. M. Bookjans, and M. S. Chapman, *Nature Physics* **8**, 305 (2012).
- [15] W. Zhang, S. Yi, and L. You, *New J. Phys.* **5**, 77 (2003).
- [16] W. Zhang, D. L. Zhou, M.-S. Chang, M. S. Chapman, and L. You, *Phys. Rev. A* **72**, 013602 (2005).
- [17] A. Lamacraft, *Phys. Rev. A* **83**, 033605 (2011).
- [18] R. Barnett, J. D. Sau, and S. Das Sarma, *Phys. Rev. A* **82**, 031602 (2010).

- [19] F. Gerbier, A. Widera, S. Fölling, O. Mandel, and I. Bloch, [Phys. Rev. A **73**, 041602\(R\) \(2006\)](#).
- [20] S. R. Leslie, J. Guzman, M. Vengalattore, J. D. Sau, M. L. Cohen, and D. M. Stamper-Kurn, [Phys. Rev. A **79**, 043631 \(2009\)](#).
- [21] Sabrina R. A. Leslie, Ph.D. thesis, University of California, Berkeley, 2008.
- [22] L. Santos, M. Fattori, J. Stuhler, and T. Pfau, [Phys. Rev. A **75**, 053606 \(2007\)](#).
- [23] J. Jiang, L. Zhao, M. Webb, N. Jiang, H. Yang, and Y. Liu, [Phys. Rev. A **88**, 033620 \(2013\)](#).
- [24] Z. Zhang and L.-M. Duan, [Phys. Rev. Lett. **111**, 180401 \(2013\)](#).

APPENDIX B

FIRST-ORDER SUPERFLUID-TO-MOTT-INSULATOR PHASE TRANSITIONS IN SPINOR CONDENSATES

This appendix includes a reprint of Ref. (44): J. Jiang, L. Zhao, S.-T. Wang, Z. Chen, T. Tang, L.-M. Duan, and Y. Liu, First-order superfluid-to-Mott-insulator phase transitions in spinor condensates, *Phys. Rev. A* 93, 063607 (2016).

First-order superfluid-to-Mott-insulator phase transitions in spinor condensates

J. Jiang,^{1,*} L. Zhao,^{1,*} S.-T. Wang,² Z. Chen,¹ T. Tang,¹ L.-M. Duan,² and Y. Liu^{1,†}

¹*Department of Physics, Oklahoma State University, Stillwater, Oklahoma 74078, USA*

²*Department of Physics, University of Michigan, Ann Arbor, Michigan 48109, USA*

(Received 14 December 2015; revised manuscript received 28 March 2016; published 7 June 2016)

We observe evidence of first-order superfluid-to-Mott-insulator quantum phase transitions in a lattice-confined antiferromagnetic spinor Bose-Einstein condensate. The observed signatures include the hysteresis effect, significant heatings across the phase transitions, and changes in spin populations due to the formation of spin singlets in the Mott-insulator phase. The nature of the phase transitions is found to strongly depend on the ratio of the quadratic Zeeman energy to the spin-dependent interaction. Our observations are qualitatively understood by the mean field theory and suggest tuning the quadratic Zeeman energy is a new approach to realize superfluid-to-Mott-insulator phase transitions.

DOI: [10.1103/PhysRevA.93.063607](https://doi.org/10.1103/PhysRevA.93.063607)

I. INTRODUCTION

A quantum phase transition from a superfluid (SF) to a Mott insulator (MI) was realized in a scalar Bose-Einstein condensate (BEC) trapped by three-dimensional (3D) optical lattices about a decade ago [1]. Marking an important milestone, this achievement has stimulated tremendous efforts to apply highly controllable ultracold bosonic and fermionic systems in studying condensed matter models [2–6]. The SF-MI transitions have been confirmed in various scalar BEC systems via different techniques that can efficiently control the ratio of interatomic interactions to the mobility of atoms [1,5–7]. One well-known approach to simultaneously enhance interatomic interactions and suppress atomic motion is by raising the depth of an optical lattice [1]. Another convenient method is to manipulate interactions with a magnetically tuned Feshbach resonance [7]. A third technique is to control the hopping energy of bosonic atoms by periodically shaking the lattice [6]. Spinor BECs, on the other hand, possess an additional spin degree of freedom, leading to a range of phenomena absent in scalar BECs [8–14]. One important prediction is the existence of first-order SF-MI phase transitions in lattice-trapped antiferromagnetic spinor BECs [2,11,13,15–18]. In contrast, the phase transitions can only be second order in scalar BECs and ferromagnetic spinor BECs [2,5,17].

In this paper, SF-MI transitions are studied in sodium antiferromagnetic spinor BECs confined by cubic optical lattices. We observe the hysteresis effect, changes in spin components, and substantial heating across the phase transitions. These indicate the existence of metastable states, the formation of spin singlets, and associated first-order transitions. In the ground state of the spinor BECs, the nature of SF-MI transitions is found to be determined by the competition between the quadratic Zeeman energy q_B and the spin-dependent interaction U_2 . At low magnetic fields where U_2 dominates, signatures of first-order transitions are observed. In the opposite limit, the transitions appear to be second order and resemble those occurring in scalar BECs. These qualitative features are explained by our mean-field

(MF) calculations. We also study the phase transitions with an initial metastable state and observe stronger heatings across all magnetic fields. Furthermore, our data indicate a new technique to realize SF-MI transitions is by varying q_B .

We describe lattice-trapped $F = 1$ spinor BECs with the Bose-Hubbard (BH) model [15,19]. In the decoupling MF approximation, the Hamiltonian can be reduced to a site-independent form [12,18,20]:

$$H_{\text{MF}} = \frac{U_0}{2}n(n-1) + \frac{U_2}{2}(\vec{S}^2 - 2n) + q_B \sum_{m_F} m_F^2 n_{m_F} - \mu n - zJ \sum_{m_F} (\phi_{m_F}^* b_{m_F} + \phi_{m_F} b_{m_F}^\dagger) + zJ|\vec{\phi}|^2. \quad (1)$$

U_0 is the spin-independent interaction, $n = \sum_{m_F} n_{m_F}$, and $n_{m_F} = b_{m_F}^\dagger b_{m_F}$ is the atom number per site of the m_F state. The vector order parameter is $\phi_{m_F} \equiv \langle b_{m_F} \rangle$, μ is the chemical potential, J is the nearest-neighbor hopping energy, z is the number of nearest neighbors, and \vec{S} is the spin operator [21]. U_2 is positive (negative) in $F = 1$ antiferromagnetic (ferromagnetic) spinor BECs, e.g., $U_2 \simeq 0.04U_0$ in a ^{23}Na system [22]. With spatially uniform superfluids in equilibrium, one can assume ϕ_{m_F} to be real. $\phi_{m_F} = 0$ ($\neq 0$) in the MI (SF) phase.

An antiferromagnetic $F = 1$ spinor BEC of zero magnetization forms a polar superfluid in equilibrium with $\langle \vec{S} \rangle = 0$ [2,22–24]. There are two types of polar superfluids: the longitudinal polar (LP) state with $(\phi_1, \phi_0, \phi_{-1}) = \sqrt{N_{\text{SF}}}(0, 1, 0)$, and the transverse polar (TP) state with $(\phi_1, \phi_0, \phi_{-1}) = \sqrt{N_{\text{SF}}/2}(1, 0, 1)$. Here N_{SF} is the number of condensed atoms per site. At zero q_B and the same N_{SF} , TP and LP states are degenerate in energy. At $q_B > 0$, the MF ground state is always the LP state, but a metastable TP phase may exist [2,24].

Our MF calculations show that q_B/U_2 is a key factor to understand the nature of SF-MI transitions in antiferromagnetic spinor BECs [25]. At low magnetic fields (where $0 \leq q_B \lesssim U_2$), U_2 penalizes high-spin configurations and enlarges the Mott lobes for even number fillings as atoms can form spin singlets to minimize the energy. Metastable Mott-insulator (MMI) and metastable superfluid (MSF) phases emerge due to the spin barrier and lead to first-order SF-MI transitions [see Figs. 1(a) and 1(c)] [15–18]. When 3D lattices are ramped up

*These authors contributed equally to this work.

†yingmei.liu@okstate.edu

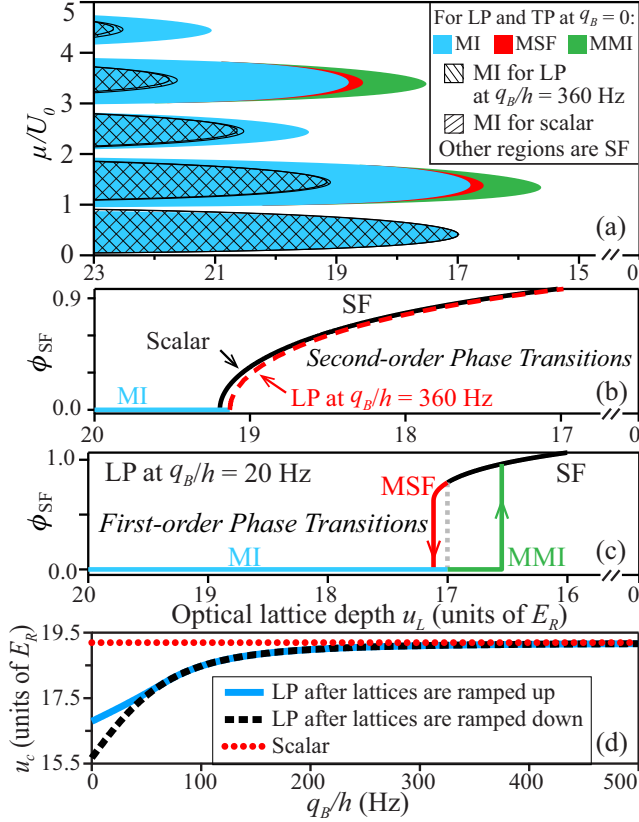


FIG. 1. (a) MF phase diagrams derived from the BH model for scalar BECs [19] and the LP and TP sodium spinor BECs in cubic lattices [see Eq. (1)]. The superfluid order parameter ϕ_{SF} versus u_L at $\mu/U_0 = 1.4$ in (b) scalar and LP spinor BECs at $q_B/h = 360$ Hz and (c) LP spinor BECs at $q_B/h = 20$ Hz. Here $|\phi_{SF}|^2 = N_{SF}$ and \hbar is the Planck constant. (d) Predicted SF-MI transition point u_c versus q_B at $\mu/U_0 = 1.4$ [see Eq. (1)].

and down, hysteresis is expected across the phase transitions (i.e., different transition lattice depth u_c). In addition, when the system changes from a metastable phase to a stable phase (e.g., from MSF to MI), there will be a jump in the order parameter and the system energy, leading to unavoidable heating to the atoms. Hence, hysteresis, substantial heating, and the formation of spin singlets may be interpreted as signatures of first-order transitions. As q_B increases, the $m_F = 0$ state has lower energy than other m_F levels and U_2 becomes less relevant. When q_B becomes sufficiently larger than U_2 ($U_2/\hbar \lesssim 80$ Hz in this work), the ground state phase diagram of antiferromagnetic spinor BECs reverts back to one that is similar to the scalar BH model with only second-order SF-MI transitions (see Fig. 1).

II. EXPERIMENTAL SETUP

Three different types of BECs (i.e., scalar BECs, LP and TP spinor BECs) are studied in this work. A scalar BEC containing up to 1.2×10^5 sodium atoms in the $|F = 1, m_F = -1\rangle$ state is created with an all-optical approach similar to Ref. [26]. A $F = 1$ spinor BEC of zero magnetization is then produced by imposing a resonant rf pulse to the scalar BEC at a fixed

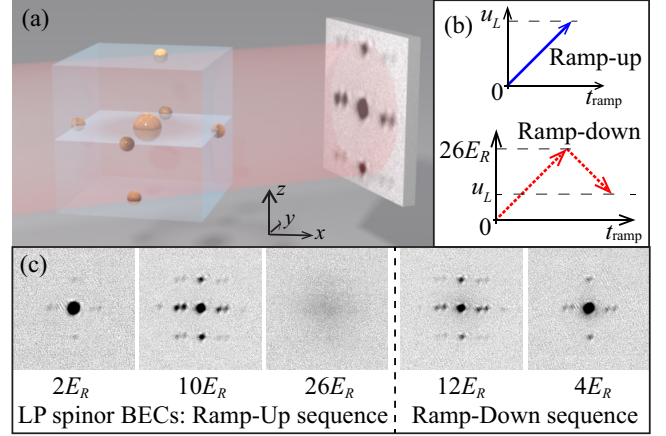


FIG. 2. (a) Schematic of the reciprocal lattice and a TOF image taken after lattices are abruptly released. The area in red represents the imaging beam. (b) Two lattice ramp sequences used in this paper. (c) Interference patterns observed after we abruptly release LP spinor BECs at various final u_L followed by a 5.5-ms TOF at $q_B/h = 360$ Hz. The left (right) panel is taken after ramp-up (ramp-down) sequences. The field of view is $400 \mu\text{m} \times 400 \mu\text{m}$.

q_B . Since the LP state (where $\rho_0 = 1$) is the MF ground state, it can be prepared by simply holding the spinor BEC for a sufficiently long time at high magnetic fields [24]. Here ρ_{m_F} is the fractional population of each m_F state. The TP state (where $\rho_{\pm 1} = 0.5$) is generated via a different approach: we apply a resonant microwave pulse to transfer all $m_F = 0$ atoms in the $F = 1$ spinor BEC to the $F = 2$ state, and then blast away these $F = 2$ atoms with a resonant laser pulse. After quenching q_B to a desired value, we adiabatically load the BEC into a cubic optical lattice within time t_{ramp} . This 3D lattice is constructed by three optical standing waves from a single-mode laser at 1064 nm, which results in a cubic periodic potential with a lattice spacing of 532 nm. All lattice beams are frequency-shifted by at least 20 MHz with respect to each other for eliminating cross interference among them. The calibration of optical lattice depth u_L is conducted via Kapitza-Dirac diffraction patterns and has an uncertainty of $\sim 15\%$. As shown in Fig. 2(b), lattices are linearly ramped up to a given u_L in a ramp-up sequence, while lattices are first adiabatically ramped up to $26E_R$ and then back down to a variable final u_L in a ramp-down sequence. Here $E_R = \hbar^2 k_L^2 / (2M)$ is the recoil energy, M and \hbar are, respectively, the atomic mass and the reduced Planck constant, and k_L is the lattice wave vector. We find that a ramp speed of $2E_R/\text{ms}$ is sufficient to satisfy the intraband adiabaticity condition and ensure $\geq 80\%$ of atoms remain in a scalar or a high-field LP spinor BEC after a ramp-down sequence to $2E_R$. We measure ρ_{m_F} with Stern-Gerlach imaging and microwave imaging after a certain time of flight (TOF).

III. FIRST-ORDER SUPERFLUID TO MOTT-INSULATOR PHASE TRANSITIONS

Distinct interference peaks can always be observed during ballistic expansion, after each BEC is abruptly released from

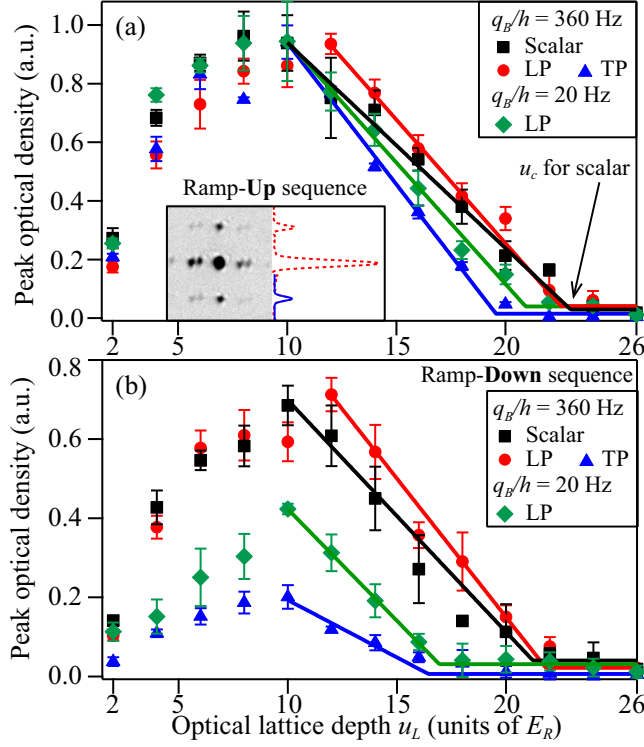


FIG. 3. (a) Peak OD of interference peaks versus u_L after lattice ramp-up sequences. Markers are experimental data, and lines are linear fits. We estimate u_c from the intersection of two linear fits to the data. The inset shows how we extract the peak OD from a TOF image (left). The dotted line in the right inset is a density profile of this TOF image through the central and one pair of interference peaks along the vertical direction, while the solid line is a bimodal fit to one side peak. (b) Similar to panel (a) except that all data are taken after lattice ramp-down sequences.

a shallow lattice of $u_L \leq 10E_R$. As shown in the TOF images in Fig. 2, the six first-order diffracted peaks are symmetrically set apart from the central peak by a distance corresponding to a momentum of $2\hbar k_L$ along three orthogonal axes. These interference peaks may be considered as evidence for coherence associated with the SF phase. In fact, a larger visibility of interference patterns, a narrower width of the central peak, and a higher optical density (OD) of interference peaks have all been used as trustworthy evidence for improved phase coherence in atomic systems [1,3,5,27].

TOF images in Fig. 2(c) show the loss and revival of the interference contrast in spinor BECs as cubic lattices are ramped up and down. A quantitative analysis of these TOF images demonstrates the interference peaks (i.e., coherence associated with the SF phase) change in a reversible manner with u_L (see Fig. 3). First, the interference patterns become more visible as lattices are made deeper and reach their maximum OD around $10E_R$. This may be due to lattice-enhanced density modulation [3,5,27]. Second, when u_L is further increased and exceeds u_c , the interference peaks steadily smear out to a single broad peak indicating atoms completely lose phase coherence. We extract u_c in Fig. 3 from the intersection of two linear fits to the data of a given BEC. To confirm the system has undergone a SF-MI transition, we monitor lattice ramp-down sequences, because

one characteristic of a MI state has proven to be a loss of phase coherence in deep lattices and a subsequent rapid revival of coherence as u_L is reduced [1,3,5]. The interference peaks of scalar and spinor BECs reversibly revive after ramp-down sequences, indicating atoms quickly recohere and return to SF states [see Fig. 3(b)].

Observations in Fig. 3 are qualitatively consistent with our MF calculations and suggest the existence of first-order SF-MI transitions under some circumstances. First, LP spinor BECs at high magnetic fields possess many properties (e.g., the peak OD) that are similar to those of scalar BECs. Their ramp-up and ramp-down curves are close to each other, while both have roughly symmetric transition points u_c . Similar phenomena were observed in ^{87}Rb and ^6Li systems and have been considered as signatures of second-order SF-MI transitions [1,3,5]. Second, LP states at low magnetic fields and TP states at high fields apparently have smaller u_c for both ramp-up and ramp-down processes compared to scalar BECs, suggesting enlarged Mott lobes. In particular, the ramp-down u_c for LP states at low fields is noticeably smaller than their ramp-up u_c , corroborating with the MF picture that hysteresis occurs across first-order phase transitions. Third, the recovered interference contrast is visibly different for various BECs after the ramp-down process (after SF-MI transitions). For scalar and high-field LP spinor BECs, nearly 75% of peak OD can be recovered in the interference peaks after ramp-down sequences. The slightly reduced interference contrast may be due to unaccounted heatings, which leads a small portion of atoms ($< 20\%$) to populate the Brillouin zone. In contrast, after we utilized quite a few techniques and optimized many parameters, the maximal recovered interference contrast of low-field LP states is only $\sim 40\%$ ($\sim 20\%$ for high-field TP states). We attribute this to unavoidable heatings across the first-order transitions as there is a jump in system energy between metastable states and stable states. Both hysteresis effect and significant heatings strongly suggest that first-order SF-MI transitions are realized in our experiment. Note, however, we do not see noticeable jumps in the observables as is typically associated with first-order transitions. This is likely due to the presence of even and odd atom fillings in inhomogeneous systems such as trapped BECs, although predicted first-order SF-MI transitions only exist for even occupancy number. Limited experimental resolutions may be another reason.

Our data in Fig. 3(b) also demonstrate that a new approach to realize SF-MI transitions is by ramping q_B at a fixed u_L . For example, when the final u_L in ramp-down sequences is set at a value between $17E_R$ and $21E_R$, atoms in LP spinor BECs can cross SF-MI transitions if q_B/h is sufficiently reduced (e.g., from 360 to 20 Hz). This agrees with Fig. 1(d): u_c depends on q_B .

We then compare scalar and spinor BECs within a wide range of magnetic fields, $20\text{ Hz} \leq q_B/h \leq 500\text{ Hz}$, after identical lattice ramp sequences to $u_L = 10E_R$. We choose $10E_R$ because it is apparently the lattice depth around which we observe the maximum interference contrast, with negligible difference in scalar and spinor BECs after ramp-up sequences at all q_B . This is consistent with Fig. 1, which predicts all BECs studied in this work should be well in the SF phase at $10E_R$. However, the interference peak ODs show intriguing

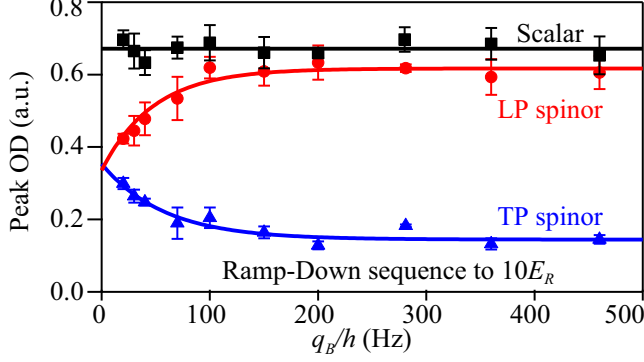


FIG. 4. Peak OD of interference peaks versus q_B observed after lattice ramp-down sequences to $10E_R$. Markers are experimental data. Red and blue lines are exponential fits. The black line is a linear fit.

differences after ramp-down sequences to $10E_R$ (see Fig. 4): deviations from the maximal value appear for LP spinor BECs at low magnetic fields and the TP state at all positive q_B . We again attribute this to different amount of heatings across SF-MI transitions. Different extent of heatings may be produced due to different spin barriers as well as the amount of energy jump across the transitions. Hence, the maximum recovered OD is a good indicator for the appearance or disappearance of first-order SF-MI transitions. Notably, LP spinor BECs are found to behave very similarly to scalar BECs when $q_B \gg U_2$ (see Fig. 4). This observation is consistent with Fig. 1(d), in which the two MF curves for the LP state merge indicating that metastable states disappear and SF-MI transitions become second order when $q_B/h > 70$ Hz. Furthermore, the difference between LP and TP spinor BECs appears to exponentially decrease as q_B approaches zero. Exponential fits to the data verify that LP and TP spinor BECs should show the same behavior at $q_B = 0$.

Figure 5(a) shows the change in the fractional population ρ_0 as the lattice is ramped up, which provides another evidence that is consistent with first-order SF-MI transitions. In the MF picture, the first-order transition is related to the formation of spin singlets in the even lobe MI phase. For example, in the $n = 2$ MI lobe, the MI ground state $|\psi_g\rangle$ at zero q_B is the singlet state where $\rho_0 = \rho_{+1} = \rho_{-1} = 1/3$ [11,13,15–18], i.e., $|\psi_g(q_B = 0)\rangle = |S = 0, S_z = 0\rangle = \frac{\sqrt{2}}{3}|101\rangle - \frac{\sqrt{1}}{3}|020\rangle$ in the occupation basis of $|n_1, n_0, n_{-1}\rangle$. For $q_B > 0$, we diagonalize Eq. (1) in this occupation basis and find $|\psi_g\rangle = \frac{U_2 - 2q_B + \sqrt{4q_B^2 - 4q_B U_2 + 9U_2^2}}{2\sqrt{2}U_2} |101\rangle - |020\rangle$. This calculation result is shown in Fig. 5(b). A line at $u_L = 26E_R$ from Fig. 5(b) represents the result in the $n = 2$ Mott lobe, which is also highlighted as the theoretical $n = 2$ line in Fig. 5(a) inset. Two predictions can be derived from this MF calculation: ρ_0 drastically decreases as atoms cross the first-order transition (from SF to MI), and ρ_0 rises with q_B in the $n = 2$ Mott lobe.

Our observations shown in Fig. 5(a) may be the first experimental confirmation of these predictions: an initial LP state is found to sigmoidally evolve to a state consisting of all three m_F components as u_L is ramped up at low magnetic fields, with the measured ρ_0 sigmoidally decreasing from one in the SF phase to around 0.6 in the MI phase

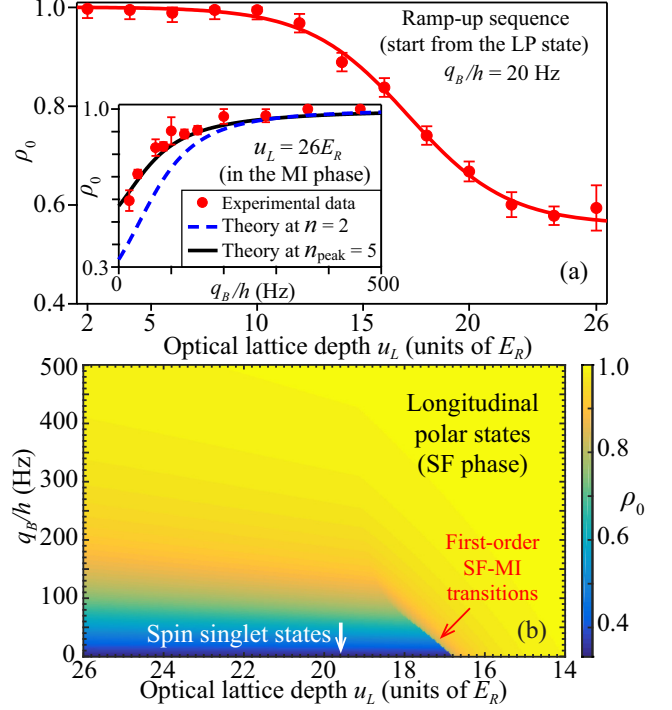


FIG. 5. (a) Measured ρ_0 versus u_L after an initial LP spinor BEC undergoes ramp-up sequences to various final u_L at $q_B/h = 20$ Hz. The solid line is a sigmoidal fit. Inset: Similar to the main figure except that we set q_B at various values and the final u_L at $26 E_R$ to ensure atoms enter into the MI phase. The dashed (solid) line represents the MF result for $n = 2$ ($n_{\text{peak}} = 5$). (b) Predicted ρ_0 in the ground state of antiferromagnetic spinor BECs at various u_L and q_B with $\mu/U_0 = 1.4$.

($u_L \geq 22E_R$). In addition, in the MI phase, the measured ρ_0 rises with q_B , and approaches one at $q_B \gg U_2$ where the ground state phase diagram of antiferromagnetic spinor BECs resembles the scalar BH model with only second-order SF-MI transitions [see Fig. 5(a) inset]. This observation can be well understood by the MF calculation [the $n_{\text{peak}} = 5$ line in Fig. 5(a) inset]. Note that the peak filling factor n_{peak} is five in our inhomogeneous system, and the data in Fig. 5(a) thus represent an average of different atom fillings. In other words, the theoretical $n_{\text{peak}} = 5$ line in Fig. 5(a) inset represents a weighted average of the MF predictions at five different n (i.e., $n = 1, 2, 3, 4, 5$) based on the atom density distribution in a harmonic trap. Good agreements between our data and the MF theory suggest that the observed substantial change in ρ_0 at very low fields may be mainly due to the formation of spin singlets in the even lobe MI phase (after atoms cross the first-order transitions).

IV. CONCLUSION

In conclusion, we have conducted the first experimental study on SF-MI transitions in lattice-confined sodium spinor BECs. We have observed hysteresis, significant heatings across the phase transitions, and the change in ρ_0 resulting from the formation of spin singlets in the MI phase. These observations strongly suggest first-order SF-MI transitions are realized

in our system. Our data are understood by the MF theory and suggest SF-MI transitions can be realized by tuning q_B . Further studies are required to confirm more signatures of the first-order transitions, e.g., by precisely imaging Mott shells [4,7].

ACKNOWLEDGMENTS

We thank the Army Research Office and the National Science Foundation for financial support. S.T.W. and L.M.D. are supported by the IARPA, the ARL, and the AFOSR MURI program. S.T.W. thanks Xiaopeng Li for helpful discussions.

-
- [1] M. Greiner, O. Mandel, T. Esslinger, T. W. Hänsch, and I. Bloch, *Nature (London)* **415**, 39 (2002).
 - [2] D. M. Stamper-Kurn and M. Ueda, *Rev. Mod. Phys.* **85**, 1191 (2013).
 - [3] J. K. Chin, D. E. Miller, Y. Liu, C. Stan, W. Setiawan, C. Sanner, K. Xu, and W. Ketterle, *Nature (London)* **443**, 961 (2006).
 - [4] G. K. Campbell, J. Mun, M. Boyd, P. Medley, A. E. Leanhardt, L. G. Marcassa, D. E. Pritchard, and W. Ketterle, *Science* **313**, 649 (2006).
 - [5] I. Bloch, J. Dalibard, and W. Zwerger, *Rev. Mod. Phys.* **80**, 885 (2008).
 - [6] H. Lignier, C. Sias, D. Ciampini, Y. Singh, A. Zenesini, O. Morsch, and E. Arimondo, *Phys. Rev. Lett.* **99**, 220403 (2007).
 - [7] C. Chin, R. Grimm, P. Julienne, and E. Tiesinga, *Rev. Mod. Phys.* **82**, 1225 (2010).
 - [8] P. Windpassinger and K. Sengstock, *Rep. Prog. Phys.* **76**, 086401 (2013).
 - [9] J. Heinze, S. Götz, J. S. Krauser, B. Hundt, N. Fläschner, D.-S. Lühmann, C. Becker, and K. Sengstock, *Phys. Rev. Lett.* **107**, 135303 (2011).
 - [10] P. Soltan-Panahi, J. Struck, P. Hauke, A. Bick, W. Plenkers, G. Meineke, C. Becker, P. Windpassinger, M. Lewenstein, and K. Sengstock, *Nat. Phys.* **7**, 434 (2011).
 - [11] S. S. Natu, J. H. Pixley, and S. Das Sarma, *Phys. Rev. A* **91**, 043620 (2015).
 - [12] K. W. Mahmud and E. Tiesinga, *Phys. Rev. A* **88**, 023602 (2013).
 - [13] G. G. Batrouni, V. G. Rousseau, and R. T. Scalettar, *Phys. Rev. Lett.* **102**, 140402 (2009).
 - [14] M. Shinozaki, S. Tsuchiya, S. Abe, T. Ozaki, and T. Nikuni, *J. Low Temp. Phys.* **175**, 236 (2014).
 - [15] E. Demler and F. Zhou, *Phys. Rev. Lett.* **88**, 163001 (2002); A. Imambekov, M. Lukin, and E. Demler, *Phys. Rev. A* **68**, 063602 (2003).
 - [16] K. V. Krutitsky, M. Timmer, and R. Graham, *Phys. Rev. A* **71**, 033623 (2005).
 - [17] T. Kimura, S. Tsuchiya, and S. Kurihara, *Phys. Rev. Lett.* **94**, 110403 (2005).
 - [18] D. Yamamoto, T. Ozaki, C. A. R. Sa de Melo, and I. Danshita, *Phys. Rev. A* **88**, 033624 (2013).
 - [19] M. P. A. Fisher, P. B. Weichman, G. Grinstein, and D. S. Fisher, *Phys. Rev. B* **40**, 546 (1989).
 - [20] R. V. Pai, K. Sheshadri, and R. Pandit, *Phys. Rev. B* **77**, 014503 (2008); A. Wagner, Spinor condensates in optical superlattices, Ph.D. thesis, University of Basel, 2012.
 - [21] The linear Zeeman energy is ignored in Eq. (1), since it remains unchanged during collisional spin interconversions in $F=1$ spinor BECs. The spin operators are given by $S_x = \frac{1}{\sqrt{2}}(b_0^\dagger b_1 + b_1^\dagger b_0 + b_{-1}^\dagger b_0 + b_0^\dagger b_{-1})$, $S_y = \frac{i}{\sqrt{2}}(b_0^\dagger b_1 - b_1^\dagger b_0 + b_{-1}^\dagger b_0 - b_0^\dagger b_{-1})$, $S_z = b_1^\dagger b_1 - b_{-1}^\dagger b_{-1}$.
 - [22] L. Zhao, J. Jiang, T. Tang, M. Webb, and Y. Liu, *Phys. Rev. Lett.* **114**, 225302 (2015).
 - [23] T.-L. Ho, *Phys. Rev. Lett.* **81**, 742 (1998); T. Ohmi and K. Machida, *J. Phys. Soc. Jpn.* **67**, 1822 (1998).
 - [24] J. Jiang, L. Zhao, M. Webb, and Y. Liu, *Phys. Rev. A* **90**, 023610 (2014).
 - [25] We solve Eq. (1) self-consistently by requiring $\phi_{m_F} = \langle b_{m_F} \rangle$ in the occupancy number n basis with a maximum of 15 atoms per site. Since the observed n_{peak} is five, the truncation errors are negligible.
 - [26] L. Zhao, J. Jiang, T. Tang, M. Webb, and Y. Liu, *Phys. Rev. A* **89**, 023608 (2014).
 - [27] K. Xu, Y. Liu, D. E. Miller, J. K. Chin, W. Setiawan, and W. Ketterle, *Phys. Rev. Lett.* **96**, 180405 (2006).

APPENDIX C

LATTICE-INDUCED RAPID FORMATION OF SPIN SINGLETs IN SPIN-1 SPINOR CONDENSATES

This appendix includes a reprint of Ref. (45): L. Zhao, T. Tang, Z. Chen, and Y. Liu, Lattice-induced rapid formation of spin singlets in spin-1 spinor condensates, arXiv: 1801.00773.

Lattice-induced rapid formation of spin singlets in spin-1 spinor condensates

L. Zhao, T. Tang, Z. Chen, and Y. Liu*

Department of Physics, Oklahoma State University, Stillwater, Oklahoma 74078, USA

(Dated: January 3, 2018)

We experimentally demonstrate that combining a cubic optical lattice with a spinor Bose-Einstein condensate substantially relaxes three strict constraints and brings spin singlets of ultracold spin-1 atoms into experimentally accessible regions. About 80 percent of atoms in the lattice-confined spin-1 spinor condensate are found to form spin singlets, immediately after the atoms cross first-order superfluid to Mott-insulator phase transitions in a microwave dressing field. A phenomenological model is also introduced to well describe our observations without adjustable parameters.

PACS numbers: 67.85.Fg, 03.75.Kk, 03.75.Mn, 05.30.Rt

Many-body spin singlet states, in which multiple spin components of zero total spin are naturally entangled, have been widely suggested as ideal candidates in investigating quantum metrology and quantum memories [1–14]. Advantages of spin singlets in the quantum information research include long lifetimes and enhanced tolerance to environmental noises [2, 3]. These advantages may become more pronounced if the singlets consist of ultracold spin-1 particles [1]. A spin singlet is the ground state of many types of spinor gases, however, its experimental realizations have proven to be very challenging mainly due to its fragilities [3, 10, 12–15]. Allowed parameter ranges for spin singlets of spin-1 atoms are strictly limited to the vicinity of zero quadratic Zeeman energy q and zero magnetization m , and the ranges drastically shrink when the atom number increases [10–13]. Another constraint is the formation of spin singlets requires atoms remaining adiabatic for a long time duration [13, 16]. In this Letter, we experimentally demonstrate that combining a spinor Bose-Einstein condensate (BEC) with cubic optical lattices significantly relaxes these strict constraints and enables creating spin singlets of spin-1 atoms rapidly. Our observations confirm that spin singlets are brought into experimentally accessible regions by two key lattice-modified parameters, which are the lattice-enhanced interatomic interactions and substantially reduced atom number in individual lattice sites. Lattice-confined spinor BECs present degeneracies in spin and spatial domains, which provide perfect platforms to simulate quantum mesoscopic systems and study rich physics of fragmentation [7, 12].

Different methods have been proposed for detecting spin singlets. The first approach is to measure the population of each spin component, as atoms in a spin singlet should be evenly distributed into all spin states [17, 18]. The second method is to verify a spin singlet is invariant after its spin is rotated by a resonant Rf-pulse [2, 9, 12, 18, 19]. Another signature of a spin singlet is its high level of spin squeezing shown in quantum non-demolition measurements [2, 4–6]. A spin singlet can also be identified by its high-order correlation functions, e.g., its zero spin nematicity detected by light scattering

measurements [12, 20]. Other detectable parameters of a spin singlet include large population fluctuations in each of its spin components, and its excitation spectra mapped by Bragg scattering [10, 17]. In this paper, we apply the first two methods to demonstrate that about 80% of spin-1 atoms in a lattice-confined spinor BEC can form spin singlets, immediately after the atoms cross first-order superfluid (SF) to Mott-insulator (MI) phase transitions in a microwave dressing field. A phenomenological model is also developed to explain our observations without adjustable parameters.

We start each experimental cycle with an antiferromagnetic $F=1$ spinor BEC of $n = 1.2 \times 10^5$ sodium atoms and zero m in its free-space ground state, i.e., a longitudinal polar (LP) state in the $q > 0$ region or a transverse polar (TP) state when $q < 0$ [21–25]. The atoms are then loaded into cubic lattices and enter into the MI phase with the peak occupation number per lattice site being five, $n_{\text{peak}} = 5$. We express the Hamiltonian of the spinor Mott insulators by ignoring the hopping energy in the site-independent Bose-Hubbard model as [21]:

$$\hat{H} = \frac{U_0}{2}(\hat{n}^2 - \hat{n}) - \mu\hat{n} + \frac{U_2}{2}(\hat{\mathbf{S}}^2 - 2\hat{n}) + q(\hat{n}_1 + \hat{n}_{-1}). \quad (1)$$

Here U_0 (U_2) is the spin-independent (spin-dependent) interaction, μ is the chemical potential, $\hat{\mathbf{S}}$ is the spin operator, and $\hat{n} = \sum_{m_F} \hat{n}_{m_F}$ is the number operator of all hyperfine m_F states. We obtain the ground states of spinor Mott insulators by diagonalizing Eq. (1) at a given n . For example, the ground states are spin singlets at zero q in the even Mott lobes.

Sufficiently deep cubic lattices localize atoms and lower n by five orders of magnitude in a typical BEC system. Figure 1 illustrates how this enormous reduction in n together with the lattice-enhanced interatomic interactions can make spin singlets realizable in experimentally accessible regions. Figure 1 is derived from the mean-field theory (MFT) and based on two notable signatures of a spin singlet, i.e., each of its m_F states has an identical fractional population ρ_{m_F} and a big $\Delta\rho_{m_F}$ (the standard deviation of ρ_{m_F}) [10, 17, 18]. For example,

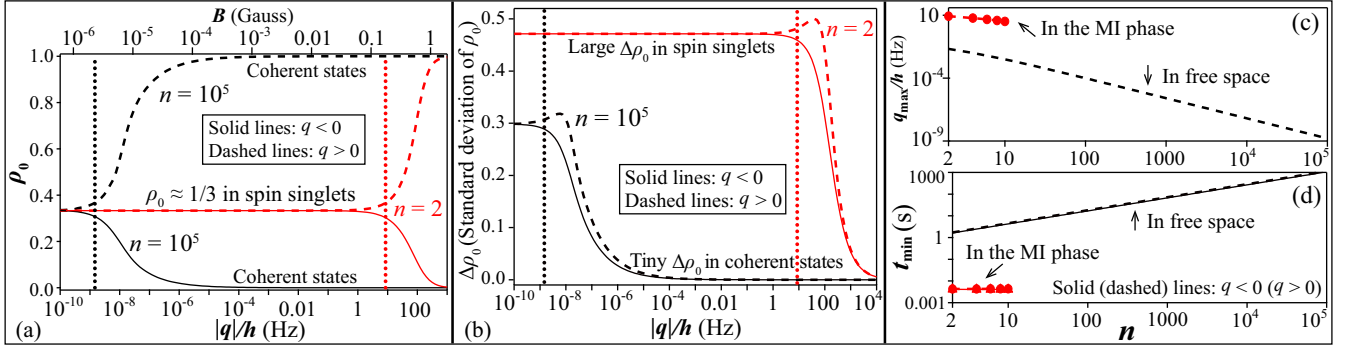


FIG. 1. (a) and (b): vertical black (red) dotted lines mark q_{\max} , the maximum allowed q for spin singlets, in $F=1$ sodium spinor BECs of $n = 10^5$ atoms in free space (in the $n=2$ Mott lobe at $u_L = 26E_R$). All panels are derived from MFT at zero m with solid (dashed) lines representing the $q < 0$ ($q > 0$) region, and black (red) lines representing spinor gases in free space (spinor Mott insulators) [16]. (a) Predicted ρ_0 versus $|q|$ at $n = 2$ (red) and 10^5 (black). The top horizontal axis lists the corresponding B when $q > 0$. (b) Predicted $\Delta\rho_0$ versus $|q|$ at $n = 2$ (red) and 10^5 (black). (c) Predicted q_{\max} versus n . (d) The minimum time t_{\min} versus n for generating singlets of sodium atoms via an adiabatic sweep at its corresponding $\pm q_{\max}$.

spin singlets of $F=1$ atoms should have $\rho_0 \approx \rho_{\pm 1} \approx 1/3$ and $\Delta\rho_0 = 2\Delta\rho_{\pm 1} > 0.29$. In sharp contrast, $\rho_0 = 0$ and $\rho_{\pm 1} = 0.5$ ($\rho_0 = 1$ and $\rho_{\pm 1} = 0$) with negligible $\Delta\rho_{m_F}$ are found in coherent TP (LP) states when $q < 0$ ($q > 0$) [24]. The allowed q range for spin singlets is $0 \leq |q| \leq q_{\max}$, which is determined by considering $\Delta\rho_{m_F} \gg 0$ and $\rho_0 = (1+0.1)/3$ at $q = q_{\max}$ (that corresponds to $\rho_0 \simeq (1-0.1)/3$ at $q = -q_{\max}$) in MFT [26]. An expansion of ten orders of magnitude in q_{\max} is marked by vertical dotted lines in Figs. 1(a) and 1(b), i.e., from a narrow region of $|q|/h < 2 \times 10^{-9}$ Hz in a free-space spinor BEC of 10^5 atoms to a much broader range of $|q|/h < 9$ Hz in $n=2$ spinor Mott insulators. Here h is the Planck constant. This drastic raise in q_{\max} as n decreases is also shown in Fig. 1(c) for a wide range of achievable n . In addition, the lattice-induced big reduction in n can relax the magnetization constraint on creating spin singlets by five orders of magnitude, because $|m| \lesssim 0.15/n$ is required for singlets at zero q [27]. Figure 1(d) indicates another big improvement made by cubic lattices: t_{\min} can be dramatically decreased by three orders of magnitude after a free-space spinor BEC enters the MI phase [16]. Here t_{\min} is the minimum time for generating singlets via adiabatically sweeping one parameter, such as q and the lattice depth u_L . Spin singlets of $F=1$ atoms can thus be created in realistic experimental setups, e.g., in the spinor Mott insulators of $|m| \leq 0.05$ as confirmed by our experimental data in Figs. 3 and 4.

In each experimental cycle, we prepare a LP or TP state at $q/h = 40$ Hz by pumping all atoms in the undesired m_F states of a $F=1$ spinor BEC to the $F=2$ state with resonant microwave pulses, and blasting away these $F=2$ atoms via a resonant laser pulse. We then quench q to a proper value in microwave dressing fields [28], and load atoms into a cubic lattice constructed by three standing waves along orthogonal directions. The lattice spacing is 532 nm, while lattice beams are originated from

a single-mode laser at 1064 nm and frequency-shifted by 20 MHz with respect to each other. We use Kapitza-Dirac diffraction patterns to calibrate u_L . Each data point in this paper is collected after atoms being abruptly released from a lattice at a fixed u_L and expanding ballistically within a given time of flight t_{TOF} . The standard Stern-Gerlach absorption imaging is a good method to measure ρ_{m_F} of spinor gases in the SF phase. Stern-Gerlach separations become indiscernible, when atoms completely lose phase coherence in the MI phase and the signal-to-noise ratio diminishes in TOF images. To measure ρ_0 in spinor Mott insulators, we develop a two-step microwave imaging method as follows: 1) count the $m_F=0$ atoms with the first imaging pulse preceded by transferring all atoms in the $|F=1, m_F=0\rangle$ state to the $F=2$ state; 2) count all remaining atoms that are in the $m_F = \pm 1$ states with the second imaging pulse. We compare these two imaging methods using a free-space spinor BEC, and find they give similar ρ_0 with a negligible difference (unless specified, all quoted uncertainties are 2 standard errors).

To ensure atoms adiabatically enter the MI phase, a cubic lattice is linearly ramped up within time t_{ramp} to $u_L = 26E_R$. Here E_R is the recoil energy [23]. We carefully select t_{ramp} based on three criteria. First, t_{ramp} should be long enough to satisfy $du_L/dt \ll 32\pi E_R^2/h$, the interband adiabaticity requirement [29]. Second, t_{ramp} should be larger than the MFT predicted t_{\min} , as explained in Fig. 1(d). These two criteria set $t_{\text{ramp}} > 5$ ms for our system. On the other hand, t_{ramp} should be sufficiently short, with $t_{\text{ramp}} \leq t_0$ to ensure lattice-induced heating is negligible and atom losses are not greater than 10%. Figure 2 explains how we determine t_0 from the observed relationship between t_{ramp} and ρ_0 in spinor Mott insulators at $u_L = 26E_R$ and $q/h = 460$ Hz. In such a high field, SF-MI phase transitions are second order because $U_2 = 0.04U_0 > 0$ and $q \gg U_2$ at this u_L for the

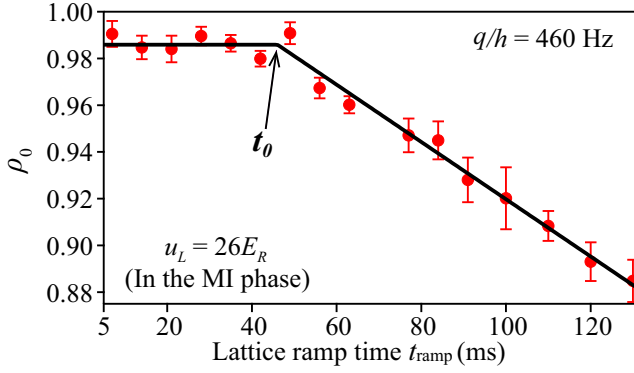


FIG. 2. Measured ρ_0 versus t_{ramp} after an initial LP spinor BEC enters the MI phase in a high field. Black lines are two linear fits. We estimate t_0 , the ideal t_{ramp} , from the intersection point of these two lines (see text).

sodium atoms [21]. Atoms initially in a LP state should thus stay in the LP state with $\rho_0 \simeq 1$, as they adiabatically cross the phase transitions and enter into the MI phase [21]. The value of ρ_0 quickly drops when inevitable heating is induced by lattices in a non-adiabatic lattice ramp sequence. We extract t_0 from the intersection point of two linear fits to the data in Fig. 2, which yields $t_{\text{ramp}} \leq t_0 \approx 45$ ms. Within this acceptable t_{ramp} range, a slower lattice ramp is preferred because it could more easily keep the system adiabatic and provide sufficient time for the atom redistribution processes [30]. The ideal lattice ramp speed is therefore set at $du_L/dt = 26E_R/t_0$ for our system.

The opposite limit is $|q| \ll U_2$ near zero q , where SF-MI phase transitions are first order and spin singlets are the ground state of $F=1$ spinor gases in the even Mott lobes [21]. We may thus identify the formation of spin singlets from evolutions of ρ_0 and $\Delta\rho_0$ during a first-order SF-MI transition. Figure 3 shows two such evolutions when atoms initially in the TP state are adiabatically loaded into the cubic lattice at the ideal lattice ramp speed to various final u_L in $q/h = -4$ Hz. These evolutions have three distinct regions. In the SF phase where $0 \leq u_L \leq 15E_R$, atoms remain in the TP state with $\rho_0 = 0$ and negligible $\Delta\rho_0$. As atoms cross first-order SF-MI transitions in $15E_R \leq u_L \leq 18E_R$, ρ_0 and $\Delta\rho_0$ sigmoidally increase with u_L . When all atoms enter into the MI phase at $u_L \geq 21E_R$, both ρ_0 and $\Delta\rho_0$ reach their equilibrium values of $\rho_0 \approx 0.3$ and $\Delta\rho_0 \gg 0$. These observations qualitatively agree with the characteristics of spin singlets. Despite that other factors can also increase $\Delta\rho_0$ in the MI phase, the measured $\Delta\rho_0$ is much smaller than the MFT prediction shown in Fig. 1(b). This may be due to the fact that the observed $\Delta\rho_0$ is an average over all 5×10^4 lattice sites in our system. Unless one can detect single lattice site precisely, the value of $\Delta\rho_0$ may not be used to verify spin singlets in lattice-confined spinor gases. We also monitor the time evolu-

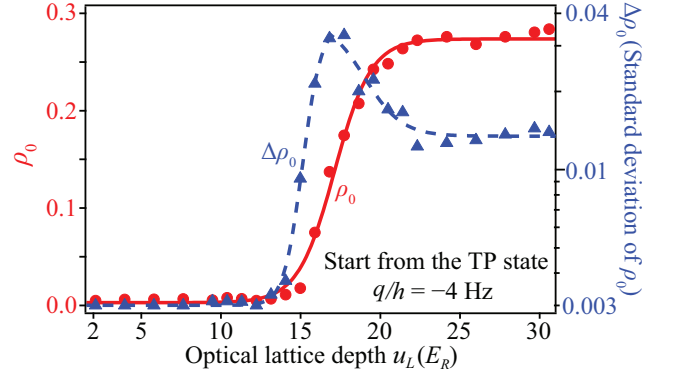


FIG. 3. Measured ρ_0 (red circles) and $\Delta\rho_0$ (blue triangles) versus u_L after an initial TP spinor BEC undergoes the ideal lattice sequence to various final u_L in a weak field near zero q . The solid line is a sigmoidal fit, and the dashed line is to guide the eye.

tion of atoms at fixed u_L and q after the ideal lattice ramp sequence. No spin oscillations are found at each q studied in this paper, which confirms atoms always stay at their ground states in these ideal lattice sequences.

We observe similar ρ_0 and $\Delta\rho_0$ evolutions within a wide range of q near zero field. The measured ρ_0 versus q in spinor Mott insulators at $u_L = 26E_R$ is shown in Fig. 4(a). These Mott insulators of $n_{\text{peak}} = 5$ are inhomogeneous systems, in which ρ_0 at a fixed q may be given by the weighted average over all Mott lobes:

$$\rho_0 = \sum_{j=1}^5 \rho_{0j} \chi_j. \quad (2)$$

Here ρ_{0j} is the MFT predicted ρ_0 in the ground state ψ_j of the $n=j$ Mott lobe, and χ_j represents mean-field atom density distributions in a harmonic trap [21]. The prediction of Eq. (2) shown by red dashed lines in Fig. 4(a), however, appears to largely disagree with our data. To understand this big discrepancy, we have tried several models and found only one phenomenological model can surprisingly describe our data without adjustable parameters (see black solid lines in Fig. 4(a)). This phenomenological model is based on one major difference between spinor and scalar Mott insulators predicted by the Bose-Hubbard model: i.e., the formation of spin singlets enlarges even Mott lobes in antiferromagnetic spinor gases [21]. For example, the $n=2$ even Mott lobe emerges at $u_L \approx 16.5E_R$, while the $n=3$ odd Mott lobe only exists in a much deeper lattice of $u_L \geq 19.5E_R$ for $F=1$ sodium spinor gases near zero field [21]. In the intermediate lattice depth of $16.5E_R < u_L < 19.5E_R$ near zero q , atoms in the $n=3$ lattice sites can freely tunnel among adjacent lattice sites, while particles in an $n=2$ lattice site already enter into the MI phase and are localized in this site. At a proper u_L near zero q , atoms may thus be able to redistribute among lattice sites with a given

odd n in the lattice-confined spinor gases. For example, at $u_L = 19E_R > 16.5E_R$, the tunneling of one atom converts two adjacent $n=3$ lattice sites to one $n=2$ and one $n=4$ sites. This u_L is then deep enough to localize the six atoms by forming a two-body spin singlet in one site and a 4-body spin singlet in the other site [30]. As a result of similar redistribution processes, atoms initially in lattice sites with $n = 5$ may form 4-body and 6-body spin singlets in the ideal lattice ramp sequences. In contrast, redistribution processes may not occur among the $n=1$ lattice sites, because the $n=1$ and $n=2$ Mott lobes emerge at similar u_L for the sodium atoms. Our phenomenological model takes these atom redistribution processes into account, and expresses ρ_0 in the spinor Mott insulators created by the ideal lattice ramp sequence as

$$\rho_0 = \sum_{j=3,5} \chi_j \frac{(j+1)\rho_{0j+1} + (j-1)\rho_{0j-1}}{2j} + \sum_{j=1,2,4} \rho_{0j} \chi_j. \quad (3)$$

Figure 4(a) shows that the prediction of Eq. (3) agrees with our experimental data. The validity of this phenomenological model is also verified by comparing its prediction with the observed ρ_0 , after a resonant Rf-pulse is applied to rotate the spin of atoms by 90 degrees. In this paper, the spin rotation operator $\hat{R}_x = \exp(-i\frac{\pi}{2}\hat{S}_x)$ is along the x -axis, which is orthogonal to the quantization axis (z -axis). After $\pi/2$ spin rotations, ρ_{0j} in Eq. (3) changes to $\rho_{0j}^r = \frac{\langle \psi_j | \hat{R}_x^\dagger \hat{n}_0 \hat{R}_x | \psi_j \rangle}{\langle \psi_j | \hat{R}_x^\dagger \hat{n}_x \hat{R}_x | \psi_j \rangle}$ in the $n=j$ Mott lobe. The prediction of Eq. (3) after these spin rotations is shown by the upper black solid line in Fig. 4(a), which well agrees with our data. The two data sets in Fig. 4(a) respectively represent projections of the atomic spin along two orthogonal axes. The observed good agreements between our phenomenological model and these data sets, therefore, suggest this model may reveal mechanisms of the ideal lattice ramp sequence in antiferromagnetic spinor gases.

Our data taken with and without the $\pi/2$ spin rotations appear to converge to a value around $\rho_0 \approx 1/3$ as q gets closer to zero in Fig. 4(a). This indicates the spinor Mott insulators become more rotationally invariant near zero field. As the spin rotational invariance is one unique signature of spin singlets, the reduced gap between the two data sets in Fig. 4(a) implies significant amounts of atoms may form spin singlets when q approaches zero. In our system, about 10% of atoms stay in the $n=1$ Mott lobe where no spin singlet can be formed. This accounts for the observed small gap between the two data sets near zero q in Fig. 4(a), and limits the maximum f_{ss} realizable in our system to about 90%. Here f_{ss} represents the fraction of atoms forming spin singlets in spinor gases. We extract f_{ss} from the measured ρ_0 based on Ref. [31]. The two data sets in Fig. 4(a) appear to yield similar

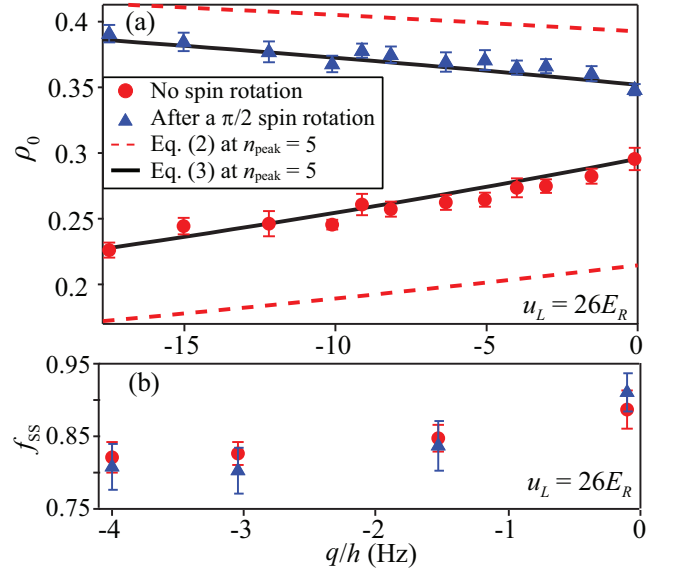


FIG. 4. (a) Red circles (blue triangles) are the measured ρ_0 in spinor Mott insulators without (with) atoms being rotated by resonant $\pi/2$ pulses at various q . The black solid (red dashed) line is the prediction of Eq. (3) (Eq. (2)). (b) Spin singlet fraction f_{ss} extracted from Panel (a) versus q (see text). The insulators are created after an initial TP spinor BEC undergoes the ideal lattice ramp sequence.

f_{ss} at a fixed q near zero field: i.e., $f_{ss} \approx 80\%$ when $-4 \text{ Hz} \leq q/h \leq 0 \text{ Hz}$ as shown in Fig. 4(b). This indicates around 80% of atoms form spin singlets in our system. Similar phenomena and slightly smaller f_{ss} are also observed in spinor Mott insulators generated after atoms initially in the LP state cross first-order SF-MI transitions in the ideal lattice ramp sequences when $q > 0$.

In conclusion, our experimental data have confirmed that combining cubic lattices with spinor BECs makes spin singlets of ultracold spin-1 atoms achievable in experimentally accessible regions. Via two independent detection methods, we have demonstrated that about 80% of atoms in the lattice-confined $F=1$ spinor BEC form spin singlets, after the atoms cross first-order SF-MI phase transitions near zero field. We have developed a phenomenological model that explains our observations without adjustable parameters. Our recent work has also indicated that we may be able to identify another signature of spin singlets, i.e., confirm their zero spin nematicity in light scattering measurements [32].

We thank the National Science Foundation and the Oklahoma Center for the Advancement of Science and Technology for financial support.

* Electronic address: yingmei.liu@okstate.edu

[1] C. C. Huang, M. S. Chang, and S. K. Yip, Phys. Rev. A **86**, 013403 (2012).

- [2] G. Tóth, and M. W. Mitchell, New J. Phys. **12**, 053007 (2010).
- [3] H. Sun, P. Xu, H. Pu, and W. Zhang, Phys. Rev. A **95**, 063624 (2017)
- [4] N. Behbood, F. Martin Ciurana, G. Colangelo, M. Napolitano, G. Tóth, R. J. Sewell, and M. W. Mitchell, Phys. Rev. Lett. **113**, 093601 (2014).
- [5] K. Eckert, L. Zawitkowski, A. Sanpera, M. Lewenstein, and E. S. Polzik, Phys. Rev. Lett. **98**, 100404 (2007).
- [6] G. Tóth, Phys. Rev. A **69**, 052327 (2004).
- [7] S. Ashhab and A. J. Leggett, Phys. Rev. A **68**, 063612 (2003).
- [8] F. Ciccarello, M. Paternostro, S. Bose, D. E. Browne, G. M. Palma, and M. Zarcone, Phys. Rev. A **82**, 030302(R) (2010).
- [9] I. Urizar-Lanz, P. Hyllus, I. L. Egusquiza, M. W. Mitchell, and G. Tóth, Phys. Rev. A **88**, 013626 (2013).
- [10] T. L. Ho and S. K. Yip, Phys. Rev. Lett. **84**, 4031 (2000).
- [11] C. K. Law, H. Pu, and N. P. Bigelow, Phys. Rev. Lett. **81**, 5257 (1998).
- [12] E. J. Mueller, T. L. Ho, M. Ueda, and G. Baym, Phys. Rev. A **74**, 033612 (2006).
- [13] A. Sala, D. L. Núñez, J. Martorell, L. De Sarlo, T. Zibold, F. Gerbier, A. Polls, and B. Juliá-Díaz, Phys. Rev. A **94**, 043623(2016).
- [14] L. De Sarlo, L. Shao, V. Corre, T. Zibold, D. Jacob, J. Dalibard, and F. Gerbier, New J. Phys. **15**, 113039 (2013).
- [15] Y. Eto, H. Ikeda, H. Suzuki, S. Hasegawa, Y. Tomiyama, S. Sekine, M. Sadgrove, and T. Hirano, Phys. Rev. A **88**, 031602(R)(2013)
- [16] Our MFT calculations are based on Ref. [24] with $t_{\min} = \hbar/\Delta E$. Here ΔE is the energy gap between the ground state and the first excited state.
- [17] A. Imambekov, M. Lukin, and E. Demler, Phys. Rev. A **68**, 063602 (2003).
- [18] J. Javanainen, J. Phys. B **33**, 5493 (2000).
- [19] F. Zhou, Int. J. Mod. Phys. B **17**, 2643 (2003).
- [20] I. Carusotto and E. J. Mueller, J. Phys. B **37**, S115 (2004).
- [21] J. Jiang, L. Zhao, S.-T. Wang, Z. Chen, T. Tang, L.-M. Duan, and Y. Liu, Phys. Rev. A **93**, 063607 (2016), and the references therein.
- [22] D. M. Stamper-Kurn and M. Ueda, Rev. Mod. Phys. **85**, 1191 (2013).
- [23] L. Zhao, J. Jiang, T. Tang, M. Webb, and Y. Liu, Phys. Rev. Lett. **114**, 225302 (2015).
- [24] J. Jiang, L. Zhao, M. Webb, and Y. Liu, Phys. Rev. A **90**, 023610 (2014).
- [25] T.-L. Ho, Phys. Rev. Lett. **81**, 742 (1998); T. Ohmi and K. Machida, J. Phys. Soc. Jpn. **67**, 1822 (1998).
- [26] Our criterion for determining q_{\max} is stricter than those used in Refs. [13, 14].
- [27] We derive this magnetization constraint from Eq. 3 of Ref. [10].
- [28] L. Zhao, J. Jiang, T. Tang, M. Webb, and Y. Liu, Phys. Rev. A **89**, 023608 (2014).
- [29] J. K. Chin, D. E. Miller, Y. Liu, C. Stan, W. Setiawan, C. Sanner, K. Xu, and W. Ketterle, Nature **443**, 961 (2006).
- [30] The required time for the atom redistribution process is proportional to $(6nJ)^{-1}$ in cubic lattices. This may set $t_{\text{ramp}} \geq 35$ ms for our system.
- [31] Our phenomenological model predicts that $\rho_0 = f_{\text{ss}}/3 (= f_{\text{ss}}/3 + (1 - f_{\text{ss}})/2)$ in spinor Mott insulators created from an initial TP spinor BEC in the ideal lattice sequence without (with) $\pi/2$ spin rotations. This prediction only works near zero q and slightly underestimates f_{ss} .
- [32] T. Tang, L. Zhao, Z. Chen, and Y. Liu (unpublished).

VITA

Tao Tang

Candidate for the Degree of

Doctor of Philosophy

Dissertation: PHASE DIAGRAMS AND QUANTUM PHASE TRANSITIONS IN
LATTICE-CONFINED ANTIFERROMAGNETIC SPINOR BOSE-EINSTEIN CON-
DENSATES

Major Field: Photonics

Biographical:

Education:

Completed the requirements for the Doctor of Philosophy in Photonics at
Oklahoma State University, Stillwater, Oklahoma in December, 2018.

Completed the requirements for the Master of Science in Physics at Univer-
sity of Science and Technology of China, Hefei, China in 2012.

Completed the requirements for the Bachelor of Science in Physics at HeFei
University of Technology, Hefei, China in 2009.

Professional Memberships:

American Physical Society